

THESIS FOR THE DEGREE OF DOCTOR OF PHILOSOPHY

Refining Electric Powertrain Efficiency:
SiC vs. Si Semiconductor, Thermal Solutions,
and Optimal Power Conversion Strategies

SEPIDEH M. AMIRPOUR



CHALMERS
UNIVERSITY OF TECHNOLOGY

Department of Electrical Engineering
Division of Electric Power Engineering
Chalmers University of Technology
Gothenburg, Sweden, 2025

**Refining Electric Powertrain Efficiency:
SiC vs. Si Semiconductor, Thermal Solutions, and Optimal Power
Conversion Strategies**

SEPIDEH M. AMIRPOUR
ISBN 978-91-8103-230-7

Copyright © 2025 SEPIDEH M. AMIRPOUR
All rights reserved.

Doktorsavhandlingar vid Chalmers tekniska högskola
Ny serie nr. 5688
ISSN 0346-718X
Department of Electrical Engineering

Chalmers University of Technology
SE-412 96 Gothenburg, Sweden
Phone: +46 (0)31 772 1000
www.chalmers.se

Printed by Chalmers Reproservice
Gothenburg, Sweden, 2025

To my loving family and my ever-living father

Abstract

This work first establishes a concrete numerical system simulation model to quantify the impact of junction temperature feedback on power and energy losses in three-phase silicon carbide (SiC)-based propulsion inverters compared to traditional silicon-insulated-gate bipolar transistors (Si-IGBTs). It then proposes and demonstrates improved heat spreading within a SiC power module using graphene-assembled films in both the packaging and a pin-fin-based heatsink through comprehensive thermal simulations.

Using a loss minimization approach, this work further determines the optimal DC-link voltage across the full drive range. It includes a detailed power loss analysis of a propulsion inverter, incorporating temperature variations, alongside finite element method (FEM)-based loss modeling of an interior permanent magnet (IPM) synchronous machine under variable DC-link voltages.

Finally, this study focuses on identifying the optimal switching frequency for SiC-based motor drives vs. IGBT counterparts across a wide range of operating conditions. The approach involves conducting a comprehensive real-time FEM analysis of losses induced by pulse width modulation (PWM) voltages in an IPM synchronous machine, compared to conventional sinusoidal current excitation feeding.

Utilizing a graphene layer in the SiC module reduced the MOSFET junction temperature by 10°C , corresponding to an applied power loss per SiC chip in steady-state simulations. Additionally, graphene integration in the heatsink lowered the SiC chip temperature rise by 11.5% compared to aluminum.

The optimized DC-link profile over WLTC reduced energy losses by 58% in the SiC system and 54% in the IGBT system compared to operating at a fixed 300 V DC-bus, with significant reductions also observed against a 450 V boosted DC-link. Furthermore, applying the optimal PWM frequency profile over WLTC lowered accumulated energy losses by up to 11% for SiC inverters and 4.2% for IGBT inverters compared to a fixed 10 kHz switching frequency.

Keywords: Electrified vehicles, Energy efficiency, SiC-based motor drives, MOSFET reverse conduction, Voltage-source inverters, Permanent magnet synchronous machine, Thermal stress, Lifetime prediction, Graphene assembled films, Liquid cooling, Conjugate heat transfer, Variable switching frequency, PWM-induced power losses, Variable DC-link.

List of Publications

This thesis is based on the following publications:

[A] **Sepideh Amirpour**, Torbjörn Thiringer, Dan Hagstedt, “Power Loss Analysis in a SiC/IGBT Propulsion Inverter Including Blanking Time, MOSFET’s Reverse Conduction and the Effect of Thermal Feedback Using a PMSM Model”. IECON 2020 The 46th Annual Conference of the IEEE Industrial Electronics Society, pp. 424-1430, Singapore, 2020.

[B] **Sepideh Amirpour**, Torbjörn Thiringer, Dan Hagstedt, “Energy Loss Analysis in a SiC/IGBT Propulsion Inverter over Drive Cycles Considering Blanking time, MOSFET’s Reverse Conduction and the Effect of Thermal Feedback”. 2020 IEEE Energy Conversion Congress and Exposition (ECCE), pp. 1505-1511, Detroit, MI, USA, 2020.

[C] **Sepideh Amirpour**, Torbjörn Thiringer, Dan Hagstedt, “Mission-Profile-Based Lifetime Study for SiC/IGBT Modules in a Propulsion Inverter”. 2021 IEEE 19th International Power Electronics and Motion Control Conference (PEMC), pp. 64-271, Gliwice, Poland, 2021.

[D] **Sepideh Amirpour**, Torbjörn Thiringer, Yasin Sharifi, Marco Majid Kabiri Samani, “Improving of Heat Spreading in a SiC Propulsion Inverter using Graphene Assembled Films”. Advances in Science, Technology and Engineering Systems Journal, vol. 6, no. 6, pp. 98-111 (2021).

[E] **Sepideh Amirpour**, Torbjörn Thiringer, “Mission-Profile-Based Lifetime study for SiC Module Chips using Graphene Films”. 2022 IEEE Energy Conversion Congress and Exposition (ECCE), pp. 1-7, Detroit, MI, USA, 2022.

[F] **Sepideh Amirpour**, Raik Orbay Torbjörn Thiringer, Majid Kabiri Samani Georgios Mademlis, Daniel Larsson, Andreas Andersson , “Highly thermal conductive graphene-based heatsink tailored for electric propulsion SiC-based inverter”. Applied Thermal Engineering, vol. 243, pp. 122548, ISSN 1359-4311 (2024).

[G] **Sepideh Amirpour**, Torbjörn Thiringer, Yu Xu, “Mapping an Optimum DC- Link Voltage across the Entire SiC-Based EV Drive Regions Using a

Synchronous Boost DC-DC Converter”. Published in SAE Technical Paper, 2024-01-2218, 2024.

[H] **Sepideh Amirpour**, Torbjörn Thiringer, Sima Soltanipour, Yu Xu, “Optimal DC-Link Voltage Mapping for SiC-Based EV Drives: Considering the Impact of a Synchronous Boost Converter”. *IEEE Access*, vol. 13, pp. 38239-38254, 2025.

[I] **Sepideh Amirpour**, Sima Soltanipour, Torbjörn Thiringer, Pranav Katta, “Adaptive Determination of Optimum Switching Frequency in SiC-PWM-based Motor Drives: A Speed-Dependent Core Loss Correction Approach”. Accepted for publication in *IEEE Open Journal of the Industrial Electronics Society*, 2025.

The following articles also reflect contributions made during this PhD study, though they are not directly related to this thesis:

[J] **Yu Xu**, A. Kersten, P. Ingelström, S. Amirpour, S. Klacar, D. Sedarsky, “Comparative study of efficiency improvement with adjustable DC-link voltage powertrain using DC-DC converter and Quasi-Z-Source inverter”. *2023 IEEE Transportation Electrification Conference and Expo, Asia-Pacific (ITEC Asia-Pacific)*, Chiang Mai, Thailand, 2023, pp. 1-5.

[K] **S. Akbari**, M. Eng, E. Adolfsson, K. Kostov, Q. Wang, S. Amirpour, T. Thiringer, J.K. Lim, M. Bakowski, D. Andersson, A. Kumar, “Vertically Aligned Graphene Layers as Thermal Interface Material for Gallium Nitride Semiconductor Components”. *2025 26th International Conference on Thermal, Mechanical and Multi-Physics Simulation and Experiments in Microelectronics and Microsystems (EuroSimE)*, Utrecht, Netherlands, 2025.

[L] **Y. Shao**, S. Amirpour, T. Thiringer, “Improving the Efficiency of SiC-based Inverter in BEV by Selecting the Switching Slew Rate for Optimisation of Switching Losses and Voltage Overshoot”. *Submitted to 2025 51st Annual Conference of the IEEE Industrial Electronics Society (IECON)*, Madrid, Spain, 2025.

Authorship Contributions

- [A] Sepideh Amirpour: Conceptualization, Methodology, Simulation, Writing – original manuscript. Torbjörn Thiringer: Supervision, Review & editing. Dan Hagstedt: Co-supervision, Review.
- [B] Sepideh Amirpour: Conceptualization, Methodology, Simulation, Writing – original manuscript. Torbjörn Thiringer: Supervision, Review & editing. Dan Hagstedt: Co-supervision, Review.
- [C] Sepideh Amirpour: Conceptualization, Methodology, Simulation, Writing – original manuscript. Torbjörn Thiringer: Supervision, Review & editing. Dan Hagstedt: Co-supervision, Review.
- [D] Sepideh Amirpour: Conceptualization, Methodology, Simulation, Experiments, Writing – original draft. Torbjörn Thiringer: Supervision, Review & editing. Yasin Sharifi: Preliminary investigation, Resources. Majid Kabiri Samani: Methodology, Review.
- [E] Sepideh Amirpour: Conceptualization, Methodology, Simulation, Writing – original draft. Torbjörn Thiringer: Supervision, Review & editing.
- [F] Sepideh Amirpour: Conceptualization, Methodology, Simulation, Experiments, Writing – original draft. Raik Orbay: Methodology, CFD/CHT Software & simulation, Writing – original draft. Torbjörn Thiringer: Supervision, Review & editing. Majid Kabiri Samani: Methodology, Writing original draft. Georgios Mademlis: Review and editing, Experiments. Daniel Larsson: Review. Andreas Andersson: Review.
- [G] Sepideh Amirpour: Conceptualization, Methodology, Simulation, Writing – original draft. Torbjörn Thiringer: Supervision, Review. Yu Xu: Review.
- [H] Sepideh Amirpour: Conceptualization, Methodology, Simulation, Writing – original draft. Torbjörn Thiringer: Supervision, Review. Sima Soltanipour: Energy loss calculation, Review. Yu Xu: Review.
- [I] Sepideh Amirpour: Conceptualization, Methodology, Simulation, Writing original draft. Sima Soltanipour: Conceptualization, Methodology,

Simulation, Writing original draft of speed-dependent core loss corrections. Torbjörn Thiringer: Supervision, Review, and editing. Pranav Katta: Preliminary investigation, Resources.

Acknowledgments

First and foremost, I would like to express my sincere gratitude to my main supervisor and examiner, Prof. Torbjörn Thiringer, for his invaluable support, feedback, patience, and time throughout this project. I would also like to thank my co-supervisor at Zeekr Technology Europe (formerly CEVT), Dr. Dan Hagstedt, for his support until the halfway point of this PhD, as well as Dr. Andreas Andersson and Johan Hellsing for their valuable support. I am also grateful to my managers, Sven Sjöberg, for his support in facilitating this opportunity during the early stages of this work, and Fredrik Nicklasson, for his continued support throughout the first half of this PhD journey.

Additionally, I would like to thank all my colleagues at Zeekr for their insights, and I express my gratitude to Dr. Shafiq Urréhman and Dr. John Bergström for their support with the administrative aspects of the project. I also thank my master thesis students for their contributions to preliminary investigations on some of the topics. A special thanks to Dr. Raik Orbay, Dr. Majid Kabiri Samani, Dr. Georgios Mademlis, and my fellow PhD researcher, Sima Soltanipour, for their contributions, suggestions, and assistance in some parts of this work. I also appreciate Dr. Anant Narula and Dr. Babak Alikhanzadehalamdari for their support, as well as the inspiring and talented community at Chalmers's Electric Power Engineering division, whose presence has made this journey even more enriching.

Finally, my deepest gratitude goes to my mother and my ever-living father for their unwavering support and encouragement throughout my educational life and to my loving family, especially Poorya and Rose Lily, for their patience and support over all these years.

The financial support given by the Swedish Energy Agency (Energimyndigheten), as well as Zeekr Technology Europe, is gratefully acknowledged.

Sepideh Amirpour
Göteborg, Sweden
December, 2024

Acronyms

BEV:	Battery Electric Vehicle
BLDC:	Brushless DC Motor
CAD:	Computer-aided Design
CFD:	Computational Fluid Dynamics
CHT:	Conjugate Heat Transfer
DBC:	Direct Bonded Copper
EDS:	Energy-dispersive X-ray Spectroscopy
EM:	Electric Machine
EMF:	Electromotive Force
EMI:	Electromagnetic Interference
EV:	Electric Vehicle
FEA:	Finite Element Analysis
FEM:	Finite Element Method
FOC:	Field-oriented Control
FVM:	Finite Volume Method
GFs:	Graphene-assembled Films
HTC:	Heat Transfer Coefficient
IM:	Induction Motor
IPM:	Interior Permanent Magnet
IPMSM:	Interior Permanent Magnet Synchronous Machine
MTPA:	Maximum Torque Per Ampere

MTPV:	Maximum Torque Per Volt
NEDC:	New European Driving Cycle
NPC:	Neutral Point Clamped
PMSM:	Permanent Magnet Synchronous Machine
PM:	Permanent Magnet
PV:	Photovoltaic
PWM:	Pulse Width Modulation
RMSE:	Root Mean Square Error
SEM:	Scanning Electron Microscopy
SiC:	Silicon Carbide
Si-IGBT:	Silicon-insulated-gate Bipolar Transistors
SPMSM:	Surface-mounted PMSM
SPWM:	Sinusoidal Pulse Width Modulation
SRM:	Switched Reluctance Motor
SVPWM:	Space Vector Pulse Width Modulation
THI:	Third Harmonic Injection
VSPWM:	Variable Switching Frequency Pulse Width Modulation
VSI:	Voltage Source Inverter
WBG:	Wide Band Gap
WLTC:	Worldwide harmonized Light vehicle Test Cycle

Mathematical symbols

A	Area of the power module layer
A_e	Effective cross-sectional area of inductance
A_L	Inductance factor
A_f	Effective cross-sectional area (frontal area)
α	Road inclination angle
α_c	Low-pass filter bandwidth
ar	Bond wire aspect ratio
B	Viscous damping constant
B_m	Amplitude of magnetic flux density of the machine
B_{pk}	Peak flux density
B_{peak}	Peak AC flux swing in inductance
C_{th}	Thermal capacitance
C_d	Aerodynamic drag coefficient
C_r	Dimensionless rolling resistance coefficient
c	Specific heat capacity
d	Power module layer thickness
D	Duty cycle of the DC-DC converter
E_{sw}	Switching energy loss
f	Fundamental frequency
f_{diode}	Diode chip thickness
f_{el}	Fundamental frequency of the electric machine

f_n	Space harmonic frequency
f_{sw}	Switching frequency
g	Gravitational constant
H	Magnetizing field
h	Heat transfer coefficient
I_D	Diode current
I_M	MOSFET current
I_{nom}	Nominal current
I_p	Peak phase current
i_d, i_q	Direct and quadrature axis current
i_{ref}	Reference current
i_s	Amplitude of the stator phase current
J	Rotational inertia of the shaft
J_e	Eddy current density in PMs
J_e^*	Complex conjugate of J_e
k	Kinetic energy of the cooling fluid
k_c	Coefficient of eddy current loss
k_e	Coefficient of excess loss
k_h	Coefficient of hysteresis loss
k_i	Current dependency exponent
k_v	Voltage dependency exponent
K	Thermal conductivity
μ	Dynamic viscosity of the cooling fluid

μ_r	Permeability
m	Mass
m	Modulation index
N_f	Number of cycles to failure of the device
N_i	Number of cycles
n_p	Pole pair number of the machine
n_s	Mechanical synchronous speed of the stator field
Ω_r	Mechanical speed of the rotor
p	Cooling fluid pressure
P_h	Hysteresis loss
P_L	Inductance core loss density
P_s	Specific power loss
Q	Heat flow
q	Heat flux
q_v	Volumetric heat generation rate per unit volume
R_s	Stator winding resistance
R_d	Diode on-state resistance
R_f	IGBT on-state resistance
R_{on}	MOSFET on-state resistance
R_{th}	Thermal resistance
$R_{th,jc}$	Thermal resistance from the junction to case
$R_{th,cs}$	Thermal resistance from case to sink
$R_{th,sf}$	Thermal resistance from sink to fluid

R_g	Gear ratio
r_t	Tire radius
ρ	Density
ρ_a	Air density in vehicle dynamics
σ	Conductivity of PM material
T_c	Power module case/baseplate temperature
T_e	Electromagnetic torque
T_L	Load torque
T_f	Fluid temperature
T_j	Semiconductor Junction temperature
T_{jm}	Mean junction temperature
T_s	Heatsink temperature
t	Fundamental period of time
t_{blanking}	Blanking time
t_{MP}	Mission profile period
t_{ON}	Thermal cycling period
τ	Modulation Duty Cycle
tr	Trace of a tensor in 3 dimensions
dv/dt	Slew rate
u_d, u_q	Direct and quadrature axis voltages
V	Volume of PM material
V_{batt}	Battery terminal voltage
V_d	Diode voltage drop

V_{dc}	DC-link voltage
V_e	Effective volume of the core of inductance
V_{nom}	Nominal voltage
V_0	Zero-sequence component
V_a^*, V_b^*, V_c^*	Phase reference voltages
V_T	IGBT voltage drop
φ	Angle of displacement power factor
ψ_m	Magnetic flux linkage
ψ_d, ψ_q	Stator flux linkage in dq -frame
ω	Angular frequency
ω_r	Electrical speed of the rotor
∇T	Temperature gradient
∇K	Thermal conductivity tensor
u	Velocity vector
\mathbf{f}	Body force vector acting on the cooling fluid domain
$\frac{\delta T}{\delta t}$	Difference in temperature with respect to time

Contents

Abstract	i
List of Publications	iii
Authorship contributions	v
Acknowledgements	vii
Acronyms	ix
Mathematical symbols	xi
I Overview	1
1 Introduction	3
1.1 Background	3
1.2 Previous work and research gaps	4
1.3 Purpose of the thesis and contributions	7
2 Key Theories and Concepts	11
2.1 SiC vs. Si semiconductors in EVs	11

2.2	Three-phase Inverter	12
2.2.1	Inverter control method	13
2.2.2	Inverter power loss analysis	17
2.2.3	Lifetime prediction of semiconductors	21
2.3	Electric machine	23
2.3.1	Equivalent circuit model	24
2.3.2	Control strategy	26
2.3.3	Power loss analysis	30
2.4	Energy loss analysis over drive cycle	32
2.5	Optimal system-level strategies	33
2.5.1	Optimum switching frequency over drive regions	33
2.5.2	Optimum DC-link voltage over drive regions	34
2.5.3	Graphene: high thermal conductivity material	38
3	Case studies	41
3.1	Simulation setups	41
3.1.1	Case setup 1	42
3.1.2	Case setup 2	44
3.1.3	Case setup 3	47
3.1.4	Case setup 4	49
3.2	Experimental setup	59
3.3	Vehicle model and drive cycle	61
4	Power and Energy Loss Analysis	63
4.1	Overview	63
4.2	Method	64
4.2.1	MOSFET reverse conduction	64
4.2.2	Thermal feedback	68
4.3	Key results and discussion	69
5	Lifetime Prediction Analysis for SiC- and IGBT-Based Inverters	73
5.1	Overview	73
5.2	Method	74
5.2.1	Thermal calculation model	74
5.2.2	Rainflow counting	75
5.3	Key results and discussion	78

- 6 Thermal Management Enhancements Using Graphene 81**

 - 6.1 Overview 82
 - 6.2 Method 83
 - 6.2.1 Graphene assembled film in the module packaging . . . 83
 - 6.2.2 Graphene-based heat exchange unit including pin fins in the heatsink 85
 - 6.3 Key results and discussion 86
 - 6.3.1 Steady-state thermal computation of the power module with/without graphene layer 86
 - 6.3.2 Transient thermal computation of the power module, with/without graphene layer using WLTC driving cycle 90
 - 6.3.3 Results of CHT computations applied to the designed aluminum and graphene pin fins based heatsinks 93
 - 6.3.4 Experimental validation of implemented CHT on the designed aluminum heatsink 98

- 7 Optimum DC-Link Voltage Determination for Electric Driveline 103**

 - 7.1 Overview 103
 - 7.2 Method 105
 - 7.3 Key results and discussion 107

- 8 Optimum Switching Frequency Determination for Electric Driveline 123**

 - 8.1 Overview 123
 - 8.2 Method 125
 - 8.2.1 Speed-dependent core loss calculation 125
 - 8.2.2 Optimum switching frequency determination 129
 - 8.3 Key results and discussion 131

- 9 Concluding Remarks and Future Work 141**

 - 9.1 Conclusions 141
 - 9.2 Future work 143

- References 145**

- II Papers 157**

 - A Paper A A1**

B Paper B	B1
C Paper C	C1
D Paper D	D1
E Paper E	E1
F Paper F	F1
G Paper G	G1
H Paper H	H1
I Paper I	I1

Part I

Overview

CHAPTER 1

Introduction

1.1 Background

Over recent years, CO_2 emissions have been a major focus for vehicle OEMs, especially in the EU, where increasingly stringent reduction targets are imposed. The New European Driving Cycle (NEDC) evaluates car emissions and fuel economy. Reports in [1] show the CO_2 emissions normalized to the NEDC over time, indicating that the EU target dropped from 170 g CO_2 /km in 2000 to 90 g CO_2 /km in 2021, with similar trends observed globally.

The ongoing discussions propose more ambitious CO_2 standards for new cars and vans. In the EU, compared to the 2021 targets, the emissions of new passenger cars must fall by 55% by 2030 and reach zero by 2035 [2], underscoring the growing market demand for well-developed and highly efficient electrified vehicles.

Hence, the efficiency of the electric propulsion system has become a critical focus for electric vehicles (EVs). Improved efficiency not only reduces energy consumption and CO_2 emissions but also extends driving range and lowers operating costs. These demands have driven extensive research and development in advanced power electronics, particularly in propulsion invert-

ers utilizing technologies such as silicon carbide (SiC) and conventional silicon insulated-gate bipolar transistors (Si-IGBTs), as well as progressive control strategies aimed at optimizing the overall performance of electric powertrains.

Wide-bandgap (WBG) SiC power modules stand out as one of the latest and most promising advances, offering notable advantages over Si-IGBTs by their faster switching transitions, lower conduction losses, and superior thermal characteristics. This thesis focuses on improving the efficiency of a voltage source propulsion inverter using SiC versus Si power modules, and employing optimized strategies along with thermal analyses that utilize innovative heat-spreading materials. The inverter is integrated with an interior permanent magnet (IPM) electric machine—the most common e-machine type in battery electric vehicles—to facilitate a comprehensive system-level efficiency analysis.

1.2 Previous work and research gaps

Electric vehicles require increasingly efficient powertrains, where inverters and electric machines are the key to overall system performance. Achieving high efficiency involves selecting the right solution, design objectives, variables, modeling approaches, control techniques, and optimization algorithms. When it comes to reducing power and energy losses particularly in the propulsion inverter, as mentioned earlier, new generations of WBG SiC power modules have offered a promising alternative to conventional silicon IGBTs. However, improvements in wide-bandgap technologies, faster-switching frequencies, and ever-evolving drive cycle requirements continuously demand precise and comprehensive modeling of losses and robust lifetime estimations—gaps not fully resolved in the current literature or industry practice. Consequently, the research questions still guide meaningful investigations for more efficient and durable EV powertrains.

The following research gaps concerning electric driveline efficiency have been identified in this thesis:

- I. By improving the efficiency of the propulsion inverter, the overall powertrain efficiency also increases [3], leading to a lighter cooling system, higher power density, and extended range. Several studies have compared SiC MOSFETs and traditional Si IGBTs for EV applications, examining energy efficiency and losses under various drive cycles [4]–[6], temperature effects through FEM analysis [7], and the MOSFET’s

reverse conduction in an electro-thermal model [8]. However, comprehensive comparisons that numerically quantify the impact of thermal feedback on power loss calculations across a wide operating region of a permanent magnet synchronous machine (PMSM)—while addressing blanking time and MOSFET reverse conduction—remain an ongoing challenge in EV powertrain design. Establishing a clear baseline of the relevant loss factors in SiC- vs. Si-IGBT-based inverters is, therefore, essential for understanding where and why underestimations or inaccuracies might occur, if these factors are overlooked.

- II. Meeting design specifications for reliability and cost in SiC-based inverters remains challenging compared to Si-IGBTs. Higher temperature fluctuations in SiC MOSFETs (chips and dies) due to their higher current density capability coupled with higher thermal conductivity make lifetime prediction a critical concern [9]. While numerous studies address semiconductor reliability—particularly mission-profile-based lifetime prediction—in photovoltaic (PV) and wind turbine applications [10]–[12], fewer extend this analysis to electric drive applications, and often focusing on Si-IGBTs [13]–[15]. Moreover, only a limited number of works examine SiC devices in PV and wind energy converters [9], [16], [17], and studies on SiC for EV applications are notably scarce. This gap becomes more pronounced when it comes to comparing the mission-profile-based lifetime for SiC and IGBT propulsion inverters, thereby demonstrating how operating conditions, dynamic loads, and thermal variations throughout the drive cycle fundamentally influence long-term performance and reliability.
- III. Recognizing heat as a major stress factor, especially in SiC switching devices, underscores the ongoing challenge of developing innovative thermal solutions to mitigate temperature-induced inefficiencies and stresses. One approach to address this issue is to enhance thermal conduction within the power module by effectively cooling the semiconductor chips. By integrating heat-spreading materials with excellent mechanical and thermal properties into the packaging, heat is efficiently diverted away from the power devices, resulting in a lower operating temperature for the system. Consequently, both the research community and manufacturers have devoted significant effort to exploring new high-thermal-conductivity materials, such as graphene, as effective heat

spreaders—efforts documented in [18], [19]. Additionally, studies in [20]–[22] have specifically investigated the use of graphene in power module packaging, with further interesting research reported in [23], [24]. However, these applications are limited in scope and do not offer a comprehensive electrical and thermal analysis of SiC semiconductor power modules from the chip level through the various material layers particularly when it comes to EV applications.

- IV. Incorporating graphene into advanced cooling devices for power electronics offers a second innovative solution to optimize thermal conditioning systems through enhanced heat transfer. A new class of graphene-enhanced heat pipes is introduced in [25], which substantially improves the heat dissipation capacity above that of copper-based commercial heat pipes. In [26], a graphene-assembled film integrated heatsink with water cooling is used, in which the graphene film was attached to the surface of a Li-ion battery cell to achieve efficient cooling of the battery cell. Another experimental set-up of a graphene-based heatsink, using a cooling fan is demonstrated in [27] to address the overheating issues in power electronics. Furthermore, when it comes to thermal simulations using computational fluid dynamics (CFD), the level of detail in many publications is not explicitly specified. For instance, in [28], [29] simulations estimating the temperature of a pin-fin equipped power module are conducted using fins, but without employing conjugate heat transfer (CHT); predetermined heat transfer coefficients (HTC) are used instead. In [30], an electrothermal design of a discrete GaN-based converter for integrated modular motor drives utilizes CFD without CHT. Concluding all the above-mentioned context, to the author’s knowledge, neither a comprehensive multidisciplinary study has been found in the existing literature that incorporates graphene into cooling system of a SiC power module in EVs, nor utilizes a full CHT approach for the thermal analysis.
- V. Fluctuations in battery voltage also create a notable challenge for EV powertrains, reducing energy efficiency and overall driving performance, as noted in [31]–[33]. A viable solution is to dynamically adjust the DC-link voltage across various driving conditions to optimize powertrain efficiency. Instead of connecting the battery directly to the inverter, a DC-DC converter supplies power to the traction inverter. However,

integrating a DC-DC converter into the powertrain system adds additional passive components, increases system complexity, raises costs, and results in reduced reliability, as highlighted in the literature [34], [35]. Several studies have investigated improving powertrain efficiency by optimizing the DC-link voltage using DC-DC converters [36]–[41]. Despite valuable research, a comprehensive loss analysis remains lacking. Losses from the DC-DC converter—including switching and inductance losses—are often underestimated, and the impact of temperature variations on power electronics is rarely evaluated. Consequently, the decision to include a DC-DC converter is not clearly justified.

- VI. SiC switching devices, with their faster transitions and higher frequency capabilities, benefit PMSMs by reducing harmonic content and current ripples, thereby lowering motor losses. However, too high a switching frequency increases inverter losses, making optimization essential for maximizing the overall efficiency of motor drive systems. Several studies have examined variable switching frequency pulse width modulation (VSFPWM), where the carrier frequency of the PWM is adjusted based on prediction models to control current ripple and reduce inverter switching losses [42]–[45]. However, these studies rely on analytical PMSM models and manufacturer-supplied loss data instead of detailed FEM-based loss maps for improved accuracy, and they typically use fixed iron loss coefficients in their calculations. [46] presents a FEM analysis of PWM power losses in an interior permanent magnet (IPM) machine driven by a WBG-based inverter, employing a dynamic Jiles-Atherton (J-A) model—as proposed in [47]—to estimate the PWM-induced core losses. Although the loss analysis is detailed, the study is limited to only a few operating conditions and does not examine how core losses vary with frequency. Furthermore, at the system level, an optimized switching frequency profile covering the entire torque-speed range, or a complete drive cycle pattern has not been fully explored.

1.3 Purpose of the thesis and contributions

This thesis focuses on improving the efficiency of an electric powertrain configured with an IPM electric machine and a three-phase voltage source inverter (VSI). It offers optimal control strategies, comprehensive thermal simulations,

and detailed evaluations of power and energy losses to comprehensively analyze the entire drive range.

The main contributions of this work are as follows:

- I. Quantification of the significance of thermal feedback on the power and energy losses in SiC vs. IGBT devices. This should be done by focusing on device-level parameters—thermal dynamics, switching characteristics, and conduction mechanisms through a comprehensive numerical loss analysis—then extending the analysis from device-level to system-level, using real-world drive cycles. (Paper A & B)
- II. Demonstration of how operating conditions and thermal variations throughout the drive cycle affect the lifetime of SiC vs. IGBT-based devices in EV applications, using mission-profile-based lifetime analysis. (Paper C)
- III. Demonstration of how graphene’s excellent thermal properties enable efficient heat spreading across the SiC MOSFET chips and direct bonded copper (DBC) layers within the power module, conducting a detailed electrical and thermal analysis of a SiC power module from the chip level through the various material layers. Then, demonstrating how these temperature reductions translate into an extended device lifetime, particularly in high-power applications. (Paper D & E)
- IV. Demonstrating how graphene—integrated into the water jacket design—can challenge conventional techniques and improve heat conduction and temperature distribution in semiconductor modules, implementing a detailed CHT methodology within a multidisciplinary framework. The analysis accurately models SiC MOSFETs from the chip level through the fluid. (Paper F)
- V. Reasonably identifying the optimal DC-link voltage across the entire drive range by performing a comprehensive system-level loss analysis. The analysis integrates FEM-based loss modeling of a PMSM as well as power electronics losses from the linked converter-inverter SiC vs. IGBT-based systems under variable DC-link voltages. (Paper G & H)
- VI. Implementing a comprehensive coupled time-stepping FEM analysis that integrates both PMSM and inverter losses in real-time simulation, captures their interaction with varying PWM switching frequencies. The

analysis accounts for e-machine space harmonics, PWM-induced harmonics, current controller interactions as well as dynamically updated core loss coefficients based on the specific supply frequencies, closely mimicking a real-world implementation. Consequently, generating full powertrain loss maps as the primary measure to reliably determine the optimal switching frequency across all SiC vs. IGBT system drive regions. (Paper I)

In summary, the road-map of this thesis begins by identifying where and why losses occur in electric drive systems using SiC versus Si devices and how these losses evolve under real conditions. It then tackles these challenges by proposing innovative cooling material solutions and optimized strategies through a detailed, multidisciplinary analysis, ultimately evaluating the benefits in reduced energy losses and extended device lifetime.

CHAPTER 2

Key Theories and Concepts

This chapter presents the theoretical foundations and mathematical models for the analysis discussed in this thesis, focusing on the efficiency of the electric powertrain outlined in Chapter 1. These models will be applied throughout the subsequent chapters.

2.1 SiC vs. Si semiconductors in EVs

In response to the demand for reducing power and energy losses in electrified vehicle (EV) applications, silicon carbide (SiC) semiconductors are increasingly favored over traditional silicon (Si) semiconductors, particularly in the inverters, due to their superior performance characteristics, as summarized in the following points [3]–[5]:

1. **Higher efficiency:** SiC devices exhibit lower switching losses because of faster transition times as well as lower conduction losses. Without the P-N junction the conduction losses are low at low current and, by utilizing the MOSFETs' reverse conduction capability, the inverter conduction losses can be lowered. This improvement in inverter efficiency leads to

an increase in e-vehicle driving range.

2. **Improved thermal performance:** In addition to lower losses—which reduce the need for extensive cooling systems—the higher thermal conductivity of SiC allows heat to be dissipated more efficiently, enabling operation at higher temperatures.
3. **Higher power density:** The ability of SiC to operate at higher frequencies allows for smaller passive components, along with improved thermal properties, resulting in more compact and lighter inverters.
4. **Higher voltage operation:** Due to higher blocking voltages, SiC devices can handle higher operating voltages, making them suitable for 800 V EV architectures, which can reduce charging times and improve efficiency.

However, SiC devices are currently more expensive than their Si counterparts, which can impact the overall cost of EVs. In addition, the production of SiC components involves more complex processes, potentially affecting yield and scalability [48], [49]. To conclude, while SiC semiconductors offer significant performance benefits for EV inverters, considerations such as cost and manufacturing challenges remain. However, as production scales and technology advances, SiC appears ready for broader adoption in electric vehicles.

2.2 Three-phase Inverter

Two-level three-phase voltage source inverters (VSI) in EV applications are the key power electronic converters that control the AC power supplied to the electric machine, typically a permanent magnet synchronous machine (PMSM) or an induction machine. They convert the DC voltage from the electric vehicle battery into a three-phase AC output with variable frequency and amplitude. Furthermore, they enable precise machine speed control and torque control by modulating the AC waveform using techniques like pulse width modulation (PWM) which will be explained in the next subsection.

The inverter consists of three legs (one for each phase of the electric machine), with two switches (usually IGBTs or SiC MOSFETs) per leg, illustrated in Figure 2.1. It is called two-level because it switches the DC input voltage into two levels ($+V_{dc}/2$ and $-V_{dc}/2$) for each phase. The topology is

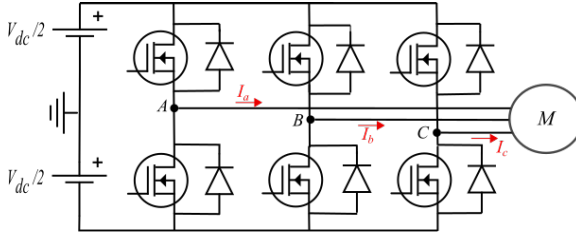


Figure 2.1: Two-level three-phase voltage source inverter topology.

simple and cost-effective with high reliability for electric vehicle propulsion systems, compatible with control strategies like field-oriented control (FOC) and, as well, has high efficiency. Hence, it is a widely used inverter topology due to its balance of performance, simplicity, and efficiency.

In addition to two-level inverters, alternative topologies such as multi-level inverters and neutral point clamped (NPC) inverters have attracted increasing interest in automotive applications [50]–[52]. The studies suggest that multi-level inverters can achieve higher efficiency than two-level designs. However, they come with notable drawbacks, including a higher component count (e.g., switches and gate drivers) and increased control complexity [50], [51]. As a result, there is still no clear agreement on the most suitable inverter topology for electric vehicles.

2.2.1 Inverter control method

Pulse Width Modulation (PWM) is a widely used technique in power electronics, including electric vehicle applications, to control the voltage and current supplied to devices like electric machines. It works by rapidly switching a signal between on and off states, varying the proportion of time the signal stays on—the duty cycle—to achieve the desired average output voltage. Two types of PWM strategies are mostly used in this work as follows.

2.2.1.1 Sinusoidal PWM

In sinusoidal PWM (SPWM), a sinusoidal reference signal is compared with a high-frequency triangular carrier signal. As shown in Figure 2.2, the ampli-

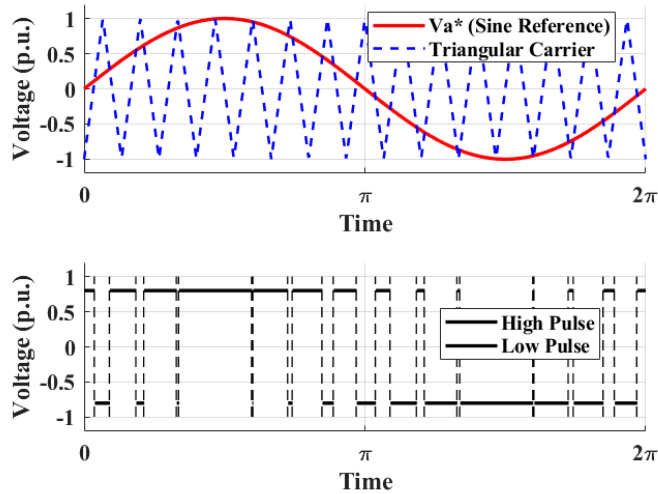


Figure 2.2: Sinusoidal phase reference with the triangular carrier signal and the generated PWM waveform.

tude of the triangular carrier wave equals half of the DC-link voltage. When the reference phase voltage surpasses the triangular wave, the upper switch turns on while the lower switch turns off, causing the current to flow through the upper switch. Conversely, when the triangular wave exceeds the reference voltage, the lower switch turns on, and current flows through the lower switch. This process generates a PWM waveform with uniform pulse widths but varying intervals, serving as the control signal for the inverter, resulting in a near-sinusoidal output voltage. As illustrated in the figure, the point where the sine wave intersects with the triangular wave determines the timing of the state transitions.

Note that while generating a sinusoidal phase voltage with a two-level inverter, the peak amplitude is constrained by the DC bus voltage. Each inverter leg produces an amplitude voltage $V_{dc}/2$. The relative amplitude of the output voltage is quantified by the modulation index (m), where $m = 1$ represents the maximum sinusoidal voltage amplitude achievable without distortion. For $m > 1$, the sinusoidal output voltage is clipped to $\pm V_{dc}/2$, introducing low-order harmonics that are challenging to filter. When the voltage reference exceeds the capabilities of the DC bus, the inverter operates in the over-modulation

region, leading to increased distortion and potential performance degradation [53], [54].

To increase the operation area without over-modulation and clipping in two-level inverters, several solutions are available [53], [54]: increasing the DC bus voltage to enable higher peak sinusoidal output without exceeding the modulation index limit; adopting multilevel inverter topologies (e.g., three-level or neutral-point clamped inverters) to extend the modulation index range; or employing advanced techniques like third harmonic injection (THI) or space vector pulse width modulation (SVPWM) to enhance DC bus voltage utilization by optimizing the reference waveform.

2.2.1.2 Sinusoidal PWM with min/max injection

SVPWM, used in this work, is equivalent to SPWM with min/max injection [53], [54]. This method (SPWM with min/max injection) adds a triangular zero-sequence component (triplen harmonics), V_0 , to the sinusoidal reference, distorting the phase voltage references. Reducing the peak voltage of the reference compared to a pure sinusoidal reference allows the modulation index to increase to $m = 2/\sqrt{3} \approx 1.15$ before hitting the limits of the DC-link voltage.

$$V_0 = \frac{\max(V_a^*, V_b^*, V_c^*) + \min(V_a^*, V_b^*, V_c^*)}{2} \quad (2.1)$$

where V_a^* , V_b^* and V_c^* are the phase reference voltages. Figure 2.3 illustrates the concept. The zero-sequence component is shown in the upper figure, taking the shape of a triangular wave using the proposed method, and the lower one depicts the results of adding the zero-sequence component to the sinusoidal references.

2.2.1.3 PWM-induced harmonics

The PWM technique generates switching harmonics in the voltage waveform of the inverter, feeding the permanent magnet synchronous motor (PMSM) in the EV powertrain. These harmonics arise due to non-sinusoidal switching (the PWM inverter's output is a series of pulses instead of a smooth sine wave), with dominant components around the PWM carrier frequency and its multiples. Harmonics in the current cause fluctuations in torque, increasing core, copper, and eddy current losses in the motor, thereby decreasing efficiency.

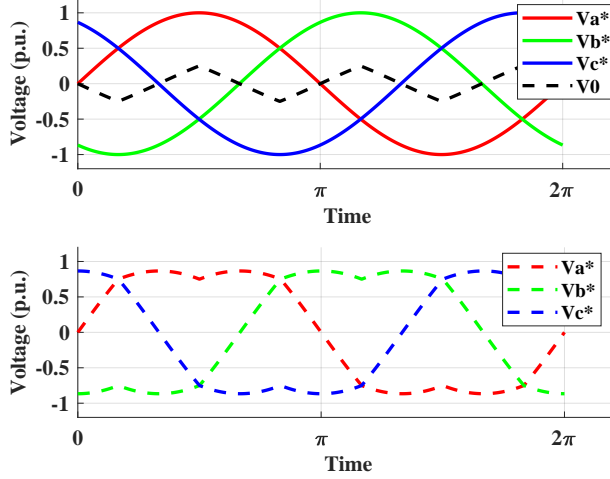


Figure 2.3: Sinusoidal phase references with the zero-sequence component and resulting phase reference obtained by addition the zero-sequence component.

In addition, harmonic interactions induce mechanical vibrations and acoustic noise in the machine. Hence, mitigating these harmonics (e.g., through filters or advanced control techniques) is crucial to optimize performance.

Analyzing PWM-induced harmonics in a PMSM fed by a three-phase VSI involves several steps, including time-domain and frequency-domain analysis, analytical methods, finite element analysis (FEA) using simulation tools, and experimental measurements to predict harmonic content and assess its impact on PMSM performance.

In the frequency-domain, Fourier analysis is a fundamental method to study and quantify the harmonic content of signals, such as the PWM waveforms and the resulting voltage and current in a PMSM. The basic of Fourier analysis is that it decomposes a non-sinusoidal periodic signal into sinusoids of various frequencies and harmonic components. This means that any periodic signal $f(t)$ can be expressed as

$$f(t) = a_0 + \sum_{n=1}^{\infty} [a_n \cos(n\omega t) + b_n \sin(n\omega t)] \quad (2.2)$$

where, n is harmonic order, a_0 , a_n , and b_n are Fourier series coefficients and $\omega = 2\pi f_1$ is the angular frequency of the lowest frequency component.

The higher the current ripple, the more significant the harmonic content in the current waveform. These harmonics generate corresponding harmonics in the magnetic flux density, which will be superimposed on the fundamental flux component, leading to an overall increase in flux density swings. Harmonics can also lead to torque ripple, causing mechanical vibrations and noise.

Therefore, accounting for these harmonics is crucial, especially if the machine operates across a wide range of switching frequencies. Additionally, selecting the appropriate switching frequency across the drive region is important for reducing current ripples and minimizing the associated harmonic contents.

2.2.2 Inverter power loss analysis

In each phase leg, power losses are affected by the current waveform, which includes both the fundamental component and the current ripple. The fundamental component depends on the type of load (e.g., resistive, inductive, or motor loads), while the current ripple is mainly influenced by the switching frequency. The overall losses in a voltage source inverter primarily include conduction losses and switching losses. The following gives a breakdown.

2.2.2.1 Conduction losses

In general, conduction losses occur due to the voltage drop across the switching devices and diodes when they conduct current. Based on the analytical approach for the SiC MOSFETs, the average conduction losses over a fundamental period of the phase current can be calculated as

$$P_{\text{cond,MOS}} = \frac{1}{2\pi} \int_0^{2\pi} R_{\text{on}} I_M^2(\alpha) \tau(\alpha) d\alpha \quad (2.3)$$

where R_{on} is the MOSFET on-state resistance, I_M is the MOSFET current, $\alpha = 2\pi ft$, f is the fundamental frequency and τ is the duty cycle which can be expressed as a function of α as

$$\tau(\alpha) = \frac{1}{2}(1 + m \sin \alpha) \quad (2.4)$$

where m is the modulation index [55]. Likewise, the diode conduction losses can be derived as

$$P_{\text{cond,D}} = \frac{1}{2\pi} \int_0^{2\pi} (R_d I_D^2(\alpha) + V_d I_D(\alpha)) \tau(\alpha) d\alpha \quad (2.5)$$

where the voltage drop, V_d , and the on-state resistance, R_d , can be obtained from the datasheet information of the forward characteristics of the diode. Finally, I_D is the diode current.

- **MOSFETs' Reverse Conduction:**

Unlike Si IGBTs, where the total reverse current of the switch flows through an anti-parallel diode, MOSFETs can also conduct reverse current due to their reverse conduction ability. If the MOSFET's drain-to-source voltage exceeds the corresponding diode forward voltage, parallel conduction of the two devices occurs. The diode may be either a separate diode or the intrinsic one. This leads to a significant reduction in the total conduction losses of the switch position. The currents flowing through the MOSFET and diode during reverse conduction can be obtained as

$$I_M = \frac{R_d I_p \sin(\alpha - \varphi) - V_d}{R_d + R_{\text{on}}} \quad (2.6)$$

$$I_D = \frac{R_{\text{on}} I_p \sin(\alpha - \varphi) + V_d}{R_d + R_{\text{on}}} \quad (2.7)$$

where φ is the angle of displacement power factor and I_p is the peak phase current [56], [57].

For the Si-IGBT module, the conduction losses of the IGBT and diode can be calculated by integrating the product of the current flowing through the device and voltage drop over it [58], [59], resulting in the expressions,

$$P_{\text{cond,IGBT}} = \frac{1}{2} (V_T \frac{I_p}{\pi} + R_f \frac{I_p^2}{4}) + m \cos \varphi (V_T \frac{I_p}{8} + \frac{1}{3\pi} R_f I_p^2) \quad (2.8)$$

$$P_{\text{cond,D}} = \frac{1}{2} \left(V_d \frac{I_p}{\pi} + R_d \frac{I_p^2}{4} \right) - m \cos \varphi \left(V_d \frac{I_p}{8} + \frac{1}{3\pi} R_d I_p^2 \right) \quad (2.9)$$

where R_f is the IGBT on-state resistance and V_T is the IGBT voltage drop.

- **Blanking Time:**

Blanking time is the interval during which both the upper and lower switches in the same phase leg of a PWM-controlled inverter are turned off, so that only the diode conducts. This measure helps prevent shoot-through faults. Its impact can be accounted for in the inverter's conduction power losses. To incorporate the impact of blanking time directly, an equivalent duty cycle can be introduced into equation (2.4), as follows. This equivalent duty cycle is subsequently used in the conduction loss equations mentioned earlier.

$$\tau_{\text{eq}}(\alpha) = \tau(\alpha) - t_{\text{blanking}} f_{\text{sw}} = \frac{1}{2} (1 - 2t_{\text{blanking}} f_{\text{sw}} + m \sin \alpha) \quad (2.10)$$

where f_{sw} is the switching frequency. During the blanking time, the diode solely conducts the current, increasing the total conduction losses of the diodes in the inverter.

2.2.2.2 Switching losses

The inverter switching losses can be determined as the product of switching energies and switching frequency with respect to the conducted phase current and the DC-link voltage. During every turn-on and turn-off event, a loss occurs in the switch and its anti-parallel/body diode. As mentioned above, the switching energies of the Si-IGBTs and diodes are generally higher than those of the SiC devices. Switching losses can be calculated analytically in a MOSFET and a diode by the expression as

$$P_{\text{sw,MOSFET,IGBT,Diode}} = f_{\text{sw}} \cdot E_{\text{sw}}(I_{\text{nom}}, V_{\text{nom}}) \cdot \left(\frac{1}{\pi} \frac{I_p}{I_{\text{nom}}} \right)^{k_i} \cdot \left(\frac{V_{\text{dc}}}{V_{\text{nom}}} \right)^{k_v} \quad (2.11)$$

where E_{sw} is switching energy loss during turn-on, turn-off and diode reverse recovery, I_p is the peak phase current, I_{nom} and V_{nom} are nominal current and voltage values and k_i , k_v are current and voltage dependency exponents,

respectively [58]. In the numerical implementation in this study, the switching loss is calculated at every switch-on and switch-off event of the device as

$$P_{\text{sw}} = \frac{\sum E_{\text{sw}}}{t} \quad (2.12)$$

where t is the fundamental period of time.

2.2.2.3 Lumped parameter thermal model of inverter

The thermal network of an inverter is a critical aspect of its design, as it determines how efficiently heat is managed within the system. Effective thermal management ensures reliable operation, prevents overheating, and extends the lifespan of the inverter components.

The lumped parameter model is a simplified representation of a physical system, where the system's distributed properties (like temperature, heat flow, or electrical resistance) are approximated as discrete and uniform elements. This model is widely used in thermal, electrical, and mechanical systems for ease of analysis and simulation. In the context of an inverter, the lumped parameter model represents heat transfer and storage within the system. It simplifies the complex heat transfer mechanisms into a manageable equivalent network of thermal resistances R_{th} and thermal capacitances C_{th} . Thermal resistance represents the system's resistance to heat flow and thermal capacitance represents the system's ability to store heat,

$$R_{\text{th}} = \frac{\Delta T}{Q} \quad (2.13)$$

$$C_{\text{th}} = \frac{m \cdot c}{\Delta T} \quad (2.14)$$

where ΔT is the temperature difference, Q is the heat flow, m is mass and c is specific heat capacity.

The thermal resistors and capacitors are connected in Foster or Cauer configurations. The Foster network represents a system as a series connection of thermal RC elements, each consisting of a thermal resistance R_{th} and a thermal capacitance C_{th} . The Cauer model, unlike the Foster model, alternates between thermal resistances and thermal capacitances in a ladder network

configuration. It mimics the physical reality of a layered thermal system (e.g., heat conduction through multiple layers of material).

However, while lumped parameter networks are powerful for many applications, their underlying assumptions and simplifications can become limiting when spatial distribution, high-frequency phenomena (e.g., the skin effect in conductors, dielectric losses in capacitors, or eddy currents in inductors), or complex geometries play a dominant role. In such cases, more detailed approaches—such as finite element analysis (FEA) and computational fluid dynamics (CFD)—can offer more accurate modeling of localized effects and non-uniform heat transfer.

Conjugate heat transfer (CHT), as an extension of CFD, further enhances these capabilities by considering the interaction between fluid flow and heat transfer in both fluids and solid materials. By combining the thermal analysis of solid components with the fluid dynamics of the surrounding media, CHT provides a more comprehensive perspective on thermal-fluid problems, thereby overcoming the inherent limitations of lumped parameter networks in complex scenarios.

2.2.3 Lifetime prediction of semiconductors

Reliability and durability are critical considerations when choosing semiconductors for converters. These factors directly impact the efficiency, maintenance, and overall system stability [60]. In power semiconductor modules, bond wire degradation and solder fatigue are considered to be the main long-term failure mechanisms due to temperature-induced mechanical stress [9]. Since the thermal cycling stresses which in the range of seconds are mainly responsible for the bond wire damages [11], then this failure is worth being considered for the lifetime analysis. Different lifetime methods for the Si-IGBT modules have been provided in [12]–[14] and for SiC-MOSFET modules the research is still ongoing [61], [62]. For instance, the state-of-the-art Si-based lifetime model in [12] provides a reasonable estimation for the SiC-MOSFET modules' lifetime. Based on the model presented in [12], the number of cycles

to failure N_f of the devices can be represented as

$$N_f = A \times (\Delta T_j)^\alpha \times (ar)^{\beta_1 \Delta T_j + \beta_0} \times \left[\frac{C + (t_{ON})^\gamma}{C + 1} \right] \times \exp\left(\frac{E_a}{k_b \times T_{jm}}\right) \times f_{diode} \quad (2.15)$$

where A , α , β_0 , β_1 , γ and C are the model parameters given in Table 2.1 as shown in [62]. ΔT_j is the semiconductor junction temperature swing, ar is the bond wire aspect ratio, f_{diode} is the diode chip thickness which is considered to be 0.6204 for the diodes and unity for the MOSFETs/IGBTs. t_{ON} is the cycling period.

Table 2.1: Lifetime model parameters

Parameter	Value	Parameter	Value
A	3.4368×10^{14}	α	-4.923
β_0	1.942	ar	0.31
β_1	-9.012×10^{-3} 1/K	C	1.434
E_a	6.606×10^{-2} eV	γ	-1.208
k_b	8.62×10^{-5} eV/K	t_{ON}	1 s

The damage modeling can be determined using the Miner's rule [63] to accumulate the damage D on the switching devices under a single run of the used mission profiles (like drive cycles in this work) as

$$D = \sum_i \frac{N_i}{N_{fi}} \quad (2.16)$$

where N_i , the number of cycles at stress level ΔT_{ji} , which can be extracted when applying the rainflow counting algorithm [64] on the temperature time series (temperature profiles). N_{fi} , the expected number of cycles to failure for the i th cycle can be calculated from (2.15).

The expected lifetime can be calculated from the damage caused by temperature cycles during the considered mission profile period t_{MP} as

$$LF = \frac{t_{MP}}{D} \quad (2.17)$$

2.3 Electric machine

Electric machines are at the core of electric vehicle (EV) powertrains, converting electrical energy into mechanical energy for propulsion. Key types of electric machines in EVs can be listed as follows.

- **Induction Motors (IM):** Widely used due to robustness and lower cost and less efficient compared to PMSM, especially at lower speeds.
- **Permanent Magnet Synchronous Motors (PMSM):** High efficiency and power density with compact and lightweight design.
- **Switched Reluctance Motors (SRM):** Simple construction and cost-effective, but requires advanced control strategies.
- **Brushless DC Motors (BLDC):** Similar to the PMSM but with simpler control and limited torque ripple performance compared to PMSM.

Effective traction applications in electric vehicles require high torque and power density, especially at low speeds for smooth starts and uphill climbs, while maintaining high efficiency across a wide range of speed and torque. Accordingly, PMSMs dominate EV applications due to their efficiency, compact design, high torque output, and smooth performance [65]. While cost and magnet dependency pose challenges, advancements in motor design and control strategies continue to make PMSMs a cornerstone of modern electric vehicle powertrains.

PMSMs can be mainly categorized into surface-mounted PMSMs (SPMSMs) and interior PMSMs (IPMSMs). This study is entirely focused on the IPMSM, a specific type of motor in which the rotor contains embedded permanent magnets, enhancing torque density due to increased saliency [66]. The permanent magnets (PMs) are arranged to direct magnetic flux from the north pole to the south pole, passing through the stator. To induce rotor motion, a rotating magnetic flux is created in the stator using a three-phase AC current source. The interaction between the magnetic fields of the stator and the rotor causes the rotor to align with the stator's magnetic field. As a result, the rotor's rotational speed matches the magnetic field's speed in the stator.

2.3.1 Equivalent circuit model

The mathematical model of a PMSM is used to analyze its electrical behavior in the dq -reference-frame. A dq -reference-frame is a rotating coordinate system commonly used for analyzing AC machines and power electronics. It transforms three-phase (abc) variables into two orthogonal axes, d (direct) and q (quadrature). By rotating at the same speed as the rotor's magnetic field (in machines), the dq -frame converts time-varying signals into time-invariant DC-like quantities. This simplifies the control and analysis of AC systems, enabling techniques such as field-oriented control (FOC) or vector control in electric drives.

The mathematical model of a PMSM can be presented with the circuit equivalent model shown in Figure 2.4. In the model, R_s is the stator winding resistance, L_d is the inductance in the direct axis (aligned with the rotor magnetic field), and L_q is the inductance in the quadrature axis in dq -frame. ψ_m is the magnetic flux linkage due to the permanent magnets embedded in the rotor. i_d and i_q are direct and quadrature axis currents, and u_d and u_q are direct and quadrature axis voltages, and ω_r is the electrical speed of the rotor [67].

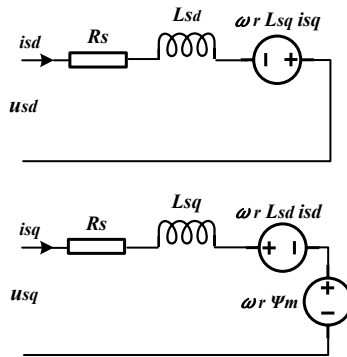


Figure 2.4: Equivalent circuit model of a PMSM in the dq -reference frame.

According to the model, the stator voltage and stator current relationship

can be described as

$$u_{sd} = R_s i_{sd} + L_{sd} \frac{di_{sd}}{dt} - \omega_r \psi_q \quad (2.18)$$

$$u_{sq} = R_s i_{sq} + L_{sd} \frac{di_{sq}}{dt} + \omega_r \psi_d \quad (2.19)$$

where ψ_d and ψ_q are stator flux linkage in dq -frame as function of inductance and current can be expressed as

$$\psi_d = L_{sd} i_{sd} + \psi_m \quad (2.20)$$

$$\psi_q = L_{sq} i_{sq} \quad (2.21)$$

The output electromagnetic torque[67], [68] can be expressed as

$$T_e = \frac{3n_p}{2} (\psi_m i_{sq} + (L_{sd} - L_{sq}) i_{sd} i_{sq}) \quad (2.22)$$

where n_p is the pole pair number of the machine.

From the perspective of mechanical dynamics, the rotor's mechanical speed Ω_r is governed by the following differential equation.

$$\frac{d\Omega_r}{dt} = \frac{1}{J} \left(T_e - T_L - \frac{B}{n_p} \omega_r \right) \quad (2.23)$$

where T_L denotes the load torque applied to the shaft, B represents the viscous damping constant, characterizing the slope of the speed-dependent load torque, and J is the rotational inertia of the shaft.

The relationship between the electrical and mechanical speed of the rotor can be expressed as

$$\omega_r = n_p \Omega_r \quad (2.24)$$

The electromagnetic power generated by the electric machine at the shaft is given by

$$P_e = T_e \Omega_r = T_e \frac{\omega_r}{n_p} \quad (2.25)$$

The fundamental frequency of the electric machine is calculated as

$$f_{el} = \frac{n_s n_p}{60} \quad (2.26)$$

where n_s represents the mechanical synchronous speed of the stator field, which is same as the mechanical speed of rotor n_r , can be expressed as

$$n_r = \frac{30}{\pi} \Omega_r \quad (2.27)$$

2.3.2 Control strategy

Field-oriented control (FOC) is a general control strategy used for controlling PMSMs (and other AC motors) to achieve precise control of torque and speed. It uses a dq -axis transformation to control the motor's torque-producing current and flux-producing current independently. This was achieved by decoupling the d and q axes through the feed-forwarding of the coupling terms. The d -axis current i_d is used to control the flux, while the q -axis current i_q is responsible for torque production. To improve performance, features like anti-windup and active damping are incorporated. Feedback controls in FOC for PMSM typically involves proportional-integral (PI) controllers to manage the dynamic response of the machine by adjusting the d -axis and q -axis currents. These controllers help eliminate the steady-state errors, maintain the machine's speed and torque by continuously adjusting the control inputs based on feedback from sensors [69]–[71].

By rewriting the equations (2.18) and (2.19), using the back-emf and coupling term $\omega_r L_s i_s$, the expression for the stator currents can be determined as

$$L_{sd} \frac{di_{sd}}{dt} = u_{sd} - R_s i_{sd} + \omega_r L_{sq} i_{sq} \quad (2.28)$$

$$L_{sq} \frac{di_{sq}}{dt} = u_{sq} - R_s i_{sq} - \omega_r L_{sd} i_{sd} - \omega_r \psi_m \quad (2.29)$$

By applying the Laplace transform, (2.28) and (2.29) can be rewritten as

$$i_{sd} = \frac{1}{L_{sd}s + R_s}(u_{sd} + \omega_r L_{sq} i_{sq}) \quad (2.30)$$

$$i_{sq} = \frac{1}{L_{sq}s + R_s}(u_{sq} - \omega_r L_{sd} i_{sd} - \omega_r \psi_m) \quad (2.31)$$

The following transfer function can be obtained as

$$G_{cd}(s) = \frac{1}{L_{sd}s + R_s} \quad (2.32)$$

$$G_{cq}(s) = \frac{1}{L_{sq}s + R_s} \quad (2.33)$$

The closed-loop system for the current controller is defined as a low-pass filter with a bandwidth α_c , where the system is characterized as

$$G_{ce}(s) = \frac{i_s}{i_{ref}} = \frac{F_c(s)G_c(s)}{1 + F_c(s)G_c(s)} = \frac{\alpha_c}{s + \alpha_c} \quad (2.34)$$

where i_s is the output current, i_{ref} is the reference current, and the error e between them can be act as the input of the current controller $F_c(s)$.

The controller $F_c(s)$ can be modeled as

$$F_c(s) = k_p + \frac{k_i}{s} \quad (2.35)$$

Similar to (2.34), the transfer function $F_c(s)$ can be rewritten as

$$F_c(s) = \frac{\alpha_c}{s} G_c^{-1}(s) = \frac{\alpha_c}{s} (L_s s + R_s) \quad (2.36)$$

The complete closed-loop control system is illustrated in Figure 2.5.

2.3.2.1 Current vector control strategy

The electromagnetic torque equation in (2.22) demonstrates that torque depends on both i_d and i_q . Therefore, different combinations of these two currents can produce the same torque. Maximum torque per ampere (MTPA) is a specific optimization strategy used within FOC (or other motor control strategies) to achieve the maximum torque for a given current level. This strategy aims to find the ideal balance between the d -axis current i_d and q -axis current

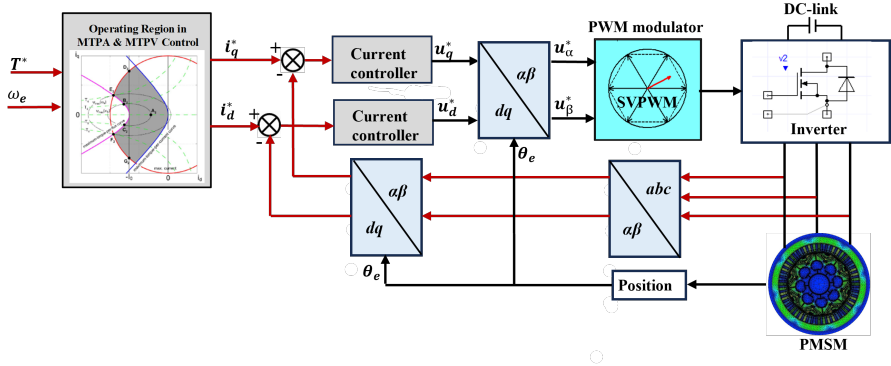


Figure 2.5: PMSM closed-loop control system.

i_q to minimize the current required for generating a specific amount of torque, thus reducing winding losses [72]. Hence, it is a technique that optimizes the machine's efficiency, particularly in the low-speed region where efficiency is critical.

In a PMSM, the operating limit consists of the operating points that provide the maximum available torque at each speed, within the chosen voltage and current limits. Therefore, up to three operation modes I, II, and III can be introduced. In mode I, called MTPA, the PMSM can produce the maximum torque without reaching the maximum voltage, as shown by the blue curve (trajectory B-A-G) in the dq -current plane in Figure 2.6. This holds for rotor speeds below the rated (base) speed (i.e. the speed at which the voltage limit is reached at peak torque operation; ω_1 in the figure). In modes II (B-C & G-F) and III (C-D & F-E), which are field weakening (FW) modes (for the speeds above rated speed, $\omega > \omega_1$), the dq -currents are again adjusted to maximize torque but now actions must be taken to not exceed the voltage limit. Although Mode II maximizes both current and voltage, further increases in speed may lead to Mode III, where the voltage stays at its maximum, and the current will be below its peak value. Notable is that for some PMSM drives (infinite speed drives), no Mode III exists [73]. The feasible operation area of the PMSM is shaded gray in the figure.

As illustrated in Figure 2.6, the torque levels are shown with the dashed green hyperbola, and the current limit is represented as a circular boundary in

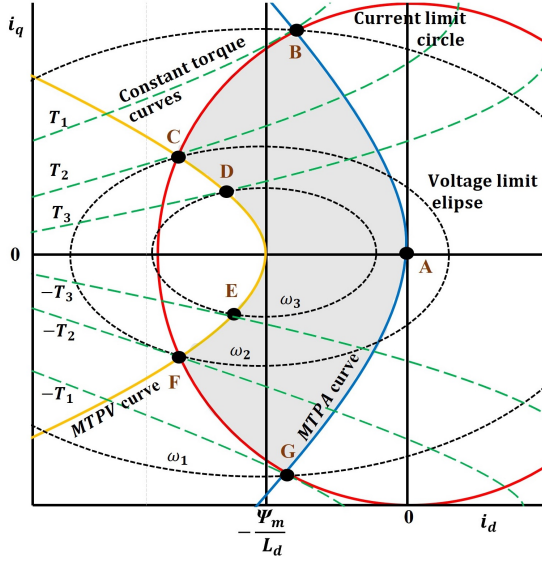


Figure 2.6: Operation boundary of a PMSM.

red. The voltage limit is represented by an elliptical shape, which shrinks as the rotor's operating speed increases (i.e. the ellipse reduces to its midpoint of $-\Psi_m/L_d$ as the speed increases).

The above-mentioned operation can not be achieved utilizing algebraic equations solely since the machine parameters vary with saturation. Instead, a numerical approach must be used, solving the minimization problem outlined below [74].

$$\begin{aligned}
 & \text{minimize} && f_0(i_{sd}, i_{sq}) \\
 & \text{inequality constraint} && f_i(i_{sd}, i_{sq}) \leq 0 \\
 & && h_i(i_{sd}, i_{sq}) = 0
 \end{aligned} \tag{2.37}$$

where

$$\begin{aligned}
 f_0(i_{sd}, i_{sq}) &= \sqrt{i_{sd}^2 + i_{sq}^2} \\
 f_i(i_{sd}, i_{sq}) &= \sqrt{u_{sd}(i_{sd}, i_{sq})^2 + u_{sq}(i_{sd}, i_{sq})^2} - \frac{V_{dc}}{\sqrt{3}} \\
 h(i_{sd}, i_{sq}) &= 1.5npi_{sq} [\Psi_m(i_{sd}, i_{sq}) + (L_{sd}(i_{sd}, i_{sq}) - L_{sq}(i_{sd}, i_{sq})) i_{sd}] - T_{e,\text{ref}}
 \end{aligned} \tag{2.38}$$

where $u_{sd}(i_{sd}, i_{sq})$ and $u_{sq}(i_{sd}, i_{sq})$ were calculated using the stator equations in steady state, defined in (2.18) and (2.19). The objective function, f_0 , represents the RMS phase current. The inequality constraint, $f_i(i_{sd}, i_{sq})$, serves as a voltage limitation when field weakening is required. Finally, the equality constraint, $h(i_{sd}, i_{sq})$, defines the electromagnetic torque, as presented in (2.22). Note that, the variations in L_{sd} , L_{sq} are functions of both i_{sd} and i_{sq} .

2.3.3 Power loss analysis

The energy efficiency of a PMSM is primarily affected by power losses, including copper losses in the windings, losses in the permanent magnets (PM), and iron losses in both the stator and the rotor. The breakdown is summarized below.

2.3.3.1 Copper losses

Copper losses in a PMSM occur due to resistance in the stator windings, which generates heat as current flows through the copper [75]. These losses are proportional to the square of the current, and are most significant at higher loads and speeds, and can be calculated as

$$P_{cu} = \frac{3}{2}(i_{sd}^2 + i_{sq}^2)R_s = \frac{3}{2}i_s^2R_s \tag{2.39}$$

where i_s is the amplitude of the stator phase current.

2.3.3.2 Iron losses

Iron losses in PMSMs are significant contributors to overall power loss and can be divided into two main components: hysteresis losses and eddy current losses. Bertotti's theory [76] provides a comprehensive model for estimating

these losses and introduces an additional loss term to take into account excess losses that are not captured by hysteresis or eddy current models. Hysteresis losses occur because of the continuous reversal of the magnetic field in the iron core. The energy required to magnetize and demagnetize the core material causes these losses. Eddy current losses are induced by the changing magnetic field, which generates circulating currents (eddy currents) in the conductive core material. The excess (stray) losses arise from factors like mechanical vibrations, flux leakage, and other non-idealities in the system. According to Bertotti, these losses depend on the frequency of flux variations and the maximum flux density. The total iron loss in PMSMs can be expressed as

$$P_{fe} = P_{fe,h} + P_{fe,c} + P_{fe,e} \quad (2.40)$$

The modified Steinmetz equations are employed to describe $P_{fe,h}$, $P_{fe,c}$ and $P_{fe,e}$, which can be expressed as follows [77].

$$P_{fe,h} = k_h f B_m^2 \quad (2.41)$$

$$P_{fe,c} = k_c f^2 B_m^2 \quad (2.42)$$

$$P_{fe,e} = k_e f^{1.5} B_m^{1.5} \quad (2.43)$$

where f and B_m represent the frequency and the amplitude of magnetic flux density of the machine, and k_h , k_c and k_e are coefficients of hysteresis loss, eddy current and excess losses, respectively.

It is important to note that accurate loss prediction during the design phase of electric machines is critical for achieving the desired efficiency and performance. However, as noted in [78], the core loss estimations from analytical models often show discrepancies of up to 100% when compared to experimental measurements of electric machines (EMs). Although these discrepancies have been studied for decades, no universally applicable solution has emerged due to the complexity of the problem.

2.3.3.3 Magnet losses

Magnet losses in PMSMs refer to the losses that occur in the permanent magnets (PMs) due to the alternating magnetic field within the motor. These losses primarily result from eddy currents induced in the magnets and hysteresis losses due to the reversal of magnetization. In practical motor design, hysteresis losses in PMs, particularly with high-performance magnets (such as NdFeB and SmCo) that have low coercivity, are often negligible compared to eddy current losses. These materials don't require much energy to magnetize and demagnetize. This leads to very low hysteresis losses [79]. Typically, the focus is on minimizing eddy current losses, which become more pronounced with the introduction of time and space harmonics in the stator current [80]. Furthermore, at higher operating frequencies and flux densities (at high speeds or under heavy load conditions), the eddy current losses in the PMs can lead to localized heating in the magnets, which can affect the magnet's performance, reduce efficiency, and even cause demagnetization if the temperature rises too much [81].

The eddy current losses in PMs can be obtained as described in [82],

$$P_{mag,e} = \frac{1}{\sigma} \int J_e \cdot J_e^* dV \quad (2.44)$$

where σ and V represent the conductivity and volume of PM material, respectively. J_e is the eddy current density in PMs and J_e^* is the complex conjugate of J_e .

2.4 Energy loss analysis over drive cycle

Drive cycles are predefined sequences of speed versus time that simulate typical driving conditions. They are integral tools for assessing the efficiency of EVs, as they simulate real-world driving conditions and provide valuable insights into energy consumption, range, and battery performance. These cycles simulate various driving behaviors, including acceleration, deceleration, and cruising, to assess how efficiently an EV uses the available energy during its operation. Different drive cycles are used to model different driving environments, such as city traffic, highway driving, and combined urban-rural conditions. A specific drive cycle, combined with the vehicle parameters used,

can be employed to determine the operating conditions for various components in the vehicle's drive system.

The vehicle dynamics and the forces acting on the vehicle can typically be described according to [83], as

$$F_{wheel} = \frac{\rho_a}{2} C_d A_f v^2 + C_r m g \cos \alpha + m g \sin \alpha + m \frac{dv}{dt} \quad (2.45)$$

where ρ_a represents the air density, C_d is the aerodynamic drag coefficient. m is the vehicle mass, g is the gravitational constant, α is the road inclination angle, C_r is the dimensionless rolling resistance coefficient. The parameter A_f is the effective cross sectional area.

The power required by the wheels to sustain a certain speed is then obtained by

$$P_{wheel} = F_{wheel}(t) v_{car}(t) \quad (2.46)$$

The total accumulated energy consumed at the wheels is determined as,

$$E_{wheel}(t) = \int P_{wheel}(t) dt \quad (2.47)$$

2.5 Optimal system-level strategies

As this study primarily focused on an optimized system-level loss analysis, it addressed strategies aimed at enhancing the overall performance of the powertrain system, as summarized below.

2.5.1 Optimum switching frequency over drive regions

The switching frequency of an inverter refers to how often the inverter switches the power devices (e.g., MOSFETs or IGBTs) on and off. Increasing the switching frequency reduces the harmonic content in the motor's three-phase current waveforms, leading to lower motor losses by reducing current ripples. However, increasing the switching frequency leads to a proportional increase in inverter losses. Hence, determining an optimal switching frequency for a motor drive system leads to achieving overall minimal system losses.

The optimal switching frequency can be adjusted across the driving range (low, medium, and high-speed operation) based on motor speed, load conditions, and thermal considerations to ensure that the motor operates efficiently

across its entire operating range. At low speeds, a lower switching frequency might be used to reduce switching losses, while at high speeds, a higher switching frequency can be used to reduce current ripple, which in turn lowers the motor's losses.

The switching frequency also affects the thermal performance of the system, since higher frequencies can produce more heat in the power electronics. Therefore, an optimal frequency should be selected to balance losses and thermal constraints.

2.5.2 Optimum DC-link voltage over drive regions

Optimum DC-link voltage involves adjusting the voltage supplied to the inverter in an efficient way to minimize losses, and ensure that the motor operates optimally across varying drive conditions. One way to realize this is by incorporating an additional DC-DC converter and implementing power management methods to optimize powertrain efficiency. Figure 2.7 illustrates both configurations, with and without the inclusion of a DC-DC converter in the powertrain, both featuring IGBT switches.

At lower operating speeds, the required DC-link voltage is reduced compared to the levels needed at rated or high-speed operation. This is primarily due to the dependence of the back electromotive force (EMF) on motor speed. A reduced DC-link voltage results in decreased switching losses within the inverter, thereby enhancing the overall efficiency of the drive system. In contrast, during rated or high-speed operation, including the field-weakening region, an increased DC-link voltage allows for a higher phase voltage. This adjustment can lower the motor current, effectively reducing both the inverter's conduction losses and the winding losses in the machine.

However, integrating a DC-DC converter into the powertrain system introduces additional passive components, increases system complexity, raises costs, and reduces reliability, as noted in the literature [34], [35], [84]. Furthermore, the losses associated with the DC-DC converter, including switches and inductance losses should be taken into account.

2.5.2.1 DC-DC Boost converter

A boost converter steps up a DC input voltage to a higher output voltage using inductors, capacitors, and a fast-switching transistor (e.g., a MOSFET

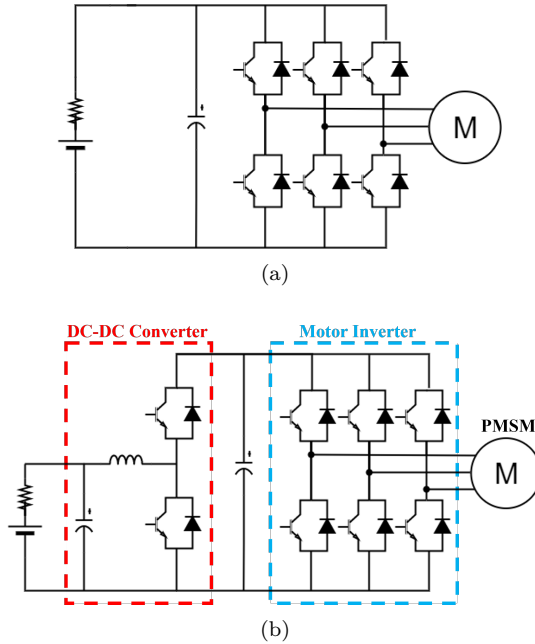


Figure 2.7: Voltage source inverter configuration. (a) Conventional EV powertrain. (b) Powertrain incorporating a synchronous DC-DC boost converter.

or IGBT). When the transistor switches on, energy is stored in the inductor; when it switches off, that stored energy is released to the output, boosting the voltage.

A synchronous boost converter, highlighted in dashed red in Figure 2.7 (b), replaces the diode with another active switch (MOSFET or IGBT), thereby reducing conduction losses and enhancing overall efficiency—especially in high-power applications. Lower losses also mean less heat generation, making these converters well-suited for electric vehicles, telecom power supplies, solar power systems, and battery charging systems.

- **MOSFETs/IGBTs conduction and switching losses:**

Assuming the current flowing through the DC-DC converter remains at a constant amplitude during a single pulse period, with fluctuations smoothed by the inductance, the duty cycle D of the boost converter

can be calculated as

$$D = 1 - \frac{V_{\text{batt}}}{V_{\text{dc}}} \quad (2.48)$$

where V_{batt} is the battery terminal voltage and V_{dc} is the DC-link voltage.

The average conduction losses of the MOSFETs and IGBT switches, along with the switching losses, can be determined using methods similar to those outlined in Section 2.2.2.

- **Inductance core and copper losses:**

As previously mentioned, to approximate the losses introduced by the DC-DC converter, including semiconductor power losses, an inductor must be utilized, and its corresponding core and copper losses should be evaluated. The choice of the selected inductor core material and shape depends on the application's requirements, such as frequency, power handling, size, efficiency, and cost. Ferrite and amorphous steel are often preferred for high-frequency applications, while silicon steel and powdered iron are better suited for low-frequency, high-power applications. The core shape also influences efficiency. Toroidal cores, for instance, typically offer higher efficiency and reduced electromagnetic interference (EMI), though they can be more expensive [85].

To begin with, the required inductor value in a boost converter can be calculated based on the peak required DC current in the converter and a peak-to-peak current ripple (can be an approximation of 20 % of the DC current),

$$L = \frac{V_{\text{in}}DT}{2\Delta I_{\text{L,peak}}} \quad (2.49)$$

where V_{in} is the battery terminal voltage, D is the duty cycle of the boost converter, T is the period time and $\Delta I_{\text{L,peak}}$ is the peak inductor ripple current.

For a chosen Toroid powder core using the inductance factor $A_L (nH/T^2)$ from the core data sheet and the required number of core stacks, the

approximate number of turns can be calculated as,

$$N = \sqrt{\frac{L}{A_L}} \quad (2.50)$$

To meet the required inductance value, the number of turns can be adjusted by calculating the magnetizing field H Oersteds (Oe), considering the initial permeability at the calculated H bias level [86], and iterating the calculations if necessary. The magnetizing field H is determined as

$$H = \frac{4\pi NI}{l_e} \quad (2.51)$$

where I is the DC current and l_e is the magnetic path length.

Core loss arises from changes in the magnetic flux field within a material. The core loss density, P_L (mW/cm^3), is generally a function of the peak AC flux swing, B_{peak} in *Tesla* (T), and the operating switching frequency. This loss can typically be approximated using manufacturer-provided core loss charts or by applying the Steinmetz loss equation [87], which provides a curve-fit model for estimating losses under given flux and frequency conditions,

$$P_L = kB_{\text{peak}}^\alpha f^\beta \quad (2.52)$$

$$B_{\text{peak}} = \frac{\Delta B}{2} \quad (2.53)$$

where k , α and β can be determined from curve fitting.

Worth mentioning is that, since flux density B is a nonlinear function of magnetic field (H), B_{peak} can be calculated by first finding the maximum and minimum values of H . By evaluating H at these extremes, the corresponding B values can then be determined, allowing for an accurate calculation of B_{peak} . Accordingly, considering the number of stacks in the core volume, core loss is determined as,

$$P_{\text{fe}} = P_L l_e A_e = P_L V_e \quad (2.54)$$

where A_e and V_e are the effective cross-sectional area and volume of the

core, respectively, both of which are provided in the core's datasheet.

Finally, the DC copper loss of the inductor or wire loss can be obtained directly as,

$$P_{cu} = Resistance.I^2 \quad (2.55)$$

where *Resistance* is the product of the data-sheet parameters: the mean length of turn, the number of turns, and the resistance per unit length for the selected wire diameter.

2.5.3 Graphene: high thermal conductivity material

Optimizing thermal conditioning systems involves effective heat transfer strategies, with recent efforts focusing on novel heat-spreading materials. Materials with ultra-high thermal conductivity, like graphene, can notably reduce operating temperatures and decrease stress on switching devices [88], [89]. Graphene, with its in-plane thermal conductivity of up to 5300 W/m.K at room temperature [90], surpasses copper (402 W/m.K) and aluminum (237 W/m.K) [91], [92], while offering lightweight properties (2.2 g/cm³) [25], [88], [91]. Graphene in the form of graphene-assembled films (GFs) has drawn attention for their promising heat dissipation performance [25], [91].

Moreover, materials like graphene enable more compact designs for electronic components. Composed of few atomic layers of sp² bonded carbon, graphene exhibits efficient phonon transfer, resulting in outstanding thermal conductivity [91]. However, single-layer graphene falls short in practical applications due to issues like poor quality, non-freestanding structures, and limited heat flux capacity [91]. To address these limitations, graphene films fabricated from individual sheets exhibit better thermal and mechanical properties [91], [93], [94], although challenges like grain size, alignment, and phonon interfacial scattering still limit performance [95]–[97].

To improve the performance of graphene films, a dry-bubbling approach, utilizing high-temperature graphitization and mechanical pressing, has been proposed [91]. Additionally, molecular functionalization is used to minimize thermal contact resistance between graphene and substrates [98]. Despite these advancements, the fabrication process remains challenging and not fully detailed.

Therefore, using graphene films in power electronics, such as in packaging,

remains challenging, especially when it comes to shaping them in standard electronics labs.

CHAPTER 3

Case studies

This chapter describes the simulation models and experimental setup along with the technical specifications used to analyze and validate the findings of this thesis. The main focus is on the efficiency analysis of the electric powertrain system configured in this work, which includes an IPM electric machine, a three-phase VSI, the control techniques, as well as diverse thermal simulations, and finally, power loss analyses for the entire drive system. The detailed methodology for each part of the study and the corresponding results will be presented and discussed in the respective chapters.

3.1 Simulation setups

This study employed various simulation tools, with the primary ones being MATLAB scripts and Simulink models, PLECS, Ansys Maxwell, and Ansys Twin Builder. These tools were primarily used for power and energy loss modeling, FEM-based loss analysis, thermal network modeling, and lifetime studies. For detailed thermal simulations, including conjugate heat transfer (CHT) and computational fluid dynamics (CFD) analyses, the Helyx software (an OpenFOAM fork) [99] and COMSOL Multiphysics were utilized in two

separate studies.

3.1.1 Case setup 1

This case study was initially based on PMSM data analyzed by FEM provided by the machine supplier. However, modifications were made, including the implementation of maximum torque per ampere (MTPA) and maximum torque per volt (MTPV) control strategies discussed in Subsection 2.3.2.1. These modifications were carried out using MATLAB scripts to regenerate the necessary reference operating data, specifically tailored for the study's objectives.

A three-phase voltage source inverter, controlled by SPWM with the zero-sequence addition method as discussed in Subsection 2.2.1, was numerically implemented in MATLAB using the analytical power loss modeling method discussed in 2.2.2. The inverter features two different SiC half-bridge modules: a 3rd generation CAB450M12XM3 SiC module [100] and a 2nd generation CAS300M12BM2 SiC module [101], both in the 1200 V class, as well as a 1200 V Si IGBT module, FZ600R12KE3 [102], for comparisons in various analyses. In the SiC-based inverters, three SiC half-bridge modules, each with two MOSFETs in parallel for each switch position, were used. For the IGBT-based inverter, six IGBT modules (with free-wheeling diodes), one IGBT in each switch position, were employed to meet the respective design specifications in each analysis. All sets were normalized to a nominal current of 600 A for comparison purposes. The rating parameters and technical data for the PMSM, and the inverters used in this case study are provided in Table 3.1.

Table 3.1: Drive system parameters used in Case setup 1

Parameter	Quantity	Unit
Number of pole pairs	4	-
Peak phase current	400	A-RMS
Peak power	80	kW
Peak torque	160	Nm
Maximum speed	12000	rpm
DC-link voltage	300	V
Permanent magnet flux linkage	$0.0241 \ll \psi_m \ll 0.0435$	Wb
d -axis inductance	$0.0842 \ll L_d \ll 0.182$	mH
q -axis inductance	$0.114 \ll L_q \ll 0.462$	mH
Switching frequency	10	kHz
Blanking time	0.5	μ s

It is worth noting that the aforementioned PMSM and inverter were numerically integrated to create a setup model for calculating power and energy losses as well as the impact of thermal feedback on the losses in the traction SiC-based inverters compared to the Si-IGBT-based inverter. Furthermore, using this setup, lifetime studies for the SiC and Si-IGBT switches were conducted, with the prediction model discussed in Subsection 2.2.3. The respective used methods and the findings from these analyses are presented in chapters 4 and 5.

Since parameters in power modules, such as on-state resistances, forward voltage drops, as well as switching and reverse recovery energies exhibit temperature dependence, inverter power losses were determined using the thermal lumped parameter configuration of the power modules shown in Figure 3.1 and the corresponding equations as follows. T_j represents the junction temperatures of the MOSFETs, and diodes, T_c is the case/baseplate temperature, T_s and T_f represent the heatsink and fluid temperatures, respectively. For a fair comparison, the same heatsink was used for each inverter although it would have been possible to use a smaller one for the SiC MOSFET inverters. The fluid temperature and fluid flow-rate were set to 65°C and 10 l/min, respectively. (Note that the detailed thermal calculation methods will be discussed in the respective chapters.) The thermal resistances from the junction to case, case to sink, and sink to fluid, represented by $R_{th,jc}$, $R_{th,cs}$, and $R_{th,sf}$,

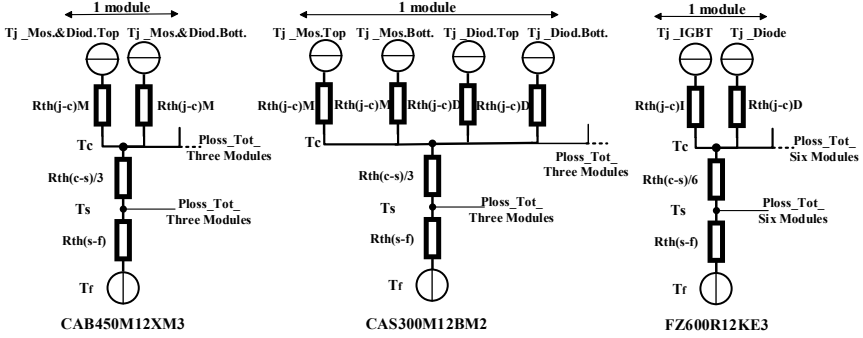


Figure 3.1: Thermal lumped parameter configuration for the investigated power modules in steady-state.

respectively, can be expressed by,

$$R_{th,jc} = \frac{T_j - T_c}{P_{loss}} \quad (3.1)$$

$$R_{th,cs} = \frac{T_c - T_s}{P_{loss}} \quad (3.2)$$

$$R_{th,sf} = \frac{T_s - T_f}{P_{loss}} \quad (3.3)$$

where T_j to T_f signifies the temperature values from the junction to fluid. The junction temperature can be modeled as

$$T_j = T_f + (R_{th,jc} + R_{th,cs} + R_{th,sf})P_{loss} \quad (3.4)$$

where P_{loss} represents the associated losses of the module's devices in each thermal stack-up layer, as illustrated in Figure 3.1.

3.1.2 Case setup 2

The objective of this case setup is to determine the optimal DC-link voltage across the entire range of the drive operating conditions by integrating a DC-DC converter into the powertrain. To achieve this target, a 2-D FEM model

of an IPMSM, built in Maxwell, was used. An illustration is shown in Figure 3.2.

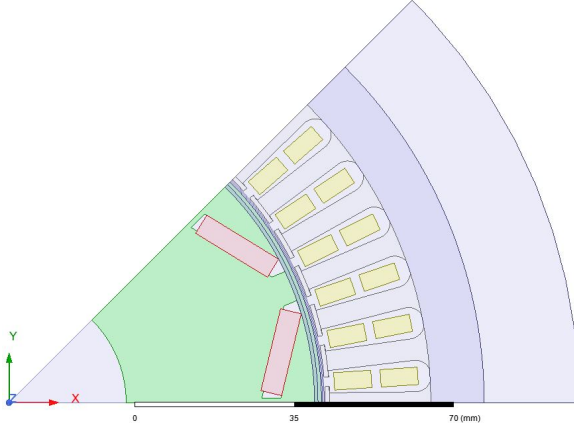


Figure 3.2: The 2D IPMSM model in ANSYS Maxwell.

The machine's stator was modeled with 48 slots, and to enhance computational efficiency, the model size was reduced to 1/8 of the original, leveraging a symmetry of the 8 identical poles. The FEM analysis was conducted by applying current excitation to the coils along with a set of boundary conditions. A transient analysis was then set up to run the simulations under different operating conditions. Next, using the d - and q -axis reference currents derived from the FEM analysis, the MTPA and MTPV control strategies were implemented through a co-simulation framework between Ansys Electronic Desktop and MATLAB for mapping the key operating points within the machine's torque-speed region.

A three-phase VSI was numerically implemented similar to the one in Case Setup 1, and then connected to a DC-DC boost converter for the purpose of this case study, as shown in the circuit configuration in Figure 2.7 (b) from the previous chapter. The converter-inverter circuit incorporates power modules similar to those in Case Setup 1, including a half-bridge SiC module, CAB450M12XM3 [100], and a Si IGBT module, FZ600R12KE3 [102] for the comparisons. In the SiC-based converter-inverter, four SiC half-bridge modules (one for the converter and three for the inverter) were used, with one MOSFET for each switch position. For the IGBT-based inverter, six IGBT

modules, one in each switch position, and two modules for the converter, were employed to meet the respective design specifications in each analysis. The rating parameters for the drive system used in this case study are provided in Table 3.2.

Table 3.2: Drive system parameters used in Case setup 2

Parameter	Quantity	Unit
Number of slots	48	-
Number of pole pairs	4	-
Peak power	100	kW
Peak phase current	400	A-RMS
Peak torque	333.3	Nm
Maximum speed	11000	rpm
DC-link voltage	220-450	V
Permanent magnet flux linkage	$0.08 \ll \psi_m \ll 0.1298$	Wb
d -axis inductance	$0.269 \ll L_d \ll 0.543$	mH
q -axis inductance	$0.417 \ll L_q \ll 1.5$	mH
Switching frequency	10	kHz
Blanking time	0.5	μ s

Worth mentioning is that a Toroid powder core with XFlux material from MAGNETICS, model 0078163A7 [103], was selected as the most efficient choice for the inductor of the DC-DC converter in the current design. The theory and the design steps are already presented in Chapter 2. Table 3.3 gives the required inductor design values and selected core parameters.

Notably, the thermal model configurations for the power modules are similar to those previously shown in Case setup 1, Figure 3.1, except that the sets were normalized to the nominal current of the SiC module of 450 A for a fair comparison.

Subsequently, the mapped operating points derived from the above-mentioned co-simulation were then utilized in the inverter as well as the converter-inverter loss calculation model. The calculations cover a range of DC voltages from 220 V to 450 V, representing the lower and upper boundaries of the DC-link voltage. The implications of these variable voltages alongside the evaluation

Table 3.3: Selected inductance core parameters.

Parameter	Value	Unit
Battery terminal voltage	300	Vdc
DC-link voltage	450	Vdc
Peak DC current	290	A
Switching frequency	10	kHz
Inductance value	115	μ H
Number of stacked cores	2	—
Number of wire strands	5	—
Wire size	6	AWG
Number of turns	51	—

of the potential benefits of integrating a DC-DC converter into the EV powertrain are discussed and detailed in Chapter 7.

3.1.3 Case setup 3

Similar to the two previous setups, the drive system in this case study consists of an IPMSM and a three-phase propulsion VSI. The studied machine features 48 stator slots and 8 rotor poles with double-layer V-shaped magnets. The geometry of the machine is depicted in Figure 3.3 and the key properties are given in Table 3.4.

The focus of this case setup is on identifying the optimal switching frequency for SiC-based motor drives across a wide range of operating conditions and comparing the results with those of a Si-IGBT counterpart. To achieve this, the baseline electric drive system was configured within a real-time co-simulation between Twin Builder and Ansys Maxwell with variable time steps less than 100 ns to comprehensively capture their interaction with varying PWM switching frequencies and predict the corresponding current ripple characteristics. The analysis combines electromagnetic field simulations in Ansys Maxwell with the drive system control algorithm in Ansys Twin Builder using PWM voltages applied to the IPMSM, compared to conventional sinusoidal current excitation. Note that in a conventional way, to characterize an electric machine in FEM tools, a simulation is run with current excitation at a single speed value. Subsequently, these results are extrapolated for other speed ranges to determine the overall machine's performance characteristics

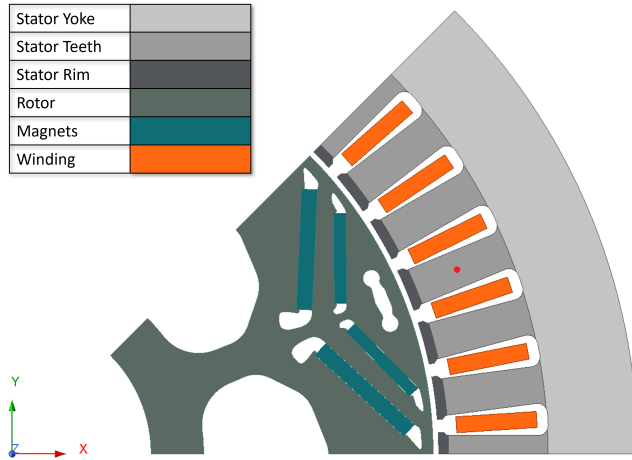


Figure 3.3: Permanent Magnet Synchronous Machine Geometry. Orange: Winding, Green: Magnets, Gray: Stator and rotor steel cores, Selected point in the tooth to do further analysis on flux density is marked with red

Table 3.4: Key parameters of the baseline electric Machine used in Case setup 3

Parameter	Quantity	Unit
Stator outer diameter	250	mm
Rotor outer diameter	168	mm
Air gap length	1.1	mm
Active Length	119	mm
Number of slots	48	-
Number of pole pairs	4	-
Peak power	220	kW
Peak current	250	A-RMS
Peak torque	426	Nm
DC-link voltage	800	V
Switching frequency	2.5-55	kHz
Blanking time	0.5	μ s

in the speed-torque map, similar to the approach used in Case setup 2.

In the inverter configuration, CAS300M17BM2 [104], a 1700 V class half-

bridge SiC module (three MOSFETs in parallel in each switch position) was used and compared with a Si-IGBT module, FZ600R17KE3 [105] (two IGBTs in parallel in each switch position) with the same blocking voltage of 1700 V for the analysis within the Twin Builder tools. To accurately determine the inverter losses, the measured currents and instantaneous voltages obtained from the real-time co-simulation between Twin Builder and Ansys Maxwell were imported into MATLAB for numerical loss model implementation.

The calculations covered a PWM switching frequency range of 2.5 kHz to 55 kHz. The effects of varying switching frequencies alongside the evaluation of the potential benefits of selecting an optimal switching frequency across the drive regions to minimize the current ripple and maintain efficient loss levels in the PMSM drive system are detailed in Chapter 8.

3.1.4 Case setup 4

This case study includes two simulation setups. The first setup analyzes the detailed thermal performance of the SiC power module, CAB450M12XM3 [100], using COMSOL Multiphysics. The second setup involves a full transient 3-D conjugate heat transfer (CHT) model of a pin-fin heatsink—with the power module mounted on top—using Helyx software (OpenFOAM).

The simulations began with the creation of the entire geometry using a computer-aided design (CAD) model.

Furthermore, the simulations mentioned above incorporate graphene, a novel, cost-effective, and eco-friendly thermal conductive material proposed in this thesis for use in SiC power module packaging and heatsink design. Graphene aims to enhance the heat distribution within the SiC module from the chip level down to the fluid, along with the water jacket geometries. The specific methods for incorporating graphene into the power module and heatsink design, along with the corresponding results, will be presented in Chapter 6.

3.1.4.1 3D-CAD model for thermal modeling set-up of the power module

To accurately model the heat distribution from the chips in the SiC devices to the fluid, a thermal model of the investigated power module was developed. The geometry was designed to closely match the real module, starting with CAD modeling. Although the thermal packaging aspects of the used

module, CAB450, were mostly unknown due to confidentiality, it was at least known that the base plate and insulator were made of copper and silicon nitride, respectively. Therefore, two experimental analyses were conducted. The first analysis involved scanning electron microscopy (SEM), and the second included energy-dispersive X-ray spectroscopy (EDS).

These analyses were performed on a similar voltage class SiC power module, CAS300M12BM2 [101], which served as a reference. The goal was to gather additional material information to construct a more realistic thermal model of the module. By conducting SEM/EDS analyses, structures with tiny thicknesses can be detected. In SEM, the sample is scanned using a highly energetic and focused electron beam, and then an extremely enlarged image of the morphology of the sample can be provided. EDS is a chemical micro-analysis technique, that identifies the X-rays released from the sample throughout a bombardment process with electrons so that the element arrangement of the analyzed volume can be determined [106]. It is worth noting that, the analysis has been conducted on a cross-sectional cut-off piece of the module.

As depicted in Figure 3.4 (a), the chips are all silicon-carbide, the base plate is made of copper and an aluminum nitride insulator has been used as one of the direct bonded copper (DBC) layers. The other two DBC layers are made of copper. Moreover, the SEM/EDS analysis revealed that the solder was $Sn_{90}Ag_{10}$ and it has been used for both solder layers, below the chip and below the DBC layers. The layers' respective thickness is presented in Figure 3.4 (b) and Table 3.5, along with the material thermal properties. It should be noted that silicon nitride (Si_3N_4) was used as the ceramic material in the DBC substrate.

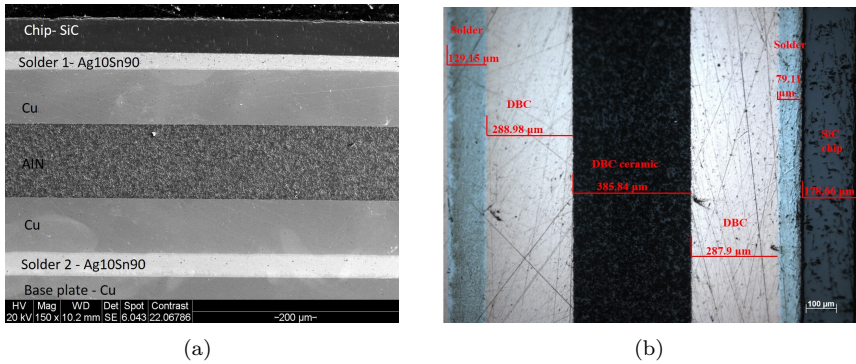


Figure 3.4: Materials and thickness of the reference SiC module CAS300 from SEM/ESD analysis. (a) Layer materials (b) Materials' thickness (given in Table. 3.5).

Table 3.5: Power module layers' thicknesses and thermal properties.

Layer	Material	Thickness	Thermal conductivity, K (W/m.K)	Density, ρ (kg/m ³)	Heat capacity, C (J/(kg.K))
Chip	SiC	178 μm	490	3216	690
DBC	Cu	288 μm	400	8940	385
DBC ceramic	Si_3N_4	386 μm	29	3100	700
Solder (below chip)	$\text{Sn}_{90}\text{Ag}_{10}$	79 μm	50	9000	150
Solder (below DBC)	$\text{Sn}_{90}\text{Ag}_{10}$	129 μm	50	9000	150
Baseplate	Cu	3 mm	400	8940	385

Figure 3.5 presents an illustration of a 3-D geometry of the power module. Each group of five chips represents one SiC switch placed in one half-bridge module. The dimensions of the module were implemented according to the datasheet of the CAB450 module.

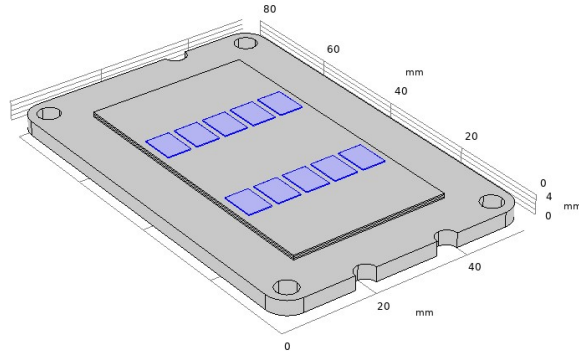


Figure 3.5: 3D-geometry of CAB450 SiC module.

3.1.4.2 3D-CAD model of the heatsink

To evaluate the thermal behavior of SiC power switches in contact with the coolant, mimicking real-world cooling, a pin-fin heatsink was designed for this setup. The key objective for a heatsink design is to enable a uniform heat dissipation while maintaining a low-pressure drop balanced with manufacturing, material, and packaging costs. Therefore, a liquid-based cooling with a significantly higher heat transfer coefficient and higher Nusselt number was considered a better candidate for a high heat flux SiC-based power module compared to those operating with forced air convection. To reduce the complexity of the CHT computations as well as to decrease the simulation time, the dimensions of the above-mentioned heatsink were modified to fit a single SiC power module. The coolant type was chosen as a 50/50 mixture of water and ethylene glycol with volume flows of 1 l/min and 6 l/min, illustrating a practical application in contrast to using pure water alone. Realistic thermophysics of the coolants is often overlooked and instead, pure water is used for modeling, which has more cooling ability than the industry-standard glycol mixtures. Figure 3.6 visualizes the drawing CAD geometry of the heatsink along with the location of the boundary conditions in a 2D view. The dimensions of the entire heatsink structure, as illustrated, are 85 mm \times 100 mm \times 25.5 mm in the x-y-z direction.

The increased surface area and the vortex shedding mechanisms have been reported to lead to better heat transfer using rectangular fins compared to

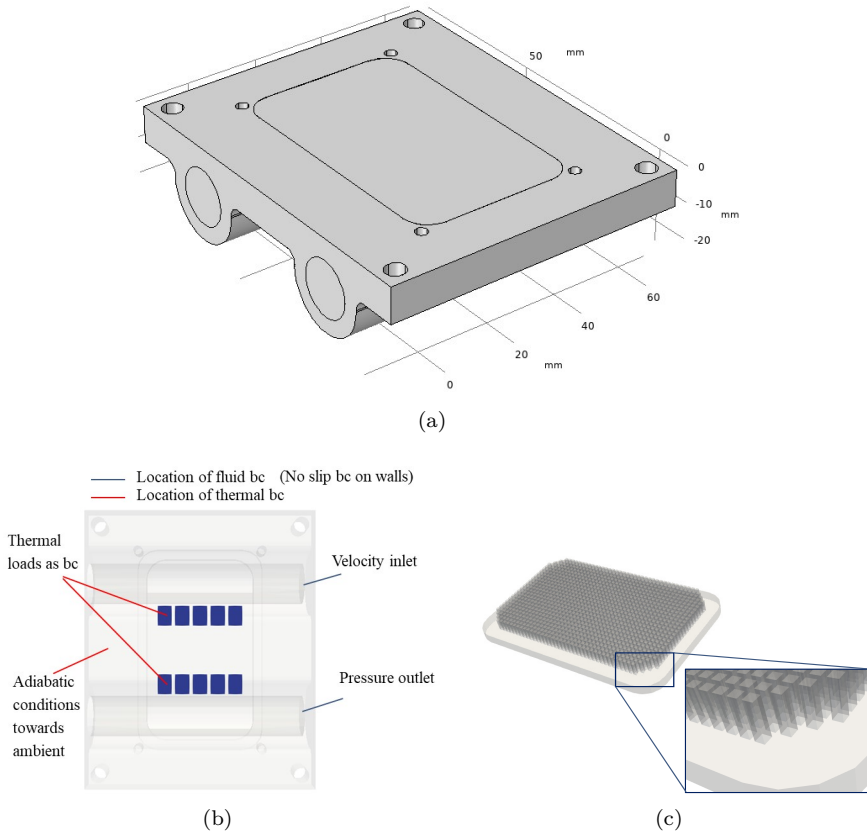


Figure 3.6: (a) Geometry of the heatsink, designed for one power module. (b) Locations of the boundary conditions. (c) Heat exchange unit.

cylindrical fins [107]. The rectangular design, not only increases the heat transfer surface but also as the coolant separation at the edges, adds additional mixing of the momentum and thermal boundary layers due to vortex shedding at the corners. Vortex shedding is the process where coherent structures formed during the energy cascade in the coolant fluid flow transition into turbulence, enhancing mixing. Incorporating this phenomenon is essential for accurate modeling. Conversely, circular pins or other shapes require special manufacturing processes [108], leading to higher computational costs

and increased complexity. Therefore, from the tuning of pin length, width, and distance, an improved heat exchange unit of the heatsink was designed to comprise 1075 rectangular-shaped fins of 1 mm section dimension and 4 mm height in the z-direction as depicted in Figure 3.6(c).

This test case provides insights into the prospective use of bundled 2D nanomaterials, particularly critical for EVs' cooling. The modeling procedure employed here could be extended to other power-intensive cooling applications.

3.1.4.3 Automated FEM computation in COMSOL for steady-state/transient heat dissipation

To be able to capture all the heat dissipation surface interactions, a 3D FEM simulation in COMSOL Multiphysics with a laminar flow interface was performed. Each of the power module materials and their thicknesses were accounted for in the meshing procedure as separate computational domains including the solders, copper, DBC, etc. To take the thermal coupling and heat spreading effects into consideration, the contact resistances between the solder layer and chips as well as between the solder and DBC layer were also modeled using the provided realistic values by material datasets (from SEM/EDS) and calculated as follows.

$$R_{th} = \frac{d}{A \cdot K} \quad (3.5)$$

where R_{th} is the thermal resistance of the layer in $[K/W]$, d is the layer thickness, A is the area of the layer and K is the thermal conductivity of the layer material.

Since the analysis focuses on the thermal distribution within the chips and DBC layers, a manually refined mesh is applied in these regions. In general, a uniform mesh distribution is created, as shown in Figure 3.7. The boundary conditions are defined by treating the chips as heat sources, with a selected power loss of 1262 W (i.e., 126.2 W per chip) applied to these heat sources, based on the previous power loss calculations of the investigated module discussed in Case study 1.

For the first part of this case study conducted in COMSOL, to simulate a liquid cooling solution, the bottom surface of the baseplate is assigned an approximated predetermined heat transfer coefficient (HTC) of $3000 (W/m^2.K)$, to represent the convective heat flux, with a water flow rate of 1 m/s and a

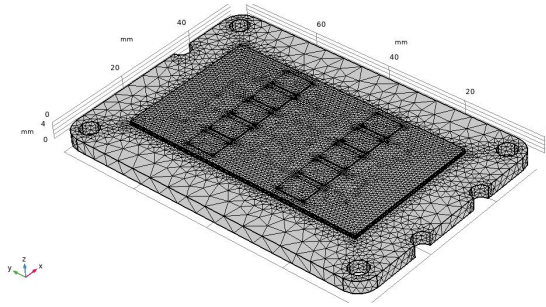


Figure 3.7: Mesh visualization of CAB450 SiC module.

temperature of 65°C . All other boundaries are set to a heat transfer coefficient of $10 \text{ (W/m}^2\cdot\text{K)}$, corresponding to the convection of low-speed air flowing above a surface [109].

In general, the transfer of heat is described as the movement of thermal energy due to a temperature gradient. The heat flux can then be expressed using Fourier's law as,

$$q = -K \cdot \nabla T \quad (3.6)$$

which defines the theory behind heat conduction. The equation shows that the thermal conductivity K in $\text{W}/(\text{m}\cdot\text{K})$, is proportional to the magnitude of the temperature gradient. q is the heat flux measured in $\text{W}/(\text{m}^2)$ and ∇T is the temperature gradient.

Heat convection, which can be either natural or forced, was applied to the system boundaries and depends on the geometry and length of the system. When natural convection is used, the system is cooled by the surrounding air. The steady-state heat flux density is then calculated using the following equation when the convective cooling/heating is involved.

$$q_s = h \cdot A \cdot (T_s - T_m) \quad (3.7)$$

where h is the heat transfer coefficient in $\text{W}/(\text{m}^2\cdot\text{K})$, T_s represents the surface temperature and T_m is the cooling media temperature.

Since there are different materials involved in this study, then the heat

conduction or heat diffusion must be taken into account by the expression as

$$\rho \cdot C \frac{\delta T}{\delta t} = \nabla K \cdot T \cdot \nabla T + q_v \quad (3.8)$$

where ρ is the density of the material in kg/m^3 , C is the specific heat capacity $J/(kg.K)$, $\frac{\delta T}{\delta t}$ represents the difference in temperature with respect to time, ∇K is the thermal conductivity tensor and q_v is the volumetric heat generation rate per unit volume W/m^3 .

Finally, the model was prepared to analyze the temperature variations within the different layers of the power module, and the temperature profiles across it, including the boundary layers. Worth noting is that the stationary solver in COMSOL was used to evaluate the steady-state temperature distribution and the time-dependent solver to evaluate the transient temperature distribution across the power module from the chips toward the bottom layers.

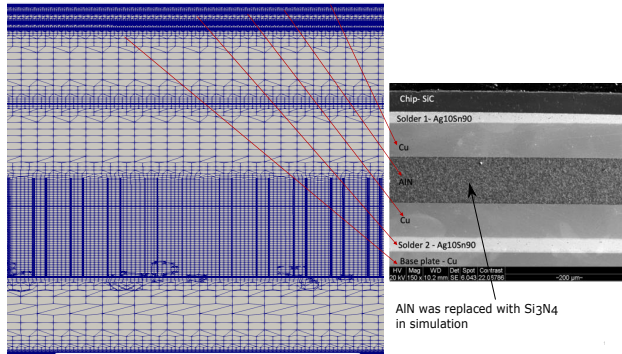
3.1.4.4 Automated CHT computation in OpenFOAM for steady-state heat dissipation

Fluid-structure interaction modeling, including CHT between solids and coolant and between solids themselves, offers the most detailed representation of heat transfer. This approach surpasses simplified models with tuned HTC in accurately determining heat transfer to the liquid.

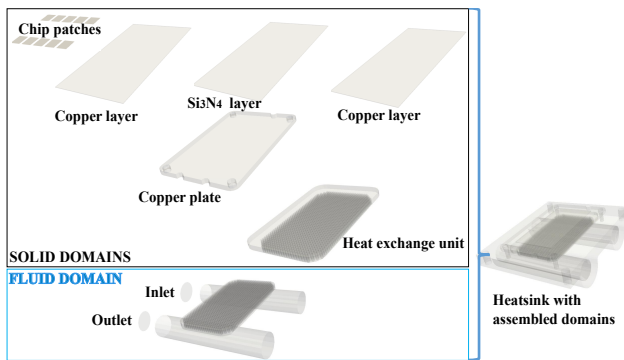
The computational workflow includes volume mesh generation, fluid domain initialization, CHT simulation, and data acquisition, all automated for efficient handling of geometry updates, parameter sweeps, and optimization. Given the 40 million finite-volume cells, a scalability study was performed on various solvers to optimize the decomposition, achieving a solution time of 11928 seconds using 36 CPUs. This setup enabled solving 40 million mesh elements across 1000 simulation points in just 3 hours, with parallelization on 36 to 5832 CPUs based on server load. This approach minimizes uncertainties and ensures high accuracy, reducing the dependence on experimental verification and extensive calibration.

Initial calculations using the inlet hydraulic diameter showed a developed turbulent field. Using glycol, the Reynolds number field varies between 6300 to 9400 in the midsection for the 6 l/min case. Reynolds number is a dimensionless quantity in fluid mechanics used to predict the flow regime (laminar, transitional, or turbulent).

To capture micron-level details (down to $30\ \mu\text{m}$, the Kolmogorov microscale; the smallest turbulent structures (eddies) size in a turbulent flow that can be resolved in a flow), the mesh is refined in the substrate layers beneath the chip. The heat sink materials and their thicknesses (solder, copper, DBC, etc.) were considered in the meshing process, with each material modeled as a separate computational domain, as shown in Figure 3.8.



(a)



(b)

Figure 3.8: (a) Computational chip-level mesh modeling of the investigated SiC CAB450M12XM3 module with layers materials. (b) Heatsink unit with assembled domains.

Accurate material layer dimensions from X-ray images were used to model distinct mesh regions with their layer counts, anisotropies, and thermal con-

ductivities, resulting in 40 million mesh elements.

All thermal anisotropies were addressed through directional thermal conductivities. The solution algorithm, implemented in OpenFOAM, solves tensors that represent a Cartesian distribution of heat transfer coefficients for all materials. Anisotropy was introduced by incorporating the directional thermal conductivities, particularly in the graphene-based cooling device. Overall, a uniform mesh distribution per domain is aimed for.

In the Finite Volume Method (FVM), the Navier-Stokes equations, including the continuity, momentum conservation, and energy equations for fluids and solids, are discretized in 3D elements. The solver script reveals that *chtMulti - RegionFoam*, a solver from Helyx (an OpenFOAM-based CFD tool), solves the transient equations, with time derivatives omitted for the steady-state variant. This solver manages the fluid domain continuity as follows.

$$\nabla \cdot (\rho \mathbf{u}) = 0 \quad (3.9)$$

where \mathbf{u} is the velocity vector and ρ is the fluid density. Subsequently, the momentum conservation in the fluid domain is modelled in 3D as [110]

$$\begin{aligned} \nabla \cdot (\rho \mathbf{u} \mathbf{u}) + \nabla \cdot (\mu \nabla \mathbf{u}) + \nabla \cdot \left(\mu \left[(\nabla \mathbf{u})^T - \frac{2}{3} \text{tr}(\nabla \mathbf{u})^T \mathbf{I} \right] \right) \\ = -\nabla p + \rho \mathbf{f} \end{aligned} \quad (3.10)$$

where \mathbf{f} is the body force vector acting on the cooling fluid domain, p is the cooling fluid pressure, μ denotes the dynamic viscosity of the cooling fluid. In (3.10), the operator *tr* takes the trace of a tensor in 3 dimensions. The energy exchange among and in the domains is modelled in both domains, in the cooling fluid as [111], [112],

$$\nabla \cdot (\rho \mathbf{u} h) + \nabla \cdot (\rho \mathbf{u} k) = \rho \mathbf{u} \cdot \mathbf{g} + \nabla \cdot (\alpha_{eff} \nabla h) \quad (3.11)$$

where h is the enthalpy of the coolant. k is the kinetic energy of the cooling fluid. The term α_{eff} is the sum of laminar and turbulent thermal diffusivities.

The energy equation, specific to the Finite Volume method (using volume center data), differs from Finite Element approaches (which use vertex data). This ensures seamless temperature field propagation between the fluid and

solid domains. The energy equation in the solid domain is modeled as follows.

$$-\nabla(\kappa\nabla T) = 0 \quad (3.12)$$

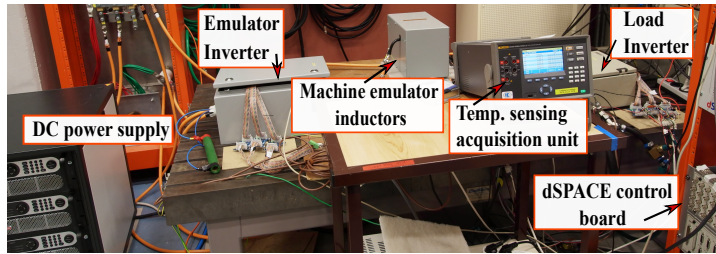
where κ is the thermal conductivity of the solid material [113].

3.2 Experimental setup

An experimental setup was created to validate the implemented CHT on the previously proposed heatsink design. An aluminum-material-based heatsink was used on a test bench featuring two identical SiC-based inverters. One inverter served as the load inverter, while the other functioned as a Power-Hardware-in-the-Loop system, emulating an electrical machine [114]. By selecting a 300 V inverter DC-Link voltage, 300 A current, and a 25 kHz switching frequency, a total power loss of 1401 W at the 180 Nm, 1500 rpm operating point of the machine emulator was applied to all three CAB450 SiC modules, resulting in 46.7 W loss per chip.

Water at 13°C (286 K) with a flow rate of 6 l/min was used as the coolant. To monitor the temperatures at the inlet, outlet, and four locations on the heatsink surface, six PT-100 sensors were installed at key points. Specifically, two sensors were placed inside the inlet and outlet, near the wall, while the remaining four sensors were positioned as close as possible to the SiC power module on the aluminum surface of the heatsink. An infrared thermal camera was also employed to observe the temperature distribution across the SiC module. Figure 3.9 illustrates the test setup, IR camera, and the position of the four sensors located on the surfaces of the heatsink.

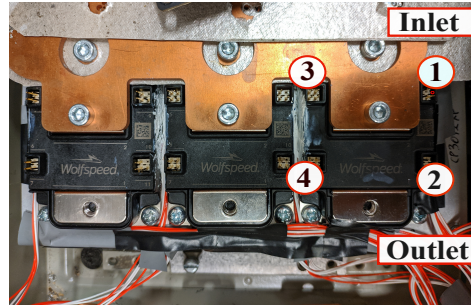
Notably, the detailed methods and corresponding findings from the thermal simulations and experimental validation (i.e., Case study 4 and Experimental setup) will be presented in Chapter 6 that follows.



(a)



(b)



(c)

Figure 3.9: (a) Test setup. (b) IR-Camera setup on the SiC power module of the inverter. (c) PT-100 sensors were located on the surfaces of the heatsink around the SiC power module.

3.3 Vehicle model and drive cycle

This thesis work utilizes two commonly used standard drive cycles mainly for energy loss analysis, lifetime predictions and efficiency assessments: the ECE-City manual and the worldwide harmonized light vehicle test cycle (WLTC) as shown in Figure 3.10. WLTC more accurately reflects real-world driving behavior by testing different driving conditions, including urban, suburban, highway, and extra-urban conditions. Note that, this case setup is integrated into the powertrain of a medium-sized battery electric vehicle (BEV), operating under the two mentioned test-drive cycles, with the vehicle's dynamic parameters given in Table 3.6.

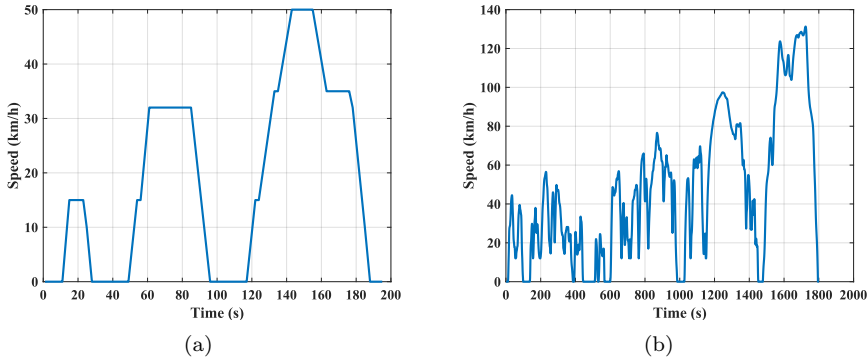


Figure 3.10: Driving schedules. (a) ECE-City-manual driving schedule. (b) WLTC driving schedule.

Table 3.6: Electric Vehicle Parameters

Parameter	Abbreviation	Value	Unit
Aerodynamic drag coefficient	C_d	0.35	-
Frontal area	A_f	2	m^2
Rolling resistance coefficient	C_r	0.007	-
Vehicle mass	m	1700	kg
Tire radius	r_t	0.3	m
Gear ratio	R_g	9.8	-

CHAPTER 4

Power and Energy Loss Analysis

This chapter is based on the following articles (Paper A & B).

- I. S. Amirpour, T. Thiringer and D. Hagstedt, "Power Loss Analysis in a SiC/IGBT Propulsion Inverter Including Blanking Time, MOSFET's Reverse Conduction and the Effect of Thermal Feedback Using a PMSM Model," IECON 2020 The 46th Annual Conference of the IEEE Industrial Electronics Society, Singapore, 2020, pp. 1424-1430.
- II. S. Amirpour, T. Thiringer and D. Hagstedt, "Energy Loss Analysis in a SiC/IGBT Propulsion Inverter over Drive Cycles Considering Blanking time, MOSFET's Reverse Conduction and the Effect of Thermal Feedback," 2020 IEEE Energy Conversion Congress and Exposition (ECCE), Detroit, MI, USA, 2020, pp. 1505-1511.

4.1 Overview

This chapter builds upon the setups described in Case Setup 1 (Section 3.1.1) and presents a comparison of power and energy losses for two SiC MOSFET modules (CAB450M12XM3 and CAS300M12BM2) and one Si-IGBT mod-

ule (FZ600R12KE3), as introduced in the aforementioned case study, within a three-phase propulsion inverter. The focus is on assessing the impact of thermal feedback on power and energy loss calculations. Two drive cycles, the ECE-City manual, and the WLTC patterns, were selected for the loss comparisons. Figure 4.1 provides an overview of the analysis.

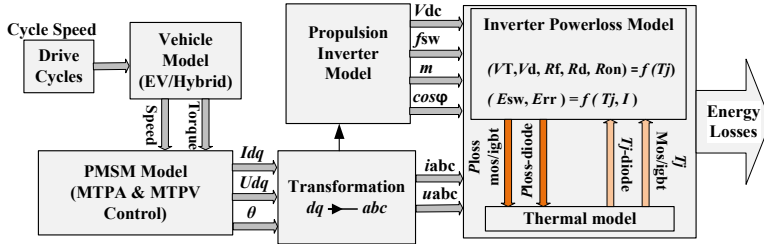


Figure 4.1: Analysis overview.

As discussed in the above-mentioned case study, the d - and q -axis reference currents, derived from PMSM FEA analysis, were input into the MTPA/MTPV control strategy. Using these control algorithms, key operating points across the machine's torque-speed region were mapped and applied in the inverter loss calculation model, accounting for the junction temperature feedback of the semiconductor devices.

4.2 Method

This study follows a two-step methodology: first, numerically modeling the inverter's power losses, with the incorporation of the MOSFET reverse conduction and blanking time models. The second step involves applying the numerical temperature feedback model to the calculated power losses and quantifying its impact on the results.

4.2.1 MOSFET reverse conduction

As discussed in Section 2.2.2, a key difference between MOSFETs and IGBTs is their current conduction behavior. In Si IGBTs, the reverse current flows through an anti-parallel diode, whereas MOSFETs can conduct in the oppo-

site direction through their reverse conduction ability. This capability was numerically incorporated into the SiC-based inverter loss calculations.

Figure 4.2 shows the diode and MOSFET currents in a phase leg of the CAS300 inverter, when considering the MOSFET reverse conduction.

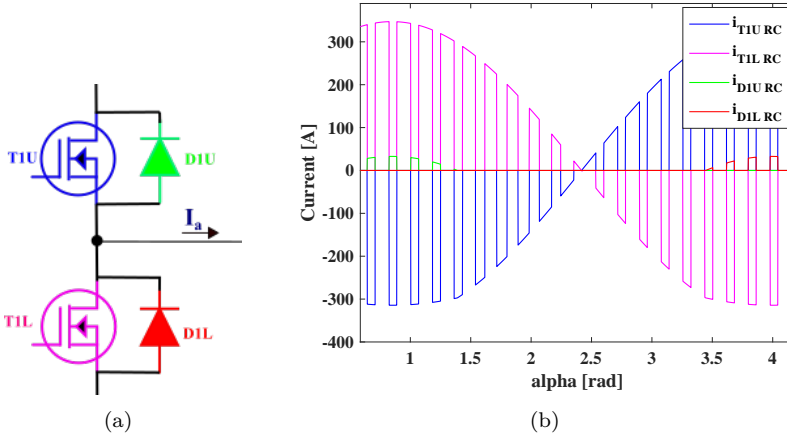


Figure 4.2: (a) One phase leg (half-bridge) of a three-phase inverter with parallel conduction of diode and MOSFET channel. (b) Impact of MOSFET's reverse conduction (RC) on diode and MOSFET currents as a function of $\alpha = 2\pi ft$ in a phase leg of the CAS300 inverter.

In Figure 4.3, the losses with and without reverse conduction of MOSFET are shown for the upper diode and MOSFET in a phase leg of the SiC-based inverter CAS300M12BM2 [101].

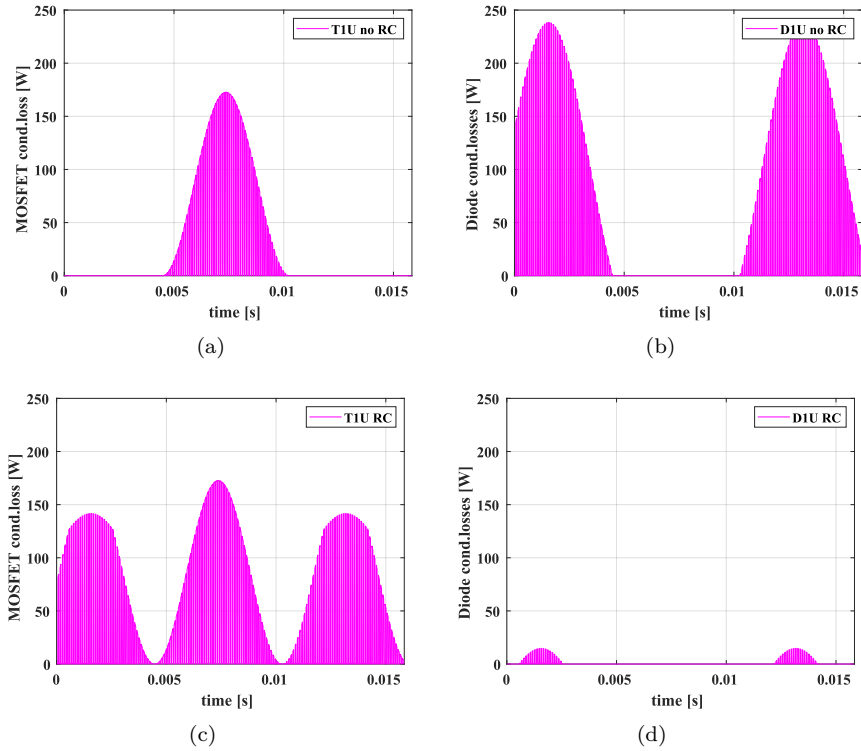


Figure 4.3: MOSFET and Diode conduction losses in CAS300, SiC inverter, upper MOSFET and Diode in a phase leg. (a) MOSFET without MOSFET reverse conduction (RC). (b) Diode without MOSFET reverse conduction (RC). (c) MOSFET with MOSFET reverse conduction (RC). (d) Diode with MOSFET reverse conduction (RC).

As is evident from Figures 4.3 (b) and (d), parallel conduction significantly reduces the conduction losses of the diodes and also the total losses in the switch position, as the current is shared between the diode and the MOSFET. The losses are calculated based on the operating condition of the studied PMSM, characterized by high current magnitude (272 A) corresponding to high torque and low speed (at 89 Nm, 1290 rpm) during the WLTC drive schedule. This operating point represents one of the worst-case conditions for power loss in urban driving cycles.

4.2.1.1 Blanking time

Since the diode only conducts during the blanking time, incorporating this period into the loss calculation increases the inverter's total conduction losses. Figure 4.4 shows the diode and MOSFET currents in a phase leg of the CAS300 inverter, with the utilization of blanking time, when also considering the MOSFET reverse conduction. In addition, Figure 4.5 shows the conduction losses of the upper diode in a phase leg of the CAS300 inverter, both without and with blanking time, considering MOSFET reverse conduction. The operating condition for calculating the diode conduction losses is the same as the one used in the previous figure.

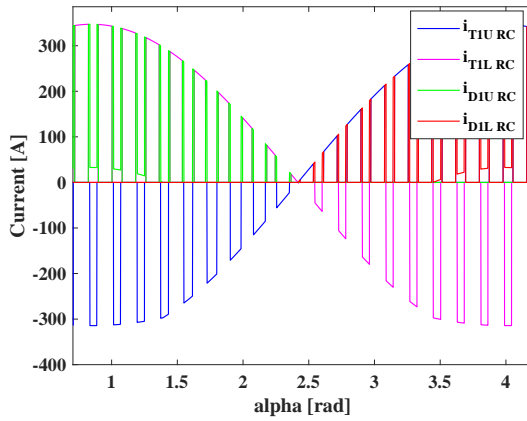


Figure 4.4: Impact of blanking time on diode and MOSFET currents as a function of $\alpha = 2\pi ft$ with considering the MOSFET's reverse conduction in a phase leg of CAS300 inverter.

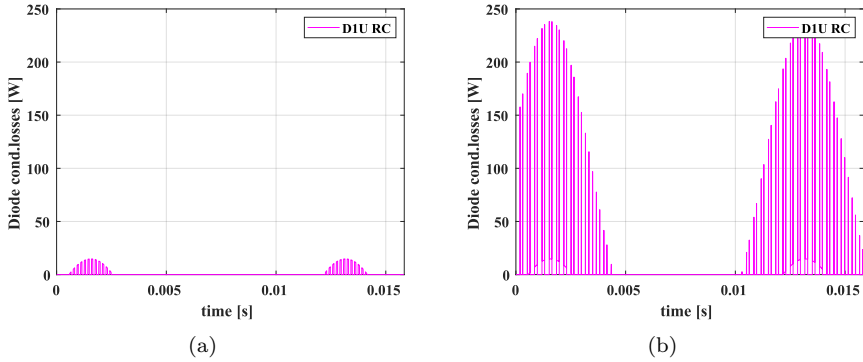


Figure 4.5: Diode conduction loss in a phase leg of CAS300 inverter. (a) With no blanking time. (b) With blanking time.

4.2.2 Thermal feedback

Thermal feedback was integrated into the loss models by calculating losses iteratively based on temperature. The devices' parameters (V_T , V_d , R_f , R_d , R_{on} , E_{sw} , and E_{rr}) were determined accounting for the present thermal situation. This was achieved by using an iterative procedure, where losses and temperatures were iterated until convergence. This was done both for the conduction and switching losses. Figure 4.6 shows the flowchart for estimating the junction temperature in steady-state using the thermal calculation model given in Figure 3.1, and equation 3.4, discussed in Case setup 1.

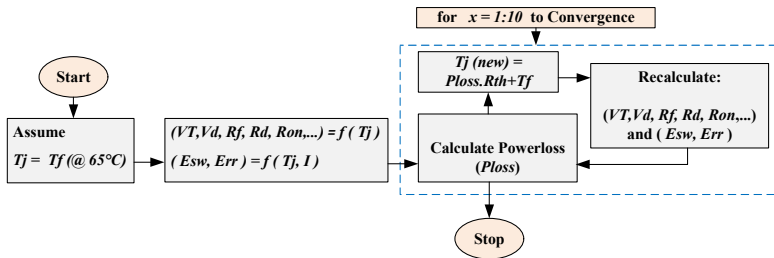


Figure 4.6: Flow chart for estimating the junction temperature in steady-state.

4.3 Key results and discussion

Table 4.1 presents the results quantifying the temperature feedback on the power losses of the SiC and Si-IGBT modules at the operating point of 89 Nm and 1290 rpm (high torque, low speed on WLTC) from the studied PMSM (given in Case setup 1). The first indications, as shown in the table, reveal a significant decrease in diode conduction losses for the two SiC modules compared to the Si-IGBT module. This can to a large extent be attributed to the MOSFET's reverse conduction capability, which allows current sharing between the diode and MOSFET.

Table 4.1: Average conduction and switching losses of the three compared inverters with and without thermal feedback at one high torque, low current operating point on WLTC.

CAB450M12XM3							
<i>@ 89Nm 1290rpm T_f = 65°C</i>	Cond. loss [W]	Cond. thermal feedback [W]	Diff. %	Sw. loss [W]	Sw. thermal feedback [W]	Diff. %	T _{junc.} thermal feedback [°C]
MOSFETs	226.4	233.2	3	42	42	0	75.7
Diodes	32.8	32.6	-0.6	1.7	1.7	0	75.7
Inverter	259.2	265.8	2.5	43.7	43.7	0	
CAS300M12BM2							
MOSFETs	314.8	326.0	3.6	45	45	0	73
Diodes	7.2	7.3	1.4	0	0	0	70.5
Inverter	322	333.3	3.5	45	45	0	
FZ600R12KE3							
IGBTs	341	343.6	0.76	182.8	190.7	4.3	74.8
Diodes	242.3	238.5	-1.6	141	151.4	7.4	76.4
Inverter	583.3	582.1	-0.2	323.8	342	5.7	

A loss increase of up to 3.5% for the conduction losses of the SiC inverters and up to 6% for the switching losses of the IGBT inverter are observed for the selected operating point on the WLTC driving schedule. The lower loss in the SiC-MOSFETs is most pronounced for lower temperatures, since at higher temperatures, the conduction losses increase less in the Si-IGBTs. Si-IGBTs have substantially higher switching losses, which limits their effectiveness in high-frequency applications. In addition, the IGBT switching losses increase noticeably with temperature, and this increase is even more pronounced than that of their conduction losses. In contrast, SiC-MOSFETs show almost no

temperature dependence for switching losses, which is apparent when studying the losses during both investigated driving cycles. Additionally, in SiC modules, the increase in diode conduction losses with temperature is much lower than in MOSFET channels due to the diode's lower dynamic resistance increase. For example, as shown in Figure 4.7, when the junction temperature reaches 150°C, the current share in the MOSFET channels decreases by up to 100 A, while the diode current increases. The negative temperature coefficient of the diodes' voltage drop also influences the current distribution in SiC-MOSFET modules.

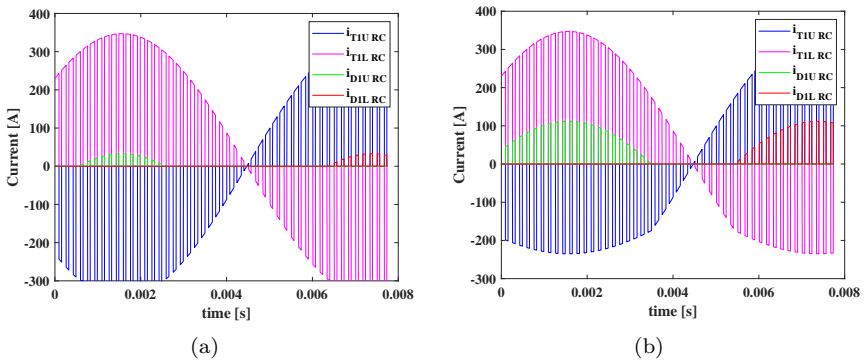


Figure 4.7: MOSFET and diode currents in a phase leg of CAS300 inverter at the chosen operating point over WLTC. (a) at 65°C junction temperature. (b) at 150°C junction temperature.

The total energy losses over 12 years (approximately the lifetime of an EV), assuming 1 hour of driving per day, for the three compared propulsion inverter modules are presented in Figure 4.8 (a).

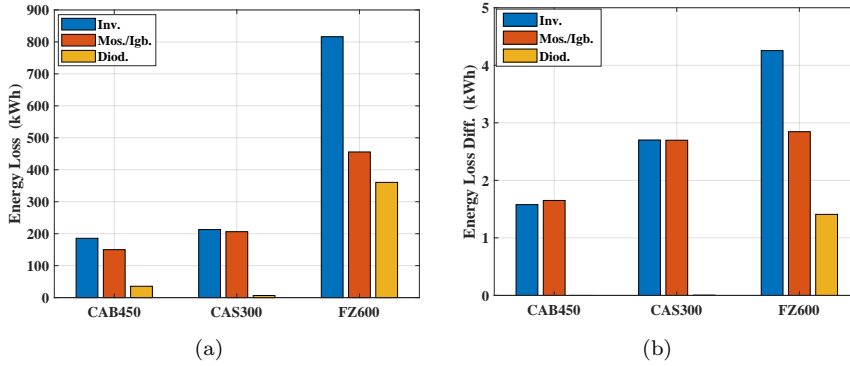


Figure 4.8: (a) Energy loss in 12 years, 1-hour driving a day, in the three compared inverters, (MOSFETs /IGBTs and diodes) with thermal feedback over WLTC. (b) Energy loss difference between thermal and no thermal effect.

The data, derived from the WLTC operation, shows that the two SiC inverters offer up to 4 times lower total energy losses compared to the Si-IGBT inverter. Figure 4.8 (b) compares the energy loss differences with and without accounting for thermal feedback on the loss calculations. With thermal feedback, the FZ600 inverter exhibits a higher loss increase of over 4 kWh, while the SiC inverters show an increase of 1-3 kWh, with minimal effect on the SiC diodes.

CHAPTER 5

Lifetime Prediction Analysis for SiC- and IGBT-Based Inverters

This chapter is based on the following articles (Paper C & E).

- I. S. Amirpour, T. Thiringer and D. Hagstedt, "Mission-Profile-Based Lifetime Study for SiC/IGBT Modules in a Propulsion Inverter," 2021 IEEE 19th International Power Electronics and Motion Control Conference (PEMC), Gliwice, Poland, 2021, pp. 264-271.
- II. S. Amirpour and T. Thiringer, "Mission-Profile-Based Lifetime study for SiC Module Chips using Graphene Films," 2022 IEEE Energy Conversion Congress and Exposition (ECCE), Detroit, MI, USA, 2022, pp. 1-7.

5.1 Overview

This chapter extends the setups described in Case Setup 1 (Section 3.1.1) to analyze the lifetimes of two SiC power modules (CAB450M12XM3 and CAS300M12BM2) and one Si-IGBT module (FZ600R12KE3) in a three-phase

propulsion inverter, as outlined in the aforementioned case study. Lifetime comparisons use the ECE-City manual and the WLTC drive cycles as mission profiles. In addition, the semiconductors' lifetime under different heatsink fluid flow rates is compared for the three modules across both drive cycles. An overview of the analysis is illustrated in Figure 5.1.

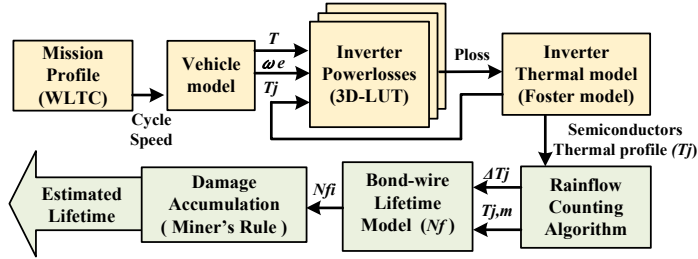


Figure 5.1: Analysis overview.

The d - and q -axis reference currents, obtained from the PMSM finite element analysis, were fed into the MTPA/MTPV control strategy to identify the machine's key operating points across the torque–speed range. These points were then applied in the inverter loss model that incorporates semiconductor junction temperature feedback. This approach generated the thermal profiles of the three modules over the two driving patterns, which were then used in the subsequent lifetime prediction analysis, detailed in the following section.

5.2 Method

The main methodology in this study involves generating thermal profiles for the inverter's power semiconductors, then applying a numerically implemented rainflow counting algorithm [64] for the subsequent lifetime prediction analysis.

5.2.1 Thermal calculation model

Following the lumped parameter configuration for the investigated power modules (Case Setup 1, Figure 3.1), a Foster thermal network from the semiconductor junction to the cooling fluid was implemented in Simulink. The model

provides the thermal feedback for the inverter’s power losses. Note that, the inverter loss itself was modeled in Simulink as a 3D look-up table (LUT), loaded with the loss values that were already calculated, (according to the method in Section 4.2 of the previous chapter).

Accordingly, the 3-D LUT outputs the power loss associated with the vehicle’s torque and speed over the drive cycle, as well as the devices’ junction temperature. Consequently, the thermal profiles of the semiconductors were derived for both driving cycles.

5.2.2 Rainflow counting

Rainflow counting [64] is an algorithm applied to the generated thermal loading profiles to convert randomly fluctuating thermal profiles into regulated thermal cycles for use in lifetime models. The method extracted the change in junction temperature (ΔT_j) as well as the mean junction temperature (T_{jm}), and the number of cycles of the Si-IGBT and SiC-MOSFET modules for the used lifetime model in this study, previously discussed in Section 2.2.3.

Figures 5.2 and 5.3 present the thermal transient profiles and the 3D temperature histograms. These plots respectively depict the temperature variation, mean temperature, and number of cycles for one SiC module and one IGBT module’s devices, under both the ECE-City manual and WLTC drive cycles.

As illustrated by the figures, the histograms show that the WLTC drive cycle exhibits higher amplitude temperature swings and greater mean temperature values than the ECE-City manual. This results in a more intense thermal profile, featuring larger and more varied temperature fluctuations due to the WLTC’s more aggressive acceleration and deceleration events.

Furthermore, a comparison of SiC and Si-IGBT devices under each driving cycle indicates that the SiC modules—particularly their diodes—experience lower thermal stress than their Si-IGBT counterparts. This is largely due to the MOSFET’s reverse conduction, which notably reduces diode conduction losses. Furthermore, because SiC-MOSFET modules have much lower switching losses, their overall power losses are substantially less than those of Si-IGBTs. Table 5.1 summarizes the temperature swings observed for all three modules investigated in this study.

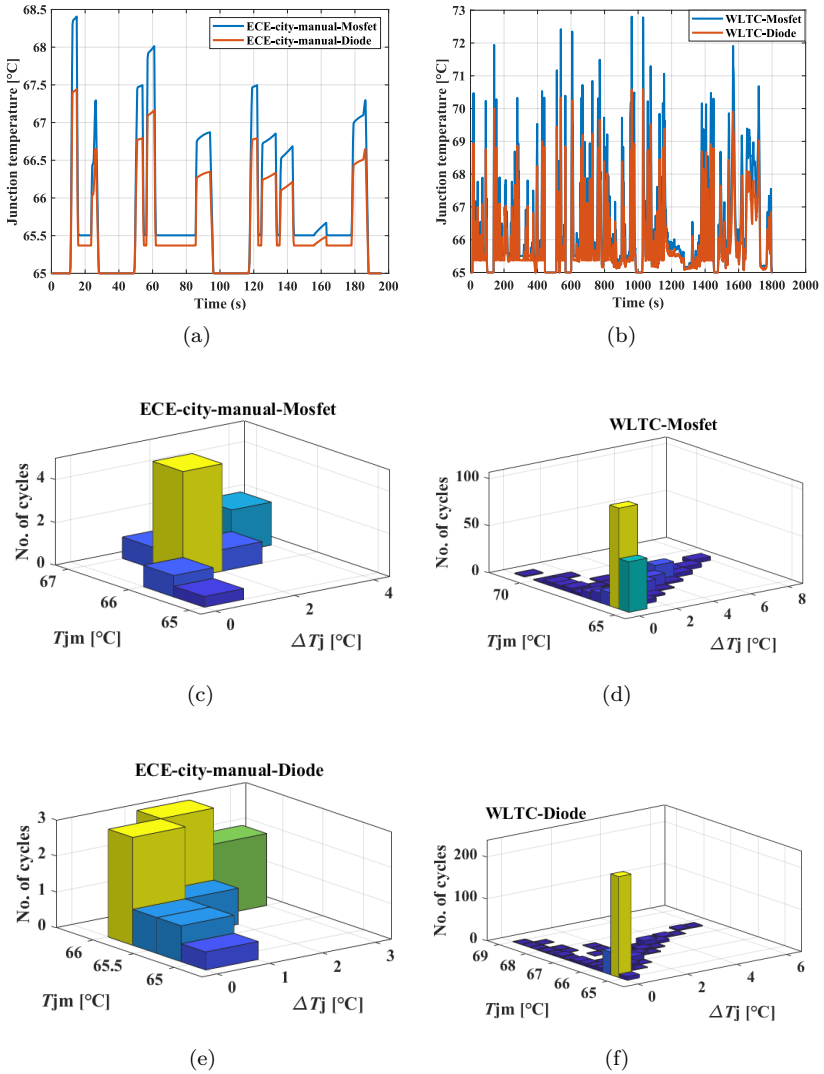


Figure 5.2: (a) and (b) Thermal transient profiles over two driving cycles for CAS300 devices. (c) and (d) 3D-histograms generated from rainflow counting for MOSFETs. (e) and (f) 3D-histograms generated from rainflow counting for diodes.

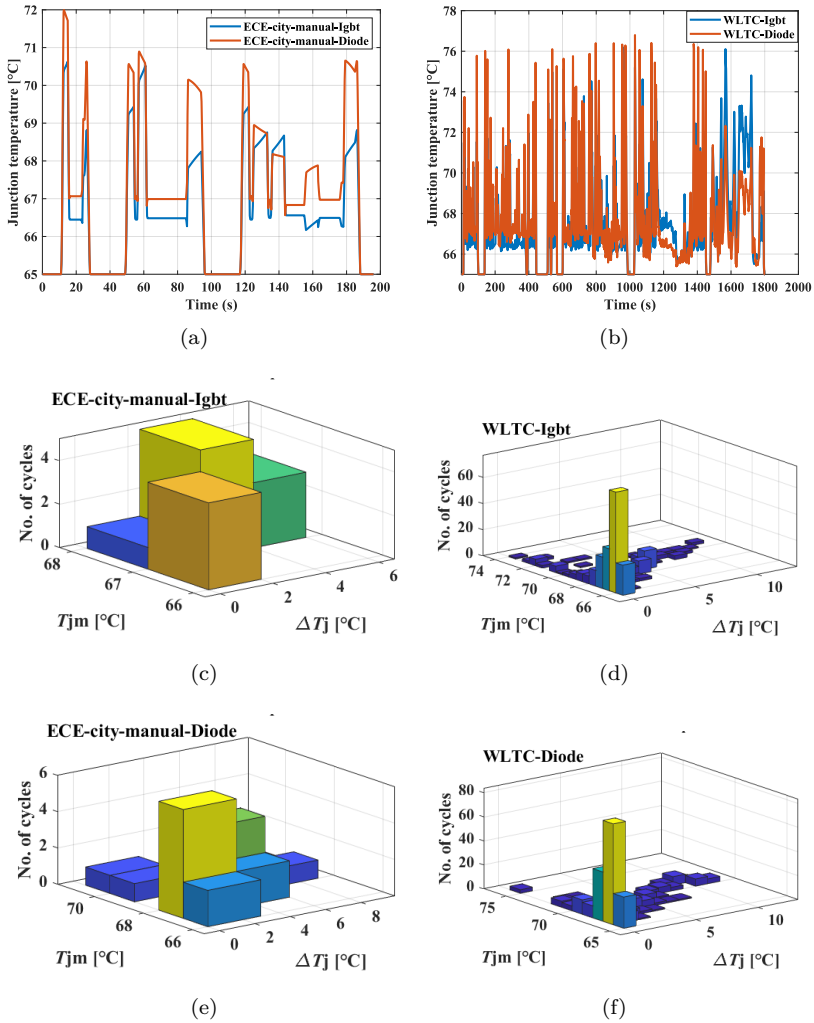


Figure 5.3: (a) and (b) Thermal transient profiles over two driving cycles for FZ600 devices. (c) and (d) 3D-histograms generated from rainflow counting for IGBTs. (e) and (f) 3-D histograms generated from rainflow counting for diodes.

Table 5.1: Temperature Swings of the compared modules over the two mission profiles.

Temp. Swing (ΔT_j)	CAB450		CAS300		FZ600	
	WLTC	ECE	WLTC	ECE	WLTC	ECE
Mos./Igbt.	7.4°C	3.4°C	7.8°C	3.4°C	11.2°C	5.7°C
Diode	7.4°C	3.4°C	5.6°C	2.5°C	12°C	7°C

5.3 Key results and discussion

As previously discussed in Chapter 1, Section 2.2.3, thermal cycling in the range of seconds is the main driver of bond wire damage [11], prompting its inclusion in the lifetime analysis. The lifetime is determined by the damage induced by temperature cycles over the chosen mission profile period, using the models introduced in the aforementioned section. Table 5.2 shows the accumulated damage on the three power modules (per single run of both mission profiles), and Figure 5.4 illustrates the estimated lifetimes of these modules under the two mission profiles.

Table 5.2: Accumulated damage on the compared modules for a single run of the two mission profiles.

Accumulated Damage [D]	CAB450		CAS300		FZ600	
	WLTC	ECE	WLTC	ECE	WLTC	ECE
Mos./Igbt.	4.2e-10	2.1e-12	5.8e-10	2.3e-12	2.8e-9	3.3e-11
Diode	4.2e-10	2.1e-12	1.8e-10	7.4e-13	1.1e-8	1.3e-10

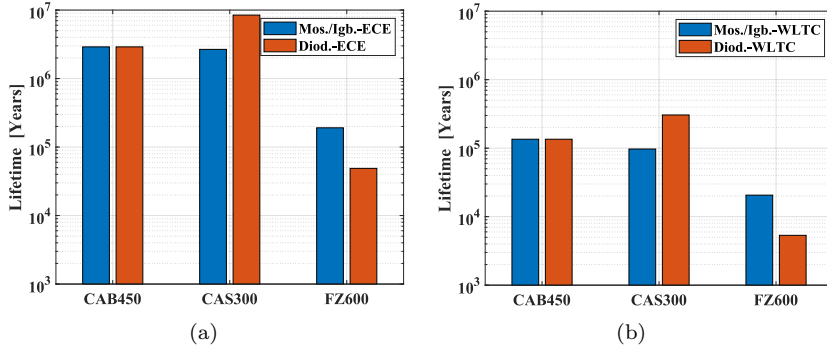


Figure 5.4: Estimated lifetime comparisons of the three modules' devices for the two mission profiles. (a) ECE-City-manual driving schedule. (b) WLTC driving schedule.

As anticipated, the SiC devices—particularly their diodes—experience significantly lower accumulated damage than the Si-IGBTs and their antiparallel diodes, thanks to reduced thermal stress on the SiC devices. Moreover, the WLTC driving cycle has a stronger impact on device lifetime compared to the ECE-City manual.

Figure 5.5 illustrates how varying the heatsink's fluid flow rate influences the lifetime predictions for both mission profiles. A lower fluid flow rate increases the heatsink's thermal impedance, leading to higher thermal stress and greater damage to the modules' devices. As anticipated, the WLTC drive cycle exhibits a more pronounced effect than the ECE-City manual.

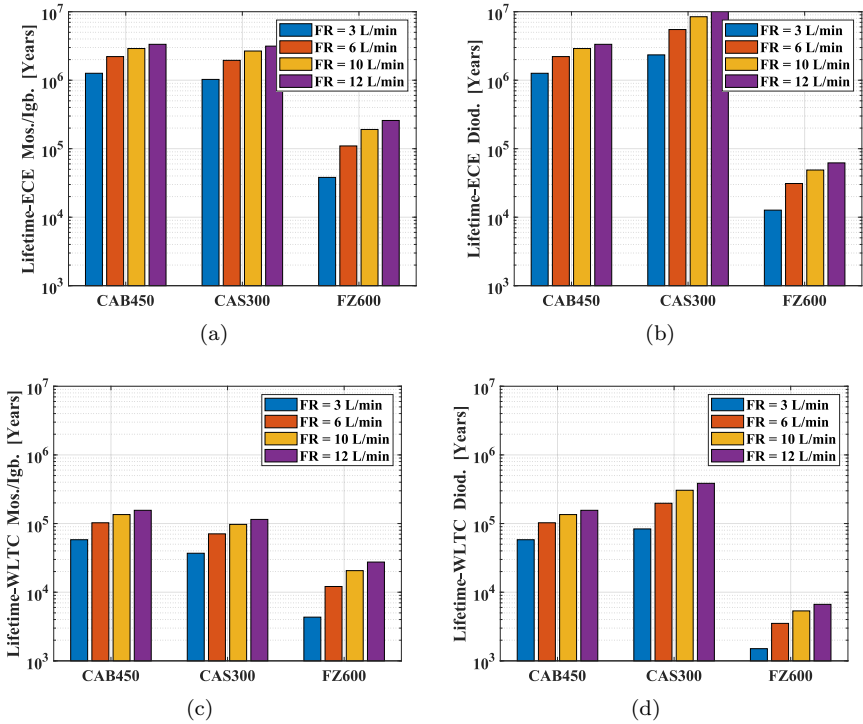


Figure 5.5: Estimated lifetime comparisons of the three modules' devices for ECE (top) and WLTC (bottom) vs different flow rates of the heatsink fluid.

CHAPTER 6

Thermal Management Enhancements Using Graphene

This chapter is based on the following articles (Paper D & F).

- I. S. Amirpour, T. Thiringer, Y. Sharifi, M.M.K. Samani "Improving of Heat Spreading in a SiC Propulsion Inverter using Graphene Assembled Films", *Advances in Science, Technology and Engineering Systems Journal*, vol. 6, no. 6, pp. 98-111 (2021).

- II. Sepideh Amirpour, Raik Orbay, Torbjörn Thiringer, Majid Kabiri Samani, Georgios Mademlis, Daniel Larsson, Andreas Andersson, "Highly thermal conductive graphene-based heatsink tailored for electric propulsion SiC-based inverter", *Applied Thermal Engineering*, Volume 243, 2024, pp. 122548, ISSN 1359-4311.

It should be noted that Section 6.3.3 of this chapter is based on joint work with Raik Orbay, whose contributions to CFD/CHT simulation setups, CHT methodology, and computations are duly acknowledged. Additionally, Georgios Mademlis's assistance with the test setups and experiments outlined in Section 6.3.4 is gratefully acknowledged.

6.1 Overview

This chapter builds on the simulation and experimental setups, from Case setup 4 (subsection 3.1.4) and experimental setup (Section 3.2), aiming to improve heat spreading and in this way make the cooling in the chosen half-bridge SiC power module (CAB450M12XM3) more effective. Through the usage of graphene as a novel heat-spreading material, both in power module packaging and in a pin-fin-based heatsink design, this work explores a powerful possibility of improving thermal management in power electronics.

As discussed in the above-mentioned Case setup, a detailed thermal model of the CAB450 module was first built in COMSOL Multiphysics and examined under the inclusion of graphene in the power module packaging. To simulate a real-world cooling structure, a multidisciplinary approach in OpenFOAM was then employed to design and analyze a liquid-cooled heatsink—using a graphene cold plate including graphene pin-fins instead of aluminum.

Figure 6.1 illustrates the thermal simulation process within the powertrain analyzed in this thesis.

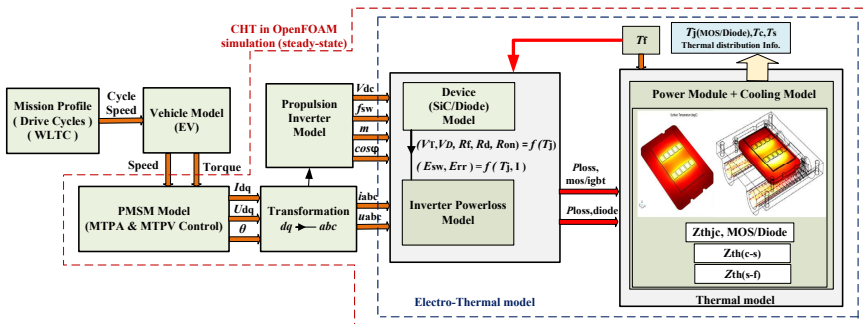


Figure 6.1: Analysis overview.

The process, shown in Fig. 6.1, was implemented to meet the inverter’s thermal dissipation requirements. It integrates electrical modeling, control algorithms, power loss analysis, as well as thermal and fluid modeling. As illustrated, the modeled light-duty electric propulsion system includes a permanent magnet synchronous machine (PMSM) along with its control system. It also features a three-phase, 2-level SiC-based inverter, coupled with a model

of the SiC-based devices used. The electro-thermal model incorporates the inverter's power loss model and the proposed heatsink model.

Initially, the flux linkage maps, ψ_d and ψ_q , produced in Ansys Maxwell, coupled with the specified electric drive parameters listed in Case study 1 (subsection 3.1.1), are employed to create a PMSM model in MATLAB. The motor control strategies, MTPA and MTPV [73] are implemented in MATLAB. Subsequently, the generated current and voltage reference maps from the PMSM control are then loaded into the inverter and inverter loss model for loss calculations.

Finally, the losses calculated based on the inlet temperature are applied to the SiC power module chips, which are emulated to resemble a real module (as detailed in Case study 4) for the thermal analysis in the first phase of simulation using COMSOL. In the next design phase, the module is integrated with the proposed heat exchange unit (in Case setup 4), for a more detailed thermal analysis in OpenFOAM.

Worth noting is that, the multidisciplinary design process presented here can simulate both the transient and steady-state (constant) thermal performance of the inverter and establish a thorough and realistic thermal analysis methodology to assess the performance of the heatsink by introducing graphene instead of metallic materials.

6.2 Method

The primary methodology in this study involves integrating graphene into two simulation setups, in COMSOL and OpenFOAM (discussed in Case Study 4) applied to both the SiC module packaging and the designed heatsink attached to the module, respectively. This integration aims to enhance the thermal performance of the SiC module by improving heat transfer from the semiconductor chips to the cooling fluid.

6.2.1 Graphene assembled film in the module packaging

As mentioned earlier, an effective solution for heat dissipation in high-power applications can be achieved by incorporating materials with high thermal conductivity into the cooling path [91]. In this study, graphene—one of the most promising materials with these properties—has been utilized to optimize

the thermal impedance of the power module and facilitate uniform, rapid heat spreading across the module.

To achieve this goal, a graphene layer has been positioned as close as possible to the chips, which serve as the heat source, depicted in Figure 6.2. The graphene layer features an in-plane thermal conductivity of 2900 (W/m · K) in the x and y directions and a cross-plane thermal conductivity of 14 (W/m · K) in the z direction. These directional properties were carefully selected to conduct and spread the heat as efficiently as possible across the module surface and into the lower layers.

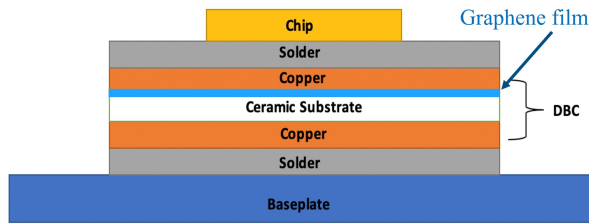


Figure 6.2: Thermal stack-up of a power module .

It is worth mentioning that freestanding graphene films (GFs) have shown greater potential than single/few-layer graphene in achieving high thermal and mechanical performance for the thermal management of high-power electronics [91]. In this work, 6 μm thick graphene films are used to achieve an optimal layer thickness, balancing thermal conductivity, which is highly dependent on graphene layer thickness [91]. The graphene layer is positioned beneath the first copper layer, ensuring a realistic placement that avoids compromising the module’s electrical conductivity, which could be affected by the poor insulating properties of graphene.

In addition, a contact resistance is set to $1.1 \times 10^{-8} \text{ K} \cdot \text{m}^2/\text{W}$ between the graphene layer and the other substrates to achieve the appropriate thermal coupling between the layers [98].

The thermal properties of graphene are given in Table 6.1 (The material and thicknesses of the other layers in the module’s thermal stack-up are provided in Case setup 4, Table 3.5).

6.2.2 Graphene-based heat exchange unit including pin fins in the heatsink

To model the graphene-based heatsink, the heat exchange unit, including the cold plate and pins, was constructed using graphene, (Figure 3.6 given in Case Study 4 illustrates the CAD drawing of the heatsink, including the heat exchange unit and its pin structure). As mentioned earlier, the thermal conductivity levels depend greatly on the thickness of the layer. The lower the thickness, the higher the thermal conductivity [91]. Therefore, the trade-off between the thermal conductivity and the thickness of the films should be precisely taken into account in the design specification. To create the pins, 1 μm thick graphene films with an in-plane thermal conductivity of 2900 W/mK in the x and z directions and a cross-plane thermal conductivity of 14 W/mK in the y direction have been chosen and assembled to make a 1 mm section dimension of the pin fins.

Moreover, the proposed heat exchange unit is to carry the heat in the principal direction between the chips and the coolant. Therefore, aligned with the flow through the pins, the x direction is the second important heat transfer route as a design parameter for the graphene heatsink.

Notably, aluminum as a heatsink material, is already a good heat conductor. Its thermal conductivity is uniform in all directions, with no anisotropies. In contrast, for the graphene-based cooling device, material anisotropies must be considered. This was done by incorporating the above-mentioned directional thermal conductivities, which were addressed through the detailed CHT model used in this work.

Table 6.1 shows the thermal properties of graphene compared with aluminum as well as the used thermal paste material (TIM).

Table 6.1: Thermal properties of graphene, aluminum, and TIM.

Material	Thermal conductivity, K (W/m.K)	Density, ρ (kg/m ³)	Heat capacity, C (J/(kg.K))
Graphene	(x, y, z) = (2900, 14, 2900)	2267	720
Aluminium	237	2700	904
TIM	5	2250	150

6.3 Key results and discussion

In this section, the key results are divided into two parts: first, the steady-state and transient thermal simulations conducted in COMSOL for the SiC power module, and second, the steady-state CHT simulation in OpenFOAM, which models the complete cooling structure of the power module attached to the pin-fin heatsink.

6.3.1 Steady-state thermal computation of the power module with/without graphene layer

The stationary solver in COMSOL was used to evaluate the steady-state temperature distribution across the power module, from the chips to the bottom layers. Heat distribution was analyzed by applying a 3-D cut-line from the middle chip to the base plate, as shown in Figure 6.3. The middle chip was selected because it experiences the highest thermal stress.

Figure 6.4 and 6.5 show the 2-D and 3-D temperature distribution across the power module, both with and without the inclusion of the graphene layer.

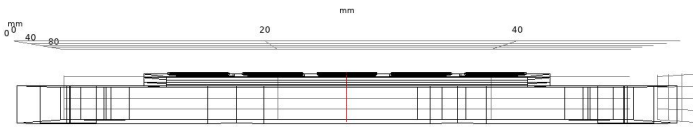
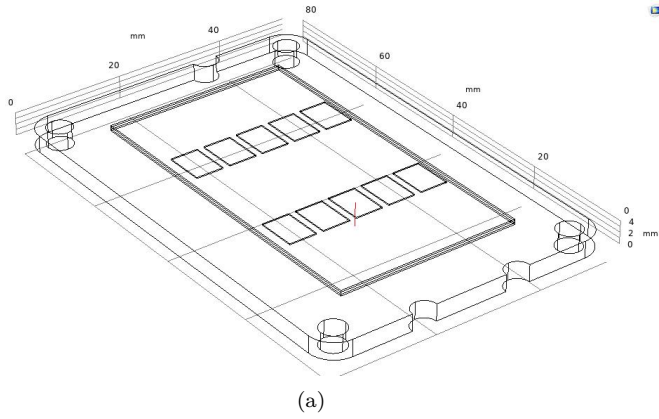
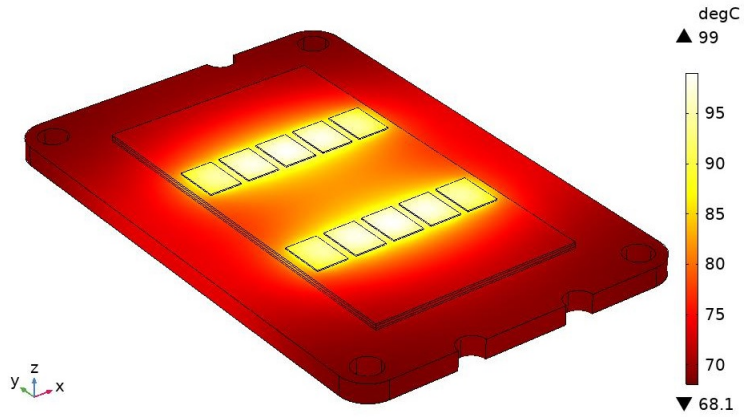
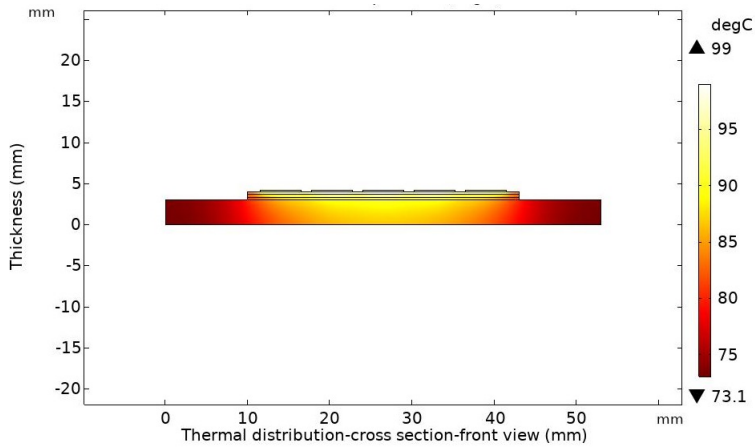


Figure 6.3: 3-D cut-line across the module for the temperature measurements. (a) Top view. (b) Side view.



(a)



(b)

Figure 6.4: Temperature distribution across the CAB450 SiC power module without graphene. (a) 3-D view. (b) 2-D view.

As shown in the figures, with an applied power loss of 126.2 W per chip, the average maximum temperature of the chips is around 99°C in the case with no graphene layer in the module, Figure 6.4.

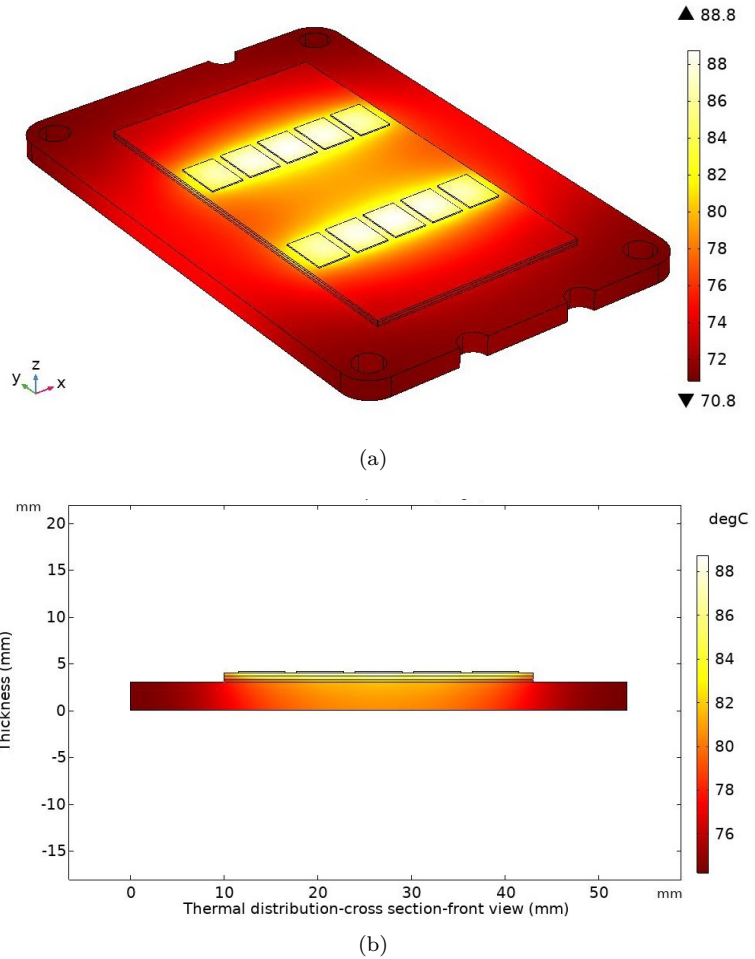


Figure 6.5: Temperature distribution across the CAB450 SiC power module with graphene. (a) 3-D view. (b) 2-D view.

While, with the graphene layer included in the module, the temperature is reduced to 88°C, reflecting a nearly 10°C reduction, see Figure 6.5.

6.3.2 Transient thermal computation of the power module, with/without graphene layer using WLTC driving cycle

Since the inverter load constantly varies, real-time thermal computations are essential to accurately quantify the thermal behavior and reliability of the inverter. Therefore, the time-dependent solver in COMSOL was used to assess the transient temperature distribution across the power module, from the chips to the bottom layers, over the WLTC driving schedule, which includes both the urban and highway phases.

First based on the vehicle model used in this thesis, the required torque and speed values for the PMSM model (presented in Case setup 1) were determined. The values were then utilized for the power loss calculation over the WLTC drive test and thereafter for the thermal loading in COMSOL. To measure the transient heat distribution, a 3-D cut-line from the middle chip to the base plate was used similarly as done in the steady-state simulation and then the calculated power losses over WLTC were applied to the chips as the heat sources. Figure 6.6 illustrates the calculated power losses over the WLTC pattern.

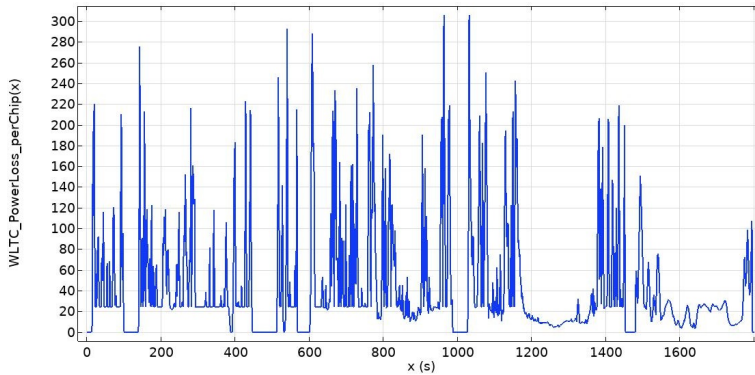


Figure 6.6: Calculated power losses over WLTC.

As can be seen in Figure 6.6, the highest calculated power losses occur around 1000 seconds, corresponding to the speeds and torques of the PMSM based on the vehicle model parameters. Therefore, the temperature distributions for both cases, with and without graphene, were evaluated at 1033 seconds, shown in Figure 6.7.

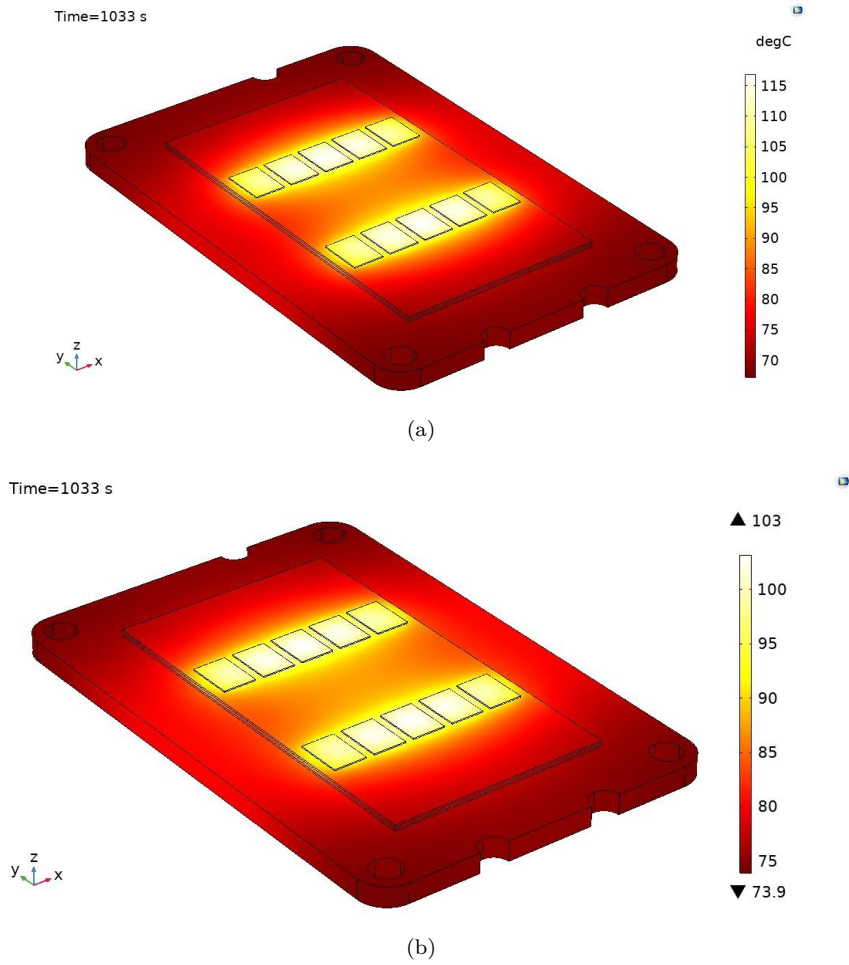


Figure 6.7: Temperature distribution across the power module. (a) Without the graphene layer. (b) With the graphene layer.

As shown in Figure 6.7, a temperature reduction of approximately 15°C per chip at 1033 seconds is observed when using the graphene layer in the power module. Furthermore, a closer inspection of the heat distribution across the module reveals a more uniform distribution with graphene. With the graphene layer, the heat is more evenly spread across the base plate, whereas, in the case without graphene, the heat is concentrated in the center, where the chips are located.

Finally, Figure 6.8 illustrates the thermal profile comparison over the WLTC driving schedule per chip between the two cases, with and without the graphene layer. As depicted in the figure, the incorporation of the graphene layer results in a lower average junction temperature per chip, which can contribute to a lower overall operating temperature of the semiconductor power module.

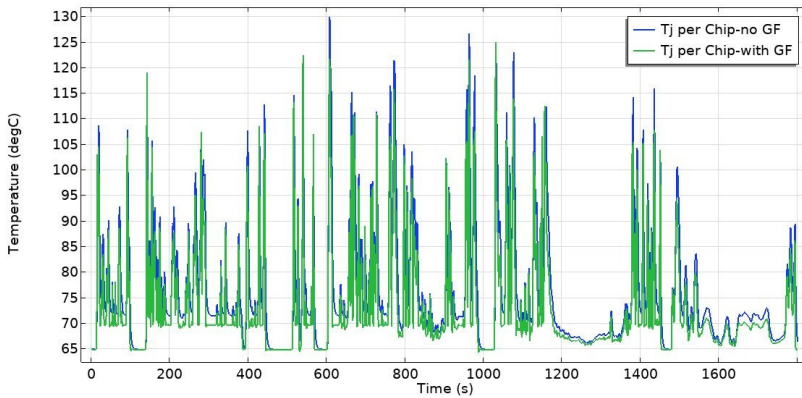


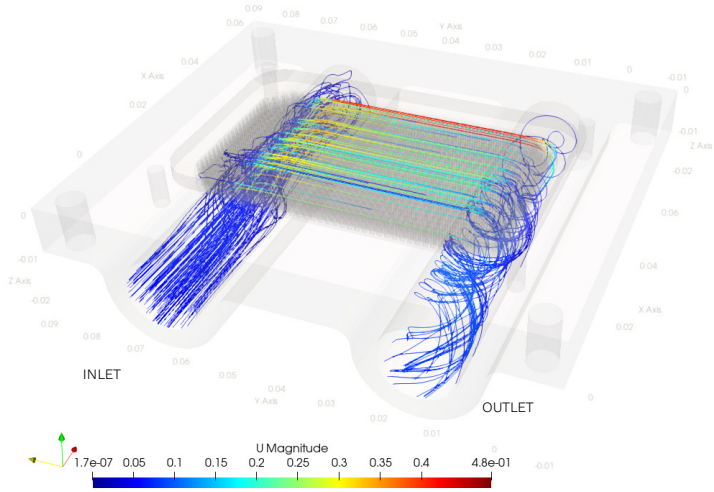
Figure 6.8: Comparison of the average junction temperature profile of each chip over the WLTC drive cycle.

It is worth noting that the effect of graphene usage is more pronounced in high-power applications, where the use of high voltage and current levels necessitates a larger number of chips for the same heatsink conducting area.

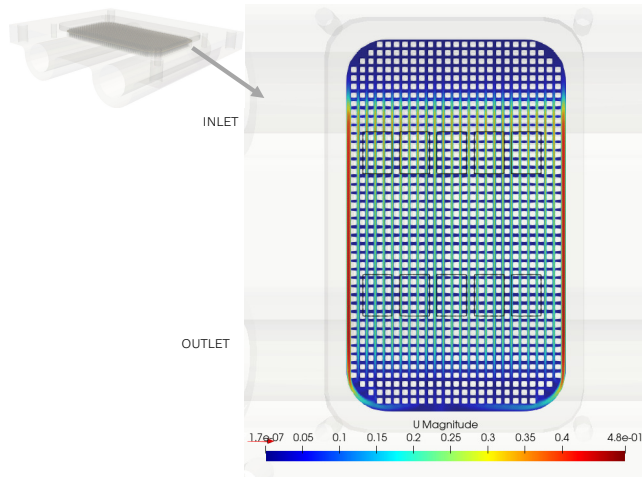
6.3.3 Results of CHT computations applied to the designed aluminum and graphene pin fins based heatsinks

First, the aluminum heat exchange unit in the modular heatsink assembly was positioned immediately under the chips. The thermal interface material (TIM) was chosen with a thickness of $75\ \mu\text{m}$ to better represent the thermal coupling between the power module and the heatsink. Accordingly, the heat transfer to the surfaces of the heatsink, at the reference temperature of 338 K (65°C) for two different fluid flow rates of 1 and 6 l/min was measured. It should be noted that the heatsink was exposed to a heat energy injection of 34.5 W power loss per chip. Similar CHT computation steps for the aluminum-based heatsink were performed for the graphene counterpart for a fair comparison.

Figure 6.9 illustrates the streamlines in the fluid domain as well as the top view of the xy surface including the chips. As can be observed in the figure, the coolant flow is accelerated more among the pins under the module, indicating effective and rapid heat dissipation from the area towards the outlet. That means, the highly conducting graphene material helps the in-plane heat spreading and makes a uniform temperature profile over the module down to the coolant.



(a)



(b)

Figure 6.9: CHT computation in graphene-based heatsink (a) Streamlines in the fluid domain. (The triad colors red, yellow, and green in Cartesian coordinate correspond to axes directions x , y , z , respectively, and the scale bar shows the fluid velocity in m/s). (b) Top view of the xy surface including the chips highlighted feature edges in black.

The immediate impact of the graphene material is also reflected in the heat transfer coefficients for the heat transfer surfaces, as shown in Table 6.2, at a reference temperature of 338 K.

Table 6.2: Results of heat transfer to the surfaces of both the Al./Gr. heatsinks

Heat transfer to the surfaces of the heatsinks	Coolant flow rate (l/min)	Convective heat flux (W)		Wall temp. (K)		Twall-Tref. (K)		Convection heat transfer coefficient (HTC) (W/m ² .K)	
		Al.	Gr.	Al.	Gr.	Al.	Gr.	Al.	Gr.
Glycol to Al./Gr. heat exchange surface	1	279.86	284.01	345.7	345.54	7.7	7.54	1962.68	2034.4
	6	275.4	280.98	340.67	340.19	2.67	2.19	5572.5	6930.64

According to the CHT computation values given in Table 6.2, the heat transfer coefficient of the graphene heatsink shows an improvement of 3.65% for 1 l/min and a substantial value of 24.4% for 6 l/min compared to those of the aluminum counterpart. Moreover, the simulation with graphene indicates a decrease up to 3.7% for 1 l/min and 19.6% for 6 l/min in the calculated thermal resistance between the cooling plate and the coolant fluid, R_{th-sf} .

Figure 6.10, shows the average temperature of the chips for both the aluminum and graphene heatsinks calculated for 1 and 6 l/min coolant flow rates.

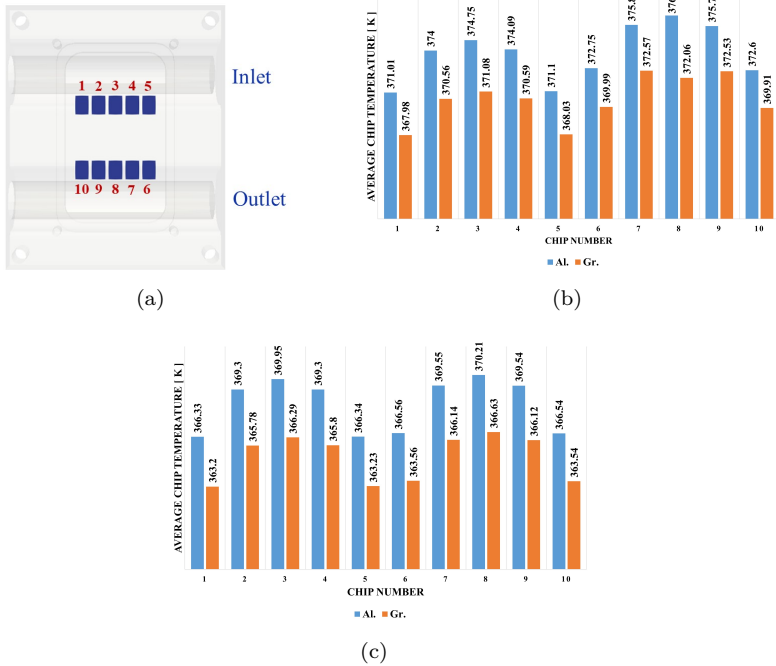


Figure 6.10: Chip numbers and average temperature of the chips in the aluminum and graphene heatsinks. (a) Chip numbers. (b) Aluminum vs graphene at 1 l/min fluid flow rate. (c) Aluminum vs graphene at 6 l/min fluid flow rate.

As illustrated in Figure 6.10, the average chip temperatures are lower with the graphene heat exchange unit compared to the aluminum unit for the same coolant flow rate. For example, considering chip number 8, with a thermal load of 34.5 W per chip and a 1 l/min fluid flow rate, the temperature rise relative to the 338 K reference fluid temperature is 38.5 K for the aluminum unit and 34.06 K for the graphene unit. This means the chip temperature in the graphene unit is reduced by 11.5% compared to the aluminum unit, relative to the cooling fluid.

However, the most significant contribution of the graphene insertion observed in this work is a substantial improvement in the speed of heat dissipation from the surface of the chips towards the fluid. Figure 6.11 presents how

the heat is absorbed from the chip level layers and rapidly distributed further to the liquid via the graphene fins compared to that of the aluminum ones.

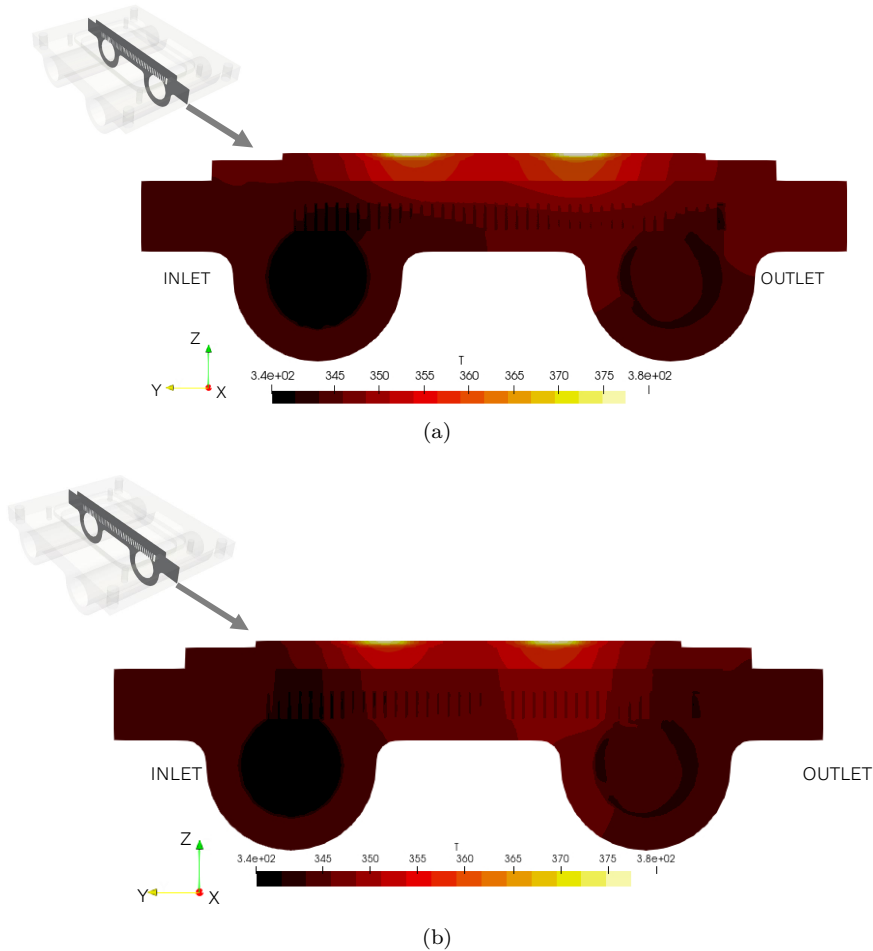


Figure 6.11: Steady-state temp. distribution in the heatsinks at 1 l/min.(a) Aluminum heatsink. (b) Graphene heatsink.

The observed improvements in the thermal performance of the graphene cooling device can be attributed to the high in-plane thermal conductivity and thermal diffusivity of graphene films (in the z-direction), which significantly

enhance heat conduction through the various material layers. Additionally, the heat is spread more uniformly over a larger volume in each layer (in the x-direction), ensuring that each layer absorbs heat evenly, resulting in a more uniform temperature profile for heat convection cooling. As a result, better heat spreading reduces thermal resistance, as more of the heatsink is effectively utilized for heat conduction. Consequently, the increased heat spreading speed and improved temperature uniformity enhance the overall heat dissipation capability.

6.3.4 Experimental validation of implemented CHT on the designed aluminum heatsink

Currently, the fabrication of the graphene-assembled films used in the proposed graphene heatsink design in this study is highly challenging for standard electronics labs. Therefore, to validate the operation of the proposed modeled heatsink, the available aluminum heatsink was used on a test bench that was described earlier in the Experimental setup (Section 3.2) in Chapter 3.

By selecting a 300 V inverter DC-Link voltage, 300 A current, and a 25 kHz switching frequency, a total power loss of 1400 W at the 180 Nm, 1500 rpm operating point of the machine emulator was applied to all three CAB450 SiC modules, resulting in 46.7 W loss per chip. Water at 13°C (286 K) with a flow rate of 6 l/min was used as the coolant. Figure 6.12 illustrates the DC-link voltage, three-phase currents, and instantaneous voltages used in the experiment.

To compare the experimental results vs. simulation, the CHT simulation has been run with the same boundary conditions as in the experiment.

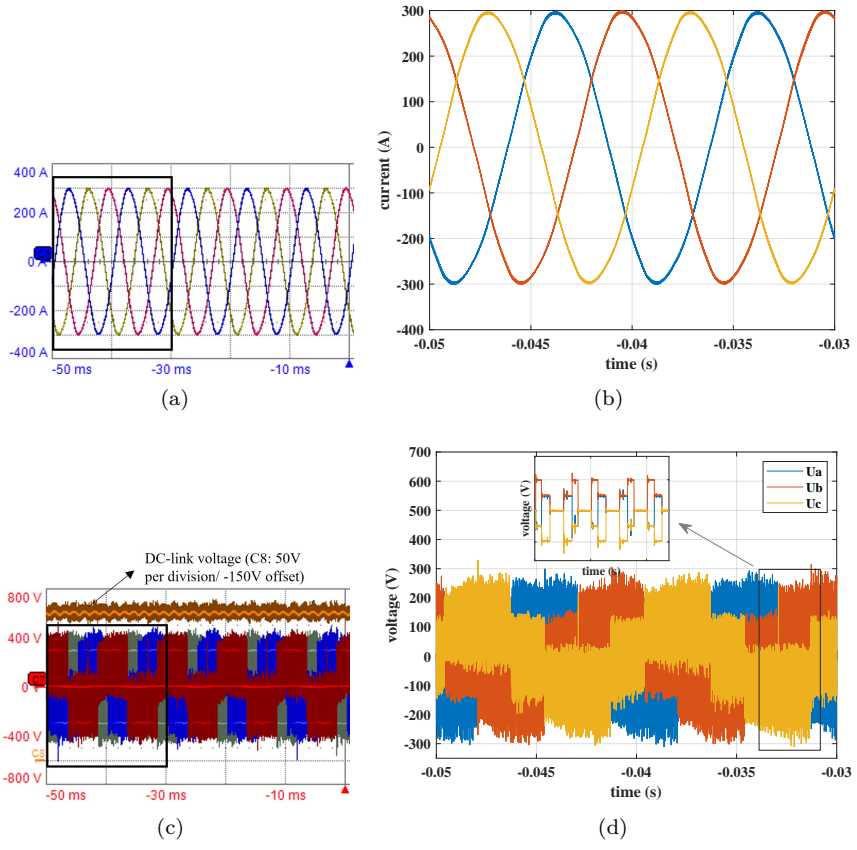


Figure 6.12: Selected boundary conditions in the experiment and simulation. (a) Three-phase currents. (b) A zoomed-in view of the currents. (c) DC-link and instantaneous voltages. (d) A zoomed-in view of the voltages.

Figure 6.13 depicts the experimental temperature profiles of the inlet and outlet. The temperatures were registered from the CHT simulation with probes located at the same locations as in the experiment.

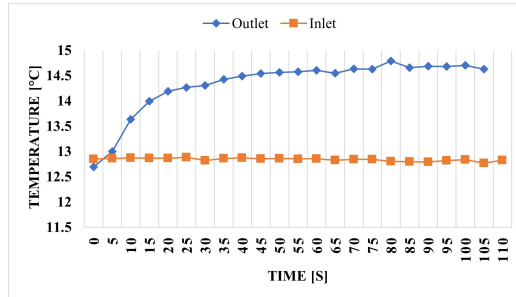


Figure 6.13: Experimentally observed temperature profiles of inlet and outlet.

As can be observed from Figure 6.13, the steady-state temperature of the outlet is about 14.6°C . This corresponds well to the value of 14.1°C obtained from the simulation for the corresponding probe location. Worth noting is that, in the experiment, the inner layers both in the power module and the designed heatsink are not easily accessible, making most of the valuable information obtained in the simulation hard to measure in the test setup through the sensors or the IR camera.

Following, the position of the other 4 sensors located on the surfaces of the heatsink and the respective temperature profiles are illustrated in Figs. 6.14 (a) and (b). According to Fig. 6.14 (b), the sensor temperature profiles are stabilized at a temperature close to 18.8°C , i.e., a temperature rise ΔT of about 6°C for the inlet temperature.

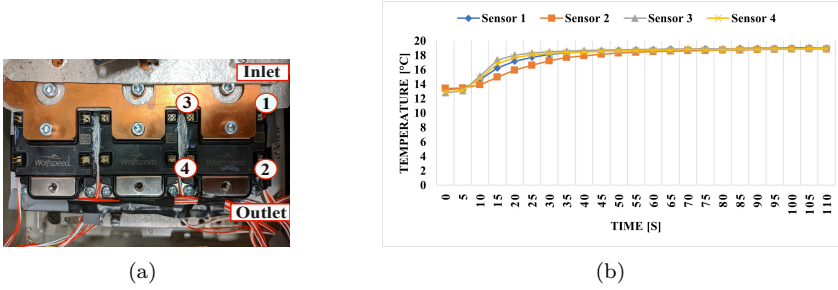


Figure 6.14: (a) PT-100 sensors located on the surfaces of the heatsink around the SiC power module. (b) Experimentally observed temperature profiles of the sensors.

The steady-state temperature rise obtained from both the experiment and the CHT simulation are given in Table. 6.3. As can be seen, the observed steady-state temperature rise in the experiment has a deviation of around 0.5°C / 10% from the corresponding values in the simulation, which is considered to be a good agreement. The given R_{dsON} in the semiconductors for 25°C has a span from a typical 2.6 mOhm to a maximum stated value of 3.7 mOhm, from the datasheet, in this work, the typical value was utilized. Furthermore, the contact, in particular, between the solder and other layers, is also uncertain.

Table 6.3: Steady-state temperature rise of the sensors from simulation and experiment

Steady-state temperature rise respect to the inlet/reference temperature				
	Sensor no.1 temperature rise ΔT_1 [$^{\circ}\text{C}$]	Sensor no.2 temperature rise ΔT_2 [$^{\circ}\text{C}$]	Sensor no.3 temperature rise ΔT_3 [$^{\circ}\text{C}$]	Sensor no.4 temperature rise ΔT_4 [$^{\circ}\text{C}$]
Simulation	5.23	5.09	5.49	5.43
Experiment	5.72	5.41	6.14	5.93
Diff. [$^{\circ}\text{C}$]	0.49	0.32	0.65	0.5
Diff. %	9.3	6.2	11.8	9.2

CHAPTER 7

Optimum DC-Link Voltage Determination for Electric Driveline

This chapter is based on the following articles (Paper G & H).

- I. Amirpour, S., Thiringer, T., and Xu, Y., "Mapping an Optimum DC-Link Voltage across the Entire SiC-Based EV Drive Regions accounting for a Synchronous Boost DC-DC Converter", Published SAE Technical Paper 2024-01-2218, 2024.
- II. S. Amirpour, T. Thiringer, S. Soltanipour and Y. Xu, "Optimal DC-Link Voltage Mapping for SiC-Based EV Drives: Considering the Impact of a Synchronous Boost Converter", Published in IEEE Access, vol. 13, pp. 38239-38254, 2025.

7.1 Overview

This chapter builds on the setups of Case setup 2 (Subsection 3.1.2), aiming to improve the powertrain efficiency by identifying an optimal DC-link voltage across the complete range of drive operating conditions utilizing a loss

minimization approach. The strategy adjusts the DC-link voltage to the various driving conditions to optimize the powertrain efficiency. This involves the inclusion of a DC-DC boost converter into the powertrain, placed between the battery and the traction inverter. For the analysis, a SiC power module (CAB450M12XM3) and a Si-IGBT module (FZ600R12KE3), as previously introduced, were used. Figure 7.1 illustrates an overview of the analysis.

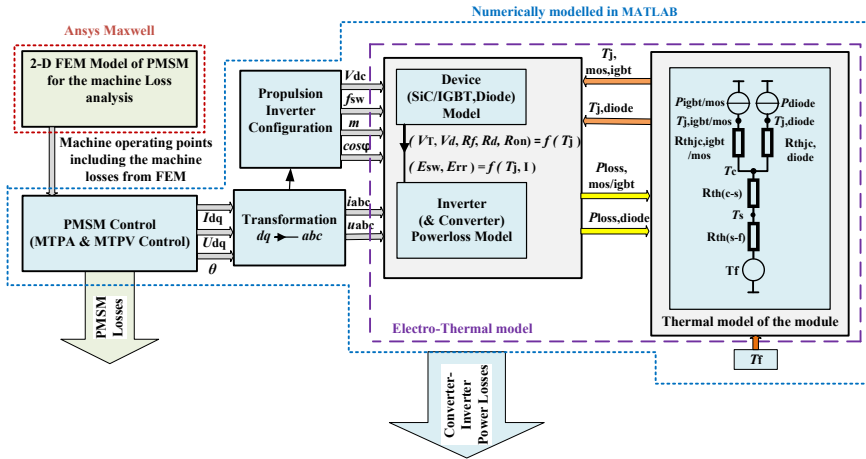


Figure 7.1: Analysis overview.

As shown in Figure 7.1, the analysis steps generally involve a comprehensive co-simulation framework implemented in this study using Ansys Electronic Desktop and MATLAB to accurately estimate powertrain losses. The FEA simulations focus on calculating key electromagnetic losses, including copper and core losses (encompassing hysteresis and eddy current losses). The d - and q -axis reference currents and voltages for the MTPA/MTPV control strategy were derived directly from the FEA analysis. This leads to a detailed mapping of key operating points across the machine's torque-speed region. These mapped points were then utilized in MATLAB, in the converter-inverter loss calculation model, incorporating the junction temperature feedback of the semiconductor devices. The analysis covers a range of supplied DC voltages, from 220 V to 450 V, which correspond to the lower and upper limits of the DC-link voltage.

7.2 Method

The main methodology of this study is the determination of the optimal DC-link voltage across the entire operational range of both the machine and the inverter.

Following the process outlined in Figure 7.2, total system losses (machine + inverter losses) were evaluated in a wide range of 220 V to 450 V DC for all operating points in the machine’s torque-speed map. The analysis then focused on identifying the minimum total losses at each operating point, assigning the corresponding DC-link voltage which led to the lowest loss for that operating point.

This approach effectively performs an offline optimization— an exhaustive (brute-force) search— generating a precomputed “optimal voltage vs. speed–torque” map that serves as a foundational reference for designing or evaluating control strategies that utilize dynamic DC-link voltage in EV powertrains.

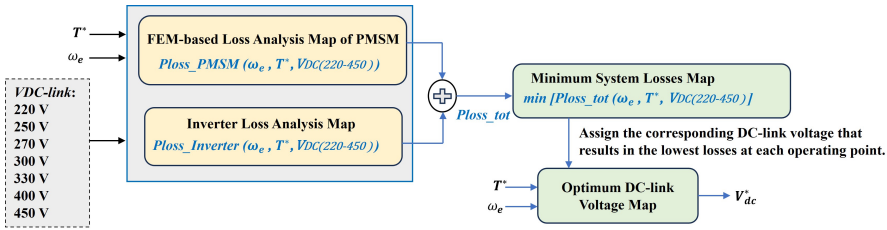


Figure 7.2: Steps to identify the optimal DC-link voltage over the entire range of the drive system.

Note that the co-simulation between Ansys Maxwell and MATLAB was essential to provide a FEM analysis of the machine losses alongside the numerical analysis of the inverter losses, (the process in Figure 7.1). This framework enabled the creation of comprehensive power loss maps and formed the foundation of the above methodology.

Accordingly, the power and energy losses of the DC-DC boost converter can be calculated based on the previously proposed adjusted DC-link profile. The calculation process is outlined in Figure 7.3. This analysis used 3-D look-up tables of losses for various battery voltage scenarios: 220 V, 250 V, 270 V, 300 V, and 330 V.

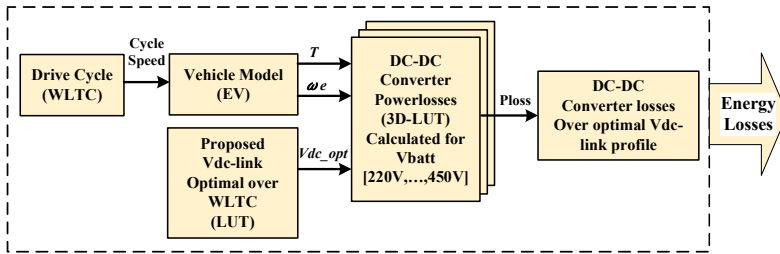
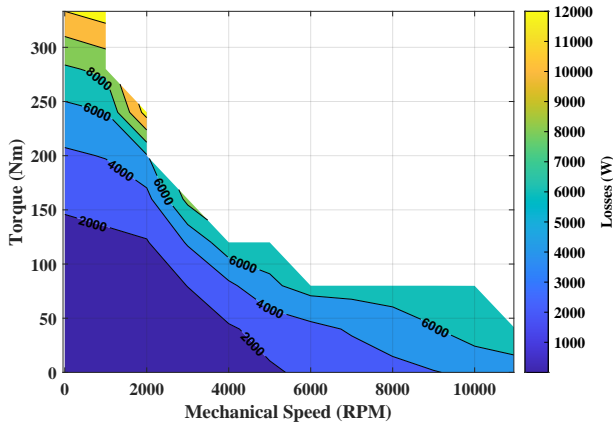


Figure 7.3: Power and energy loss calculation of DC-DC converter for the optimal DC-link voltage over WLTC for different battery voltage scenarios.

The complete analysis and the corresponding key results of this work will be presented in the following section.

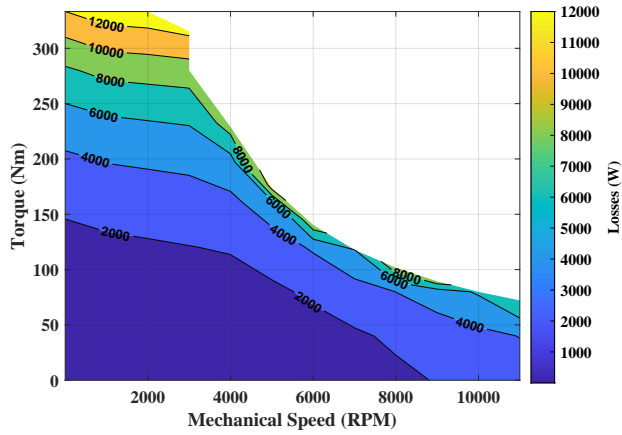
7.3 Key results and discussion

The initial phase of the analysis focused on calculating the total losses, which include both the machine and the inverter components, at the DC link voltage limits of 220 V and 450 V. The analysis is based on the drive parameters listed in Case setup 2. The results indicated that the machine exhibited greater differences in losses between the two DC-link voltage levels compared to the inverter. While the inverter showed only minor variations in losses. However, both the machine and inverter experienced lower losses at a DC-link voltage of 450 V, particularly in the field-weakening region. Accordingly, the total system losses (machine + inverter) for the two DC-link voltages, illustrated in Figure 7.4 and 7.5, indicate that the field-weakening region experiences lower losses with a 450 V DC-link compared to 220 V.



(a)

Figure 7.4: EV powertrain system total losses including machine and inverter at 220 V dc-bus voltage.



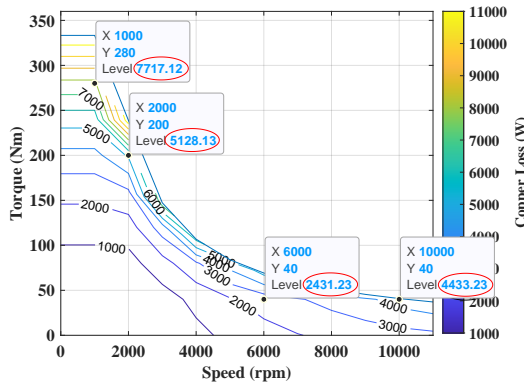
(a)

Figure 7.5: EV powertrain system total losses including machine and inverter at 450 V dc-bus voltage.

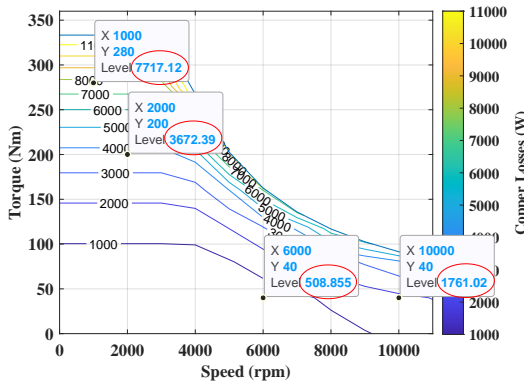
A detailed loss analysis revealed that copper losses account for a substantial portion of the total machine losses, particularly when compared to other calculated machine losses, in relation to the DC-link voltage. This observation is illustrated in Figure 7.6, highlighting four distinct operating points in the torque-speed map listed in Table 7.1. Note that, the copper losses shown in Figure 7.6, have been calculated at 220 V and 450 V DC-link voltage.

Table 7.1: Four selected operating points on the drive region.

OP. 1	OP. 2	OP. 3	OP. 4
1000	2000	6000	10000
rpm	rpm	rpm	rpm
280 Nm	200 Nm	40 Nm	40 Nm



(a)



(b)

Figure 7.6: Copper losses across the entire drive region with indicators for four operating points. (a) Copper losses at 220 V DC-link. (b) Copper losses at 450 V DC-link.

As illustrated in Figure 7.6, copper losses remain unaffected by the DC-link voltage at the first marked operating point in the low-speed, high-torque region (below base speed). However, as the speed increases—particularly in the mid-speed, low-torque region (OP.3—the third marked operating point)—the machine experiences notably higher copper losses, reaching up to 4.8 times higher with a low DC-link voltage compared to the higher DC-link one.

For the inverter, the loss analysis performed at the four selected operating points is shown in Figure 7.7.

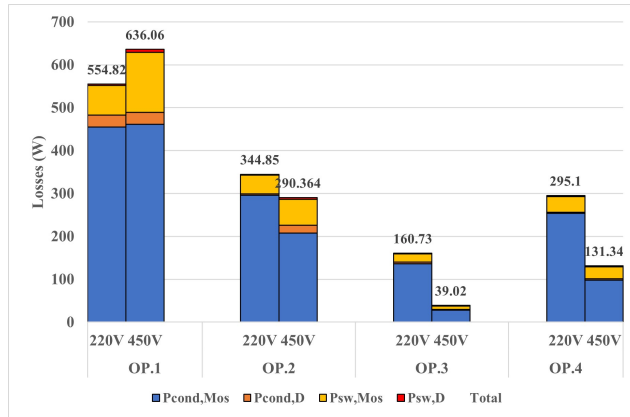
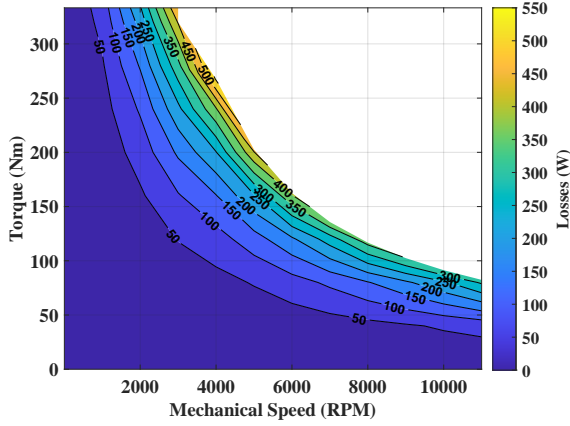


Figure 7.7: Conduction and switching losses of MOSFETs and diodes at four selected operating points, compared between DC-link voltages of 220V and 450V.

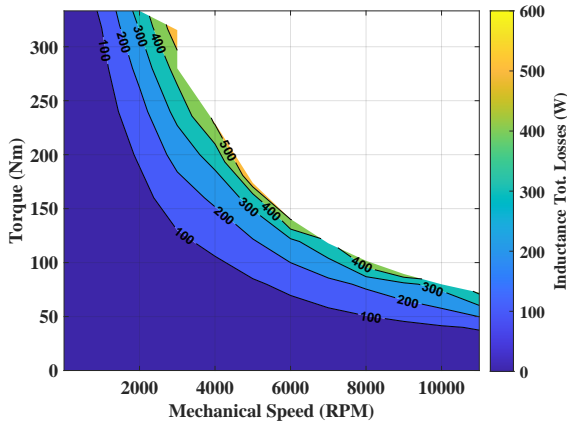
From the figure, it is clear that MOSFET conduction losses account for a significant portion of the total inverter losses. Similar to the machine's copper losses, changes in the DC-link voltage show that the third operating point, located in the high-speed, low-torque region, experiences higher losses with a lower DC-bus voltage. Furthermore, the MOSFET switching losses, which contribute secondarily to the total inverter losses, also exhibit a similar dependence on lower DC-link voltages, as they largely follow the current levels.

The results from the above-mentioned analysis led to the next phase: evaluating the potential benefits of integrating a DC-DC converter into the EV powertrain.

In this phase, a DC-DC boost converter, featuring one CAB450 SiC module and an inductor for full load condition (peak DC current), was implemented based on the theory and the design parameters presented in Chapter 2 and Case setup 2, respectively. The associated converter losses, including power electronics losses and inductor core and copper losses, were then incorporated into the overall system losses. Figure 7.8 shows the total losses of a SiC-based DC-DC converter, which boosts a 300 V battery to a 450 V DC-bus. This includes both the power electronics losses and the total inductance losses.



(a)



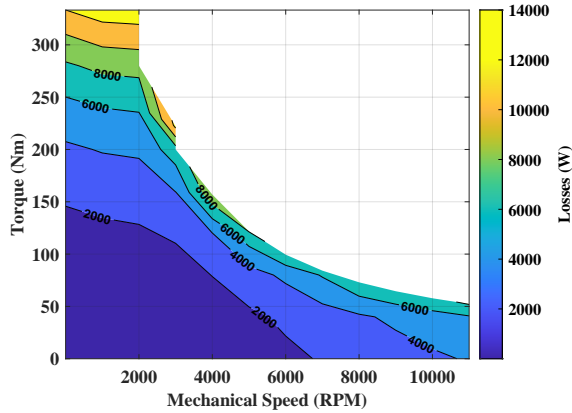
(b)

Figure 7.8: DC-DC boost converter total losses. (a) Power electronics losses in the SiC-based converter boosted from 300 V to 450 V DC-bus. (b) Inductance losses over the entire drive operating points.

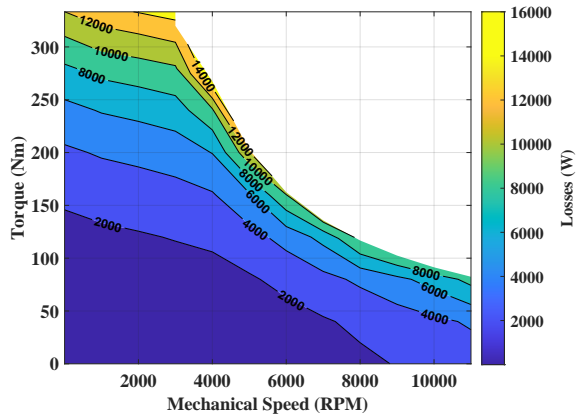
As Figure 7.8 shows, the inductance losses show slightly higher losses than the switches' total losses.

Subsequently, the total system losses were analyzed across all drive operat-

ing points of the studied machine, for both systems i.e., with and without the integration of the DC-DC converter. Figure 7.9 illustrates the system losses for boosting from a 300 V battery terminal to 450 V, both with and without integrating a DC-DC converter.



(a)



(b)

Figure 7.9: Total losses in the SiC-based system with and without the DC-DC converter. (a) Including inverter and machine at 300V DC-bus. (b) Including DC-DC, inverter, and machine boost from 300V battery terminal to 450V DC bus.

As can be observed from Figure 7.9, the powertrain system incorporating a DC-DC boost converter demonstrates lower total loss values, particularly in high-speed, low-torque regions. This differs from the scenario where the DC-DC converter is excluded. As illustrated in Figure 7.10, the loss difference between the two configurations can reach up to 5 kW. Interestingly, in the low-speed region below the base speed, the loss difference ranges from zero to negative values (see the contour bar), indicating that, under the design specifications of this study, incorporating the DC-DC converter to boost to 450 V does not enhance the drive system efficiency in this region.

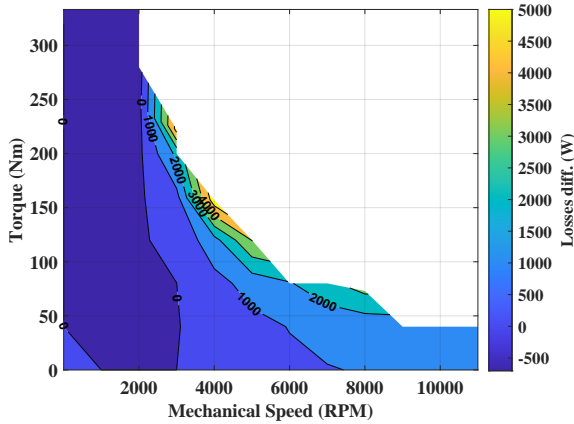
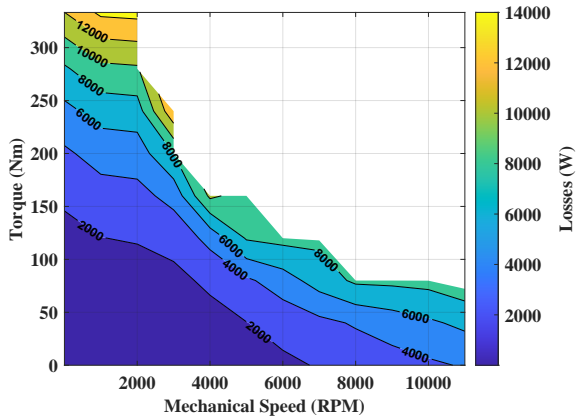


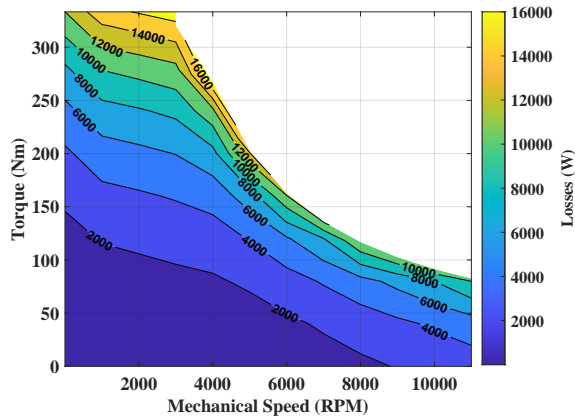
Figure 7.10: Differences in system losses with and without the DC-DC converter; figure(a)-figure(b) in Fig. 7.9.

This observation can be explained by considering the dependence of inverter switching losses on the DC-link voltage, particularly in the low-speed regions. Higher DC-link voltages lead to increased losses in this region. However, the use of SiC MOSFETs, which have much lower switching energy compared to IGBTs, contributes to this minimal loss difference in this region. If IGBT-based inverters are used instead, the difference in losses in this region (i.e., losses for 300 V DC-bus minus losses for 450 V DC-bus) would likely be greater, as shown in the next figure.

Figure 7.11 shows the IGBT-based system losses with/without a DC-DC converter for boosting from a 300 V battery terminal to 450 V DC-link voltage.



(a)



(b)

Figure 7.11: Total IGBT-based system losses. (a) Total losses including inverter and machine at 300V DC-bus. (b) Total losses including DC-DC, inverter, and machine boost from 300V battery terminal to 450V DC bus.

As expected, compared to the SiC-based system in Figure 7.9, the IGBT-based system experiences higher losses in both configurations: with a DC-DC converter at a 450V DC-link and without a DC-DC converter at a 300V

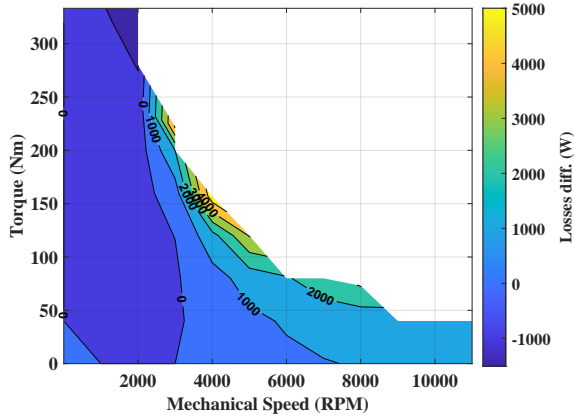
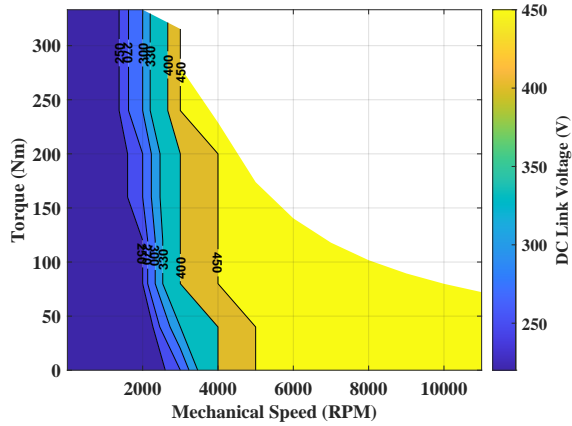


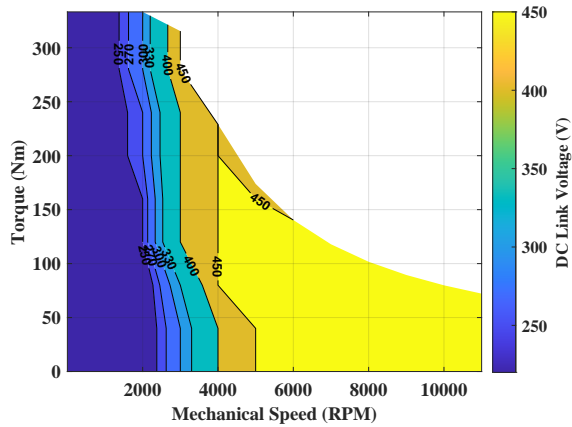
Figure 7.12: System loss differences with and without DC-DC converter; figure(a)-figure(b) in Fig. 7.11.

DC-link. However, Figure 7.12, which highlights the loss differences between configurations with and without the DC-DC converter in the IGBT system, shows a notable increase in the losses, in the low-speed, high-torque region marked by zero-values. It means that the IGBT system operating at a 300V DC-bus without the DC-DC converter has over 1 kW (see the contour bar) lower losses compared to 450 V boosted DC-bus, which is twice that observed in the SiC system under similar conditions. However, in the other drive regions, the IGBT system is comparable to that of its SiC counterpart, regarding the loss difference between including and not including the DC-DC converter.

Consequently, by using an adjustable DC-link voltage, based on the proposed optimal DC-link determination method in this study, (see Figure 7.2), the electric powertrain system can be optimized for improved efficiency. These voltage allocations aimed to achieve the lowest possible losses in each highlighted region, as depicted in Figure 7.13 and 7.14 for the machine along with both the SiC and IGBT-based inverters.



(a)



(b)

Figure 7.13: Optimum dc-bus voltages are assigned across the entire drive operating region. (a) Lowest loss Vdc-based regions for the machine. (b) Lowest loss Vdc-based regions for the SiC-based inverter.

As observed from Figure 7.13 and 7.14, for the components, particularly in the rated speed region, a 450 V DC-link voltage was found to be the optimal value for minimizing losses. While, in the low-speed region, a lower DC-link

voltage of 270 V resulted in the minimum losses for the components.

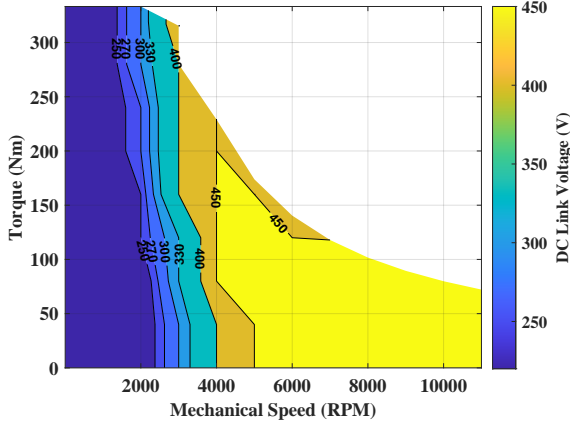


Figure 7.14: Optimum dc-bus voltages are assigned across the entire drive operating region; Lowest loss Vdc-based regions for the IGBT-based inverter.

A closer inspection of the figures reveals that, within the inverters, a 450 V DC-bus voltage is optimal for a slightly narrower region of the rated speed compared to the machine. For example, at a speed of 4000 RPM and a torque level above 200 Nm, even a 400 V DC-link voltage can result in minimum losses for the inverters. For the inverters' comparison, although a 450V DC-bus voltage is identified as the optimal value for the medium-to-high speed region in the IGBT-based inverter (similar to the SiC-based inverter), it covers a slightly smaller portion of this region.

Finally, the electric machine under study was incorporated into the powertrain of a medium-sized battery electric vehicle (BEV) and evaluated under the WLTC test drive cycle to analyze the accumulated energy losses. The dynamic parameters of the vehicle have already been presented in Chapter 3, Section 3.3. Three case studies are examined. In Case A, the powertrain system operates without a DC-DC converter, using a 300 V DC-bus (and battery) voltage. Case B incorporates the DC-DC converter, boosting the 300 V battery terminal voltage to a 450 V DC-link. Case C implements the proposed method in the current study, adjusting the DC-link voltage to an optimal level for the drive system. These case studies were conducted for both SiC- and

IGBT-based systems. Figure 7.15 shows the results of vehicle assessment in the WLTC drive cycle for Case A and B.

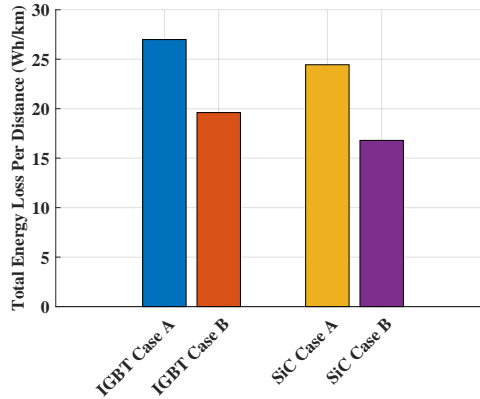
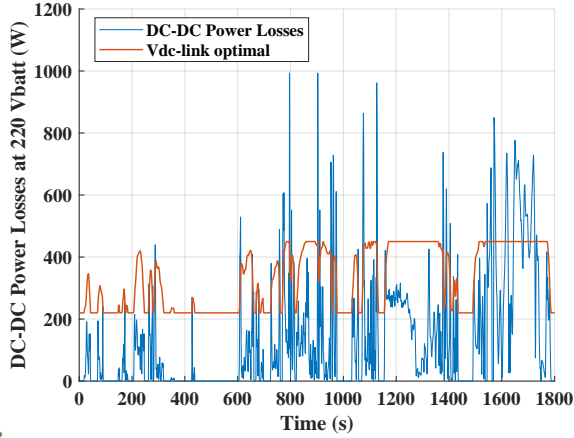


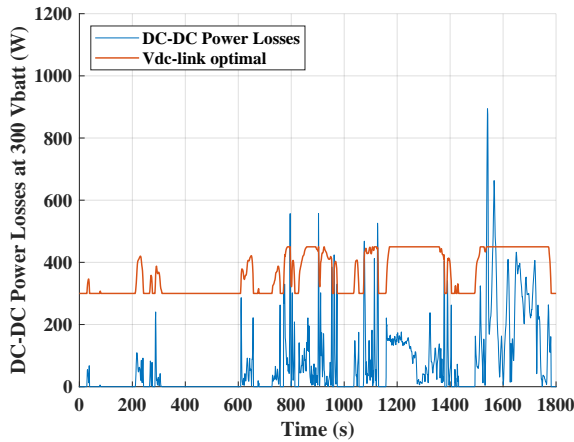
Figure 7.15: Accumulated energy loss per distance in a selected electric vehicle in WLTC test drive cycle. Case A (300 V DC-bus w/o DC-DC converter) and B (with DC-DC converter boosted from 300 V battery to 450 V DC-bus) for both IGBT and SiC-based systems.

As shown, the SiC-based drive consistently achieves lower energy losses than the IGBT-based system across all three cases. In Cases A (300 V DC-link without DC-DC converter) and B (boosted to 450 V DC-link with DC-DC converter), both IGBT and SiC systems demonstrate a significant reduction in accumulated energy losses at the higher DC-link voltage of 450 V, with a 27 % reduction for the IGBT system and a 31.7 % reduction for the SiC system over the WLTC drive pattern. This indicates that boosting to a higher DC-bus voltage benefits both IGBT- and SiC-based powertrains.

For Case C, first an analysis was performed to calculate the power and energy losses of the DC-DC boost converter when the proposed adjusted DC-link profile is applied to both SiC and IGBT-based powertrains across different battery voltage scenarios, see Figure 7.3. This analysis provides an estimate of how much the inclusion of the DC-DC converter contributes to the overall losses in the powertrain. Figure 7.16 illustrates the total power losses of the SiC DC-DC boost converter, considering the optimal DC-link profile for 220 V and 300 V battery terminal voltages.



(a)

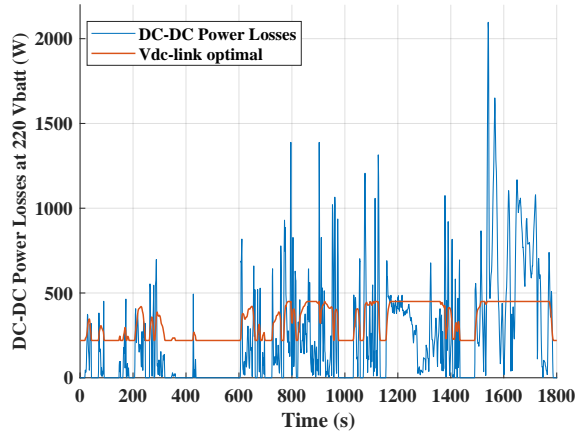


(b)

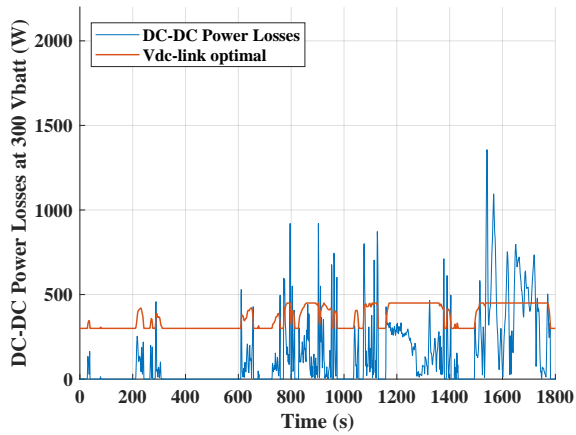
Figure 7.16: Total power losses of SiC DC-DC converter based on optimal DC-link voltage profile. (a) at 220 V battery terminal. (b) at 300 V battery terminal.

As shown, the DC-DC converter experiences higher power losses with the lower battery voltage of 220 V compared to the 300 V battery.

A similar calculation has been performed for an IGBT-based DC-DC converter. The results are shown in Figure 7.17.



(a)



(b)

Figure 7.17: Total power losses of IGBT DC-DC converter based on optimal DC-link voltage profile. (a) at 220 V battery terminal. (b) at 300 V battery terminal.

As shown in Figure 7.17, similar to the SiC-based DC-DC converter, lower power losses are observed with the higher battery voltage of 300 V for the IGBT-based converter. However, as expected, the IGBT-based converter exhibits higher total losses in both battery voltage scenarios compared to the SiC-based converter.

Consequently, the accumulated energy losses for both the SiC and IGBT DC-DC boost converters, using the proposed adjusted DC-link voltage profile, have been calculated for various battery voltage scenarios. The results are presented in Figure 7.18.

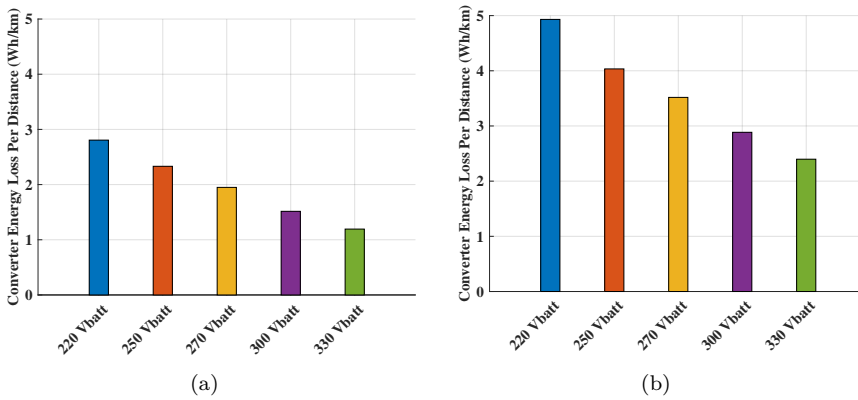


Figure 7.18: Total energy loss per distance in the DC-DC converter over the WLTC test drive cycle based on the adjusted optimal DC-link voltage for different Battery voltages. (a) SiC-based converter. (b) IGBT-based converter.

As shown in Figure 7.18, both the SiC and IGBT-based DC-DC boost converters exhibit lower energy losses at higher battery voltages over the optimal DC-link voltage profile. However, the IGBT-based converter consistently shows relatively higher energy losses compared to the SiC-based converter.

Finally, in Case C, the proposed adjusted DC-link voltage profile was applied to the entire driveline in both the IGBT and SiC systems to calculate the accumulated energy losses, as presented in Figure 7.19. Note that the average energy loss value of the DC-DC converter, derived from Figure 7.18, was used in Case C.

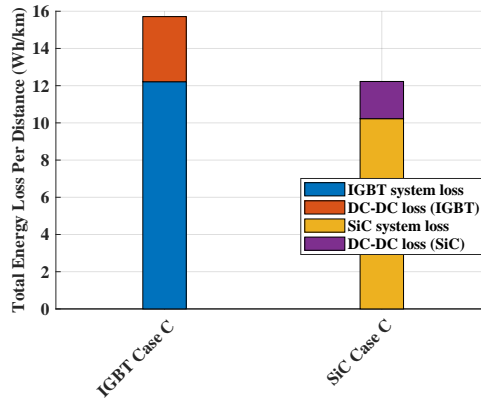


Figure 7.19: Accumulated energy loss per distance in a selected electric vehicle in WLTC test drive cycle. Case C uses the optimal DC-link voltage profile for both IGBT and SiC-based systems.

As shown in Figure 7.19, the accumulated energy losses in both the IGBT and SiC systems decrease by nearly half compared to when using fixed DC-link voltages of 300 V and the boosted 450 V (Case A and B) shown in Figure 7.15.

Additionally, in Case C, the SiC-based powertrain achieves a 22 % greater energy loss reduction compared to the IGBT counterpart when optimizing the DC-link voltage across all operating regions. Generally, an optimized, adjustable DC-link voltage enhances driveline efficiency in the IGBT- and SiC-based systems. However, the difference in energy loss between the SiC and IGBT systems is less notable with an adjustable DC link voltage. This is because the IGBT losses (especially switching losses) benefit more from the reduction in voltage (within the adjusted DC link voltage profile), while the SiC MOSFETs are already optimized for high-voltage operation since they inherently have lower losses, especially lower switching losses, compared to IGBTs, even at higher voltages. Unlike IGBTs, which suffer from exponential switching loss increase with voltage, SiC MOSFETs maintain efficient performance across a wide voltage range. Therefore, when the DC-link voltage is reduced, IGBT switching losses decrease considerably, whereas SiC MOSFETs, already operating efficiently, experience only marginal additional improvements.

CHAPTER 8

Optimum Switching Frequency Determination for Electric Driveline

This chapter is based on the following article (Paper I).

- I. Sepideh Amirpour, Sima Soltanipour, Torbjörn Thiringer, Pranav Katta, "Adaptive Determination of Optimum Switching Frequency in SiC-PWM-based Motor Drives: A Speed-Dependent Core Loss Correction Approach". Accepted for publication in the IEEE Open Journal of the Industrial Electronics Society, 2025.

It should be noted that Section 8.2.1 of this chapter is based on joint work with Sima Soltanipour, whose contributions to the analysis of core loss coefficient corrections based on speed and machine parametrization are fully acknowledged.

8.1 Overview

This chapter builds on the setups of Case setup 3 (Subsection 3.1.3), aiming to improve the powertrain efficiency by identifying an optimal switching

frequency for SiC-based motor drives across a wide range of operating conditions using a loss minimization strategy. The results are then compared with those of traditional Si-IGBT systems. This approach entails performing a detailed real-time FEM analysis to evaluate losses caused by PWM voltages in an Interior Permanent Magnet (IPM) synchronous machine, in comparison to sinusoidal current excitation, which is commonly used in e-machine analysis. The study integrates electromagnetic field simulations in Ansys Maxwell with the drive system control algorithm in Ansys Twin Builder, ensuring a precise representation of their interactions. Moreover, a method incorporating speed-adaptive core loss coefficients, which consider frequency variations, was implemented to enhance the accuracy of core loss estimation.

By applying speed-adaptive corrected core loss coefficients (discussed in the next section), key input data, such as machine reference currents, rotating speed, and dynamic inductances were generated and fed into the field-oriented control loop in Ansys Twin Builder to produce the required reference voltages for the SVPWM switching pattern of the SiC voltage source inverter. The resulting three-phase PWM currents and PWM-induced voltages excite the PMSM, generating PWM-induced losses in the machine. To ensure accurate inverter loss calculations, the measured currents and instantaneous voltages obtained from the real-time co-simulation between Twin Builder and Ansys Maxwell were then imported into MATLAB for numerical loss model implementation. For the analysis, a SiC power module (CAS300M17BM2) and a Si-IGBT module (FZ600R17KE3), as previously introduced in Case setup 3, were used. The analysis covers a range of PWM switching frequencies from 2.5 to 50 kHz.

This design topology serves as the foundation for the adjustments of the switching frequency across the entire drive region, as detailed in later sections.

8.2 Method

The main methodology in this study follows two steps: first, providing speed-adaptive core loss coefficients that are dynamically updated based on the specific supply frequencies at each operating point, as well as incorporating the effect of PWM on the core loss calculation. The second step involves the determination of the optimal switching frequency across the entire operational range of both the machine and the inverter.

8.2.1 Speed-dependent core loss calculation

The stator and rotor cores of the IPM under study are manufactured from silicon-iron steel laminates. The electromagnetic properties of these steel sheets are measured using standard methods, such as the Epstein Frame, as defined in IEC-60404 [115]. The key parameters for evaluating the performance of the electric machine, such as permeability (μ_r) and specific power loss (P_s), are measured at peak flux density (B_{pk}). The test setup is depicted in Figure 8.1.

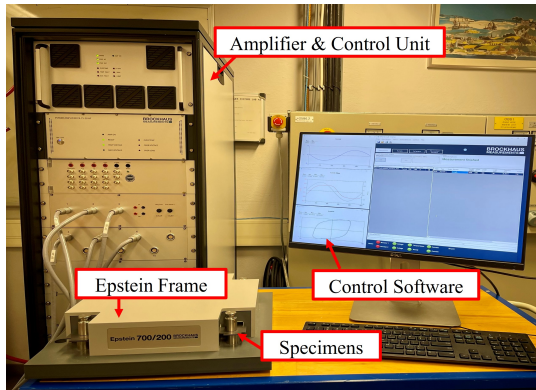


Figure 8.1: Test Setup for measuring the electrical - steel's properties.

The results show that as frequency increases, permeability decreases and specific core losses increase, Figures 8.2 and 8.3.

These properties are measured under sinusoidal excitation in a large number of frequency steps. In this way, a better representation can be made to

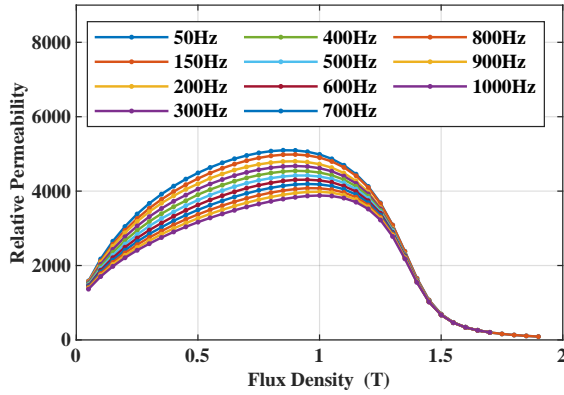


Figure 8.2: Relative permeability of the material under sinusoidal excitation with different frequencies.

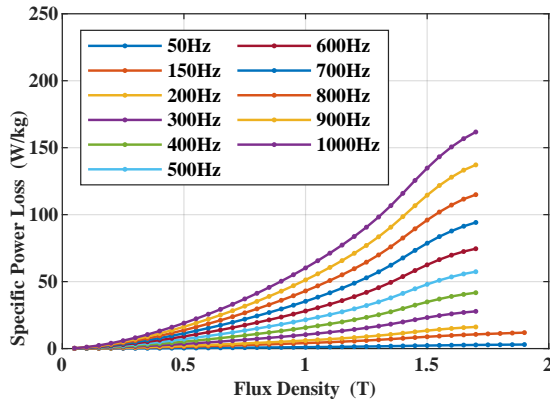


Figure 8.3: Specific Power Loss of the material under sinusoidal excitation with different frequencies.

determine the fundamental frequency iron loss for speed ranges across the wide operating region of a vehicle traction machine.

Iron loss models like the Bertotti model are widely used in FEM tools to predict the iron loss dependency on flux density and frequency. Conventionally, in FEM tools, an electric machine is characterized by running a

simulation with current excitation at a single speed, then extrapolating the results for other speed ranges to estimate the whole machine's performance across the torque-speed map. This method involves inputting multiple loss curve datasets measured at different frequencies into the FEM tool, which then applies curve fitting using the Bertotti model and minimizes the Root Mean Square Error (RMSE) to derive a single set of eddy and hysteresis loss coefficients. However, this process is highly sensitive to the choice of input frequencies, potentially leading to deviations from actual measured losses at varying frequencies.

To improve the accuracy of input data utilization, a frequency-dependent hysteresis coefficient can be introduced. In this study, an analysis of flux density distribution across the stator core cross-section and the frequency spectrum of individual stator elements reveals that different parts of the stator experience space harmonic content. This arises from the interaction between the stator slots and the rotor magnet shape. Furthermore, these space harmonics vary with the operating point, as the current angle influences the magnetic flux—determined by the interaction between the winding's electromagnetic flux and the magnetic flux generated by the magnets. Hence, to evaluate the importance of including these harmonics in the accurate calculation of core losses in the Bertotti model, the flux density distribution across the frequency spectrum was analyzed. This was done for all stator elements at 248 operating points in the torque-speed map of the IPM under study.

To simplify the study and evaluate the impact of each frequency on the core loss of the machine, the parameter Λ is introduced over a mesh element,

$$\Lambda = B_{pk,n}^2 \frac{f_n}{f_1} = \frac{P_h}{f_1 K_h} \quad (8.1)$$

where f_n is the space harmonic frequency, f_1 is the fundamental frequency at the operating point, P_h (equation 2.41) and K_h are the hysteresis loss and the hysteresis loss coefficient, respectively. This parameter shows the value of hysteresis loss for each element divided by the hysteresis coefficient. Figure 8.4 shows the distribution of Λ for the EM under study.

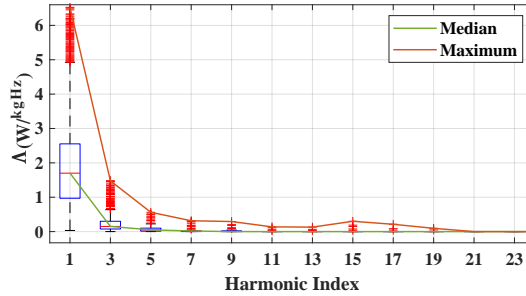


Figure 8.4: Distribution of Λ for each mesh element over the stator core at operating points throughout the speed-torque map of the IPM.

As can be seen, the median of Λ at the fundamental frequency, $1.7 \frac{W}{kgHz}$, is more than 11 times the third space harmonic content. Another observation is that 50% of the data are in the range of $0.9 \frac{W}{kgHz}$ to $2.55 \frac{W}{kgHz}$ in contrast to the third harmonic content which is in the range of $0.075 \frac{W}{kgHz}$ to $0.3 \frac{W}{kgHz}$. For the higher harmonic orders, the ratio between the median of the fundamental and the fifth-order harmonic is 34. According to this observation, it is safe to assume that the biggest portion of the core losses are generated by the flux densities appearing at the fundamental frequency. To account for the dependency of the hysteresis loss coefficient, the electric machine is characterized once again by simulation at each frequency level with the frequency-adaptive hysteresis loss coefficient replacing the conventional fixed coefficient. Figure 8.5 summarizes the steps defined to improve the core loss calculation.

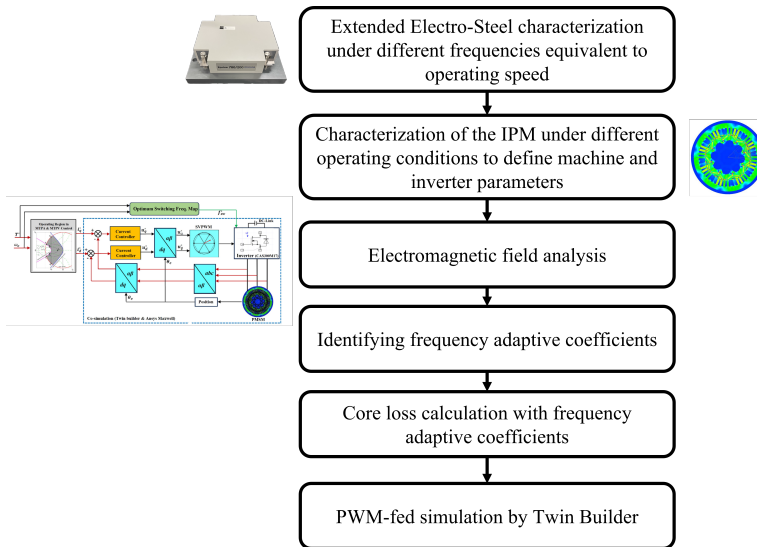


Figure 8.5: Simulation steps regarding the method to improve core loss calculation.

The proposed frequency-adaptive coefficient method improves loss estimation accuracy by emphasizing precise calculation of the fundamental frequency, which dominates iron losses at a given operating point. In contrast, the conventional approach prioritizes minimizing errors at high frequencies, often compromising accuracy at lower and medium frequencies.

8.2.2 Optimum switching frequency determination

Following the procedure depicted in Figure 8.6, total system losses (machine + inverter losses) were evaluated over a frequency range of 2.5 to 50 kHz for all operating points in the machine's torque-speed map. The analysis was carried out as an offline optimization method (as explained in the previous chapter), which identified the optimal PWM switching frequency by determining the frequency that resulted in the lowest total losses at each operating point and assigning it to that point, accordingly.

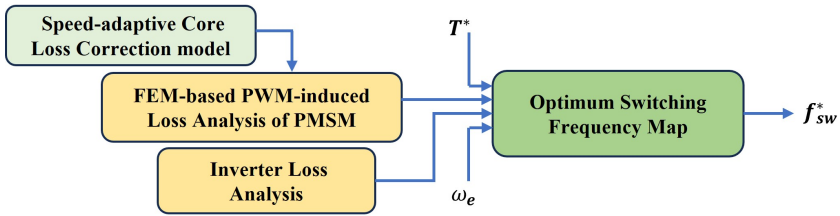
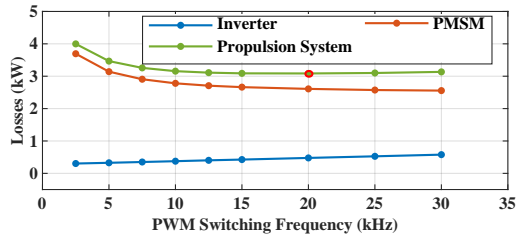
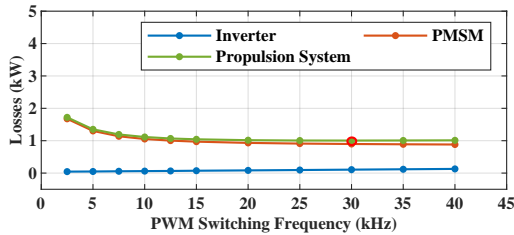


Figure 8.6: Steps to identify the optimal switching frequency over the entire range of the drive system.

An example of two tested operating points in this study—2000 rpm, 240 Nm, and 4000 rpm, 80 Nm—is illustrated in Figure 8.7. The figure depicts the trend of total losses in the drive system, encompassing both the PMSM and the SiC-based inverter, across a switching frequency range of 2.5 to 55 kHz.



(a)



(b)

Figure 8.7: Optimum PWM switching frequency determination in a total system loss minimization approach for two selected machine conditions. (a) at 2000 rpm, 240 Nm. (b) at 4000 rpm, 80 Nm.

As shown in Figure 8.7, as the PWM switching frequency increases, the decline in PMSM losses gradually diminishes, while the inverter losses rise linearly. At a certain switching frequency, these opposing trends balance each other out, resulting in minimum total losses for the drive system. For the example operating points, these optimal frequencies are identified at 20 kHz and 30 kHz, as shown by the red circles. This approach has been utilized to determine the optimal switching frequency across all operating regions of the drive system.

Notably, as previously mentioned, the comprehensive coupled time-stepping FEM analysis, which integrates both PMSM and inverter losses in real-time simulation, effectively captured their interaction across different PWM switching frequencies. This approach enabled the creation of detailed power loss maps and provided the foundation for this methodology.

8.3 Key results and discussion

As previously discussed, this study primarily focuses on optimizing system-level loss analysis to determine the optimal PWM switching frequency across all drive regions. This section presents the key results of the proposed PWM-induced power loss analysis for the IPM and the SiC-based inverter at two selected operating points, highlighting the impact of different PWM frequencies. Furthermore, this approach will be extended to all feasible operating points within the torque-speed region of the studied machine, enabling the development of an optimal switching frequency map through a drive system loss minimization strategy.

Conducting the co-simulation process, the generated PWM-induced current ripples injected into the PMSM have been analyzed for two selected machine operating conditions: one heavy-load, low-speed, and one light-load, medium-speed scenario from the drive region. The testing covered a range of PWM switching frequencies from 2.5 to 20 kHz.

Figure 8.8 illustrate the PWM-induced current ripples vs. switching frequency for the PMSM used, operating at 2000 rpm and 4000 rpm, generating electromagnetic torques of 240 Nm and 80 Nm, respectively.

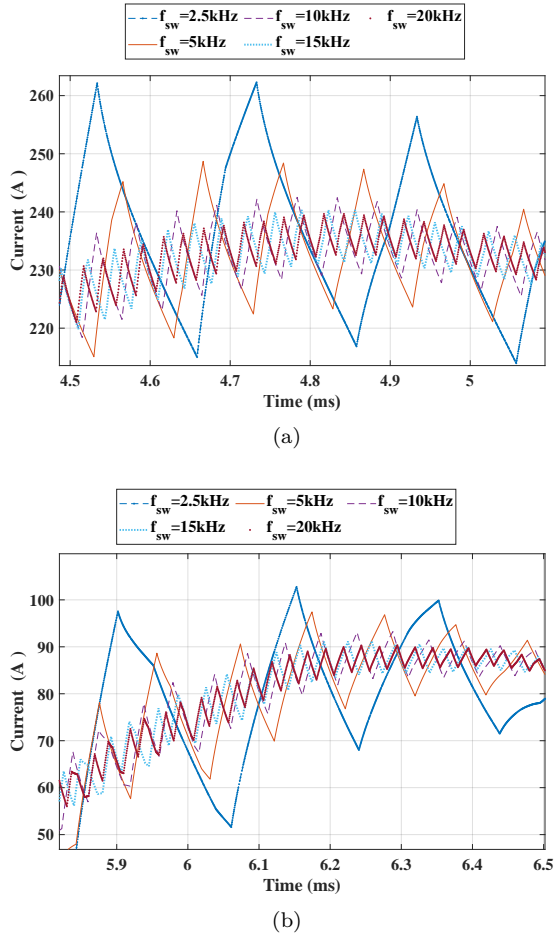


Figure 8.8: PWM-induced current ripples versus switching frequency for the PMSM, operating at heavy and light-load conditions. (a) at 2000 rpm, 240 Nm. (b) at 4000 rpm, 80 Nm.

Note that, increasing the switching frequency reduces the current ripple magnitude and corresponding harmonic content in the motor's three-phase current waveforms.

The current ripple amplitude values are displayed in Figure 8.9, showing that the ripple amplitudes for both conditions decrease monotonically as the

PWM frequencies increase. However, the difference in ripple magnitude diminishes for PWM frequencies above 12.5 kHz.

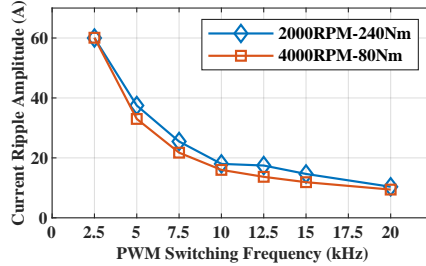


Figure 8.9: PWM-induced current ripple amplitude versus PWM switching frequencies for two selected machine conditions.

The results of the Fourier analysis that include the low-frequency and switching-frequency components are shown in Figure 8.10, and 8.11.

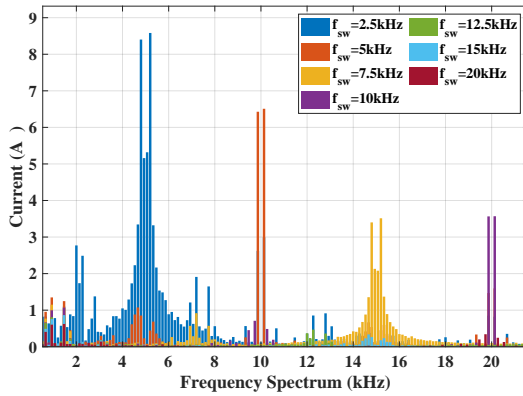


Figure 8.10: Fourier analysis of PWM-induced current ripples versus switching frequency for PMSM, operating at heavy-load condition, at 2000 rpm, 240 Nm.

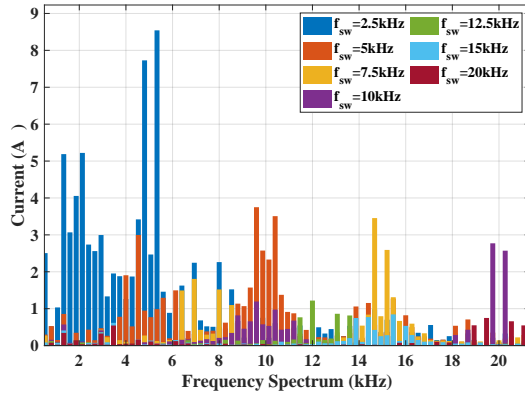


Figure 8.11: Fourier analysis of PWM-induced current ripples versus switching frequency for PMSM, operating at light-load condition, at 4000 rpm, 80 Nm.

As observed in the figures, in both the selected machine operating points, the dominant harmonics are concentrated around twice the PWM switching frequency. For instance, a switching frequency of 2.5 kHz results in a current ripple of 5 kHz, attributed to the SVPWM switching method, which generates a balanced set of switching patterns that effectively creates harmonic components at integer multiples of the switching frequency. The values of the harmonic components decrease as the PWM switching frequency increases.

To determine the impact of varying PWM switching frequencies on the machine and inverter losses, three operating conditions of the studied machine were evaluated. Figure 8.12 presents the PWM-induced losses in the machine across a wide range of PWM switching frequencies (5-30 kHz) along with the machine losses when using the sinusoidal feeding.

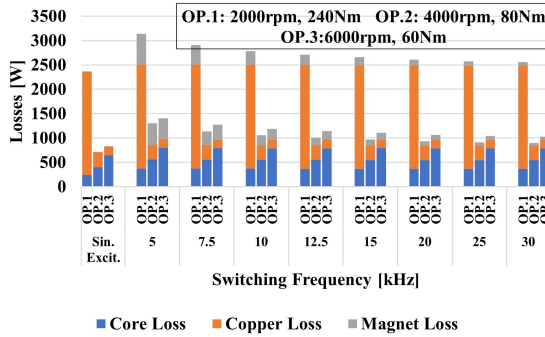


Figure 8.12: PWM-induced power losses in the machine versus PWM switching frequencies for three selected machine conditions.

As shown in Figure 8.12, across the selected machine conditions, varying the switching frequency noticeably impacts magnet losses, with a decrease in magnet loss as the PWM frequency increases. However, the reduction in core and copper losses is minimal. Higher PWM switching frequencies generate high-frequency harmonics, but these harmonics become less effective at inducing eddy currents in the magnets. As a result, less energy is lost in the form of magnet losses at higher PWM frequencies. The same high-frequency harmonics that reduce magnet losses do not have as much of an effect on core and copper losses. For the copper losses, although higher PWM frequencies can reduce current ripple, the impact on copper losses is relatively small because these losses are predominantly determined by the RMS value of the current rather than the ripple, especially for round-wire machines.

Comparing the sinusoidal excitation loss bars with PWM in Figure 8.12, PWM excitation leads to significantly higher magnet losses due to increased eddy currents from the switching harmonics. In contrast, sinusoidal excitation typically results in smoother loss behavior with fewer high-frequency components.

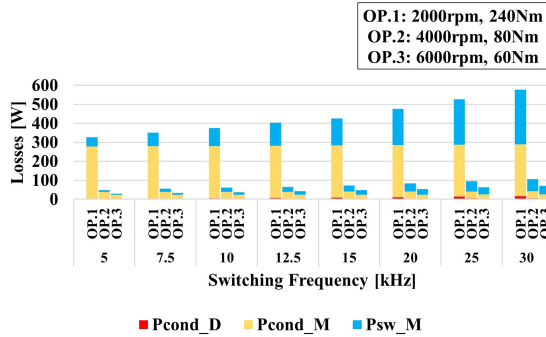


Figure 8.13: PWM-induced power losses in SiC-based inverter versus PWM switching frequencies for three selected machine conditions.

Figure 8.13 illustrates the distribution of SiC-based inverter losses as the PWM switching frequency increases from 5 to 30 kHz. As expected, increasing the PWM switching frequency substantially increases the MOSFET switching losses across all three investigated points, particularly under heavy-load conditions. In contrast, the impact on the MOSFET conduction losses is minimal. Additionally, the diode conduction losses observed under the selected operating conditions are negligible, although they slightly increase with higher switching frequencies. This increase is linked to more current flowing through the diodes as the junction temperature rises with elevated switching frequencies [8], [116]. Additionally, more switching occasions occur when current flows through the diodes. Note that, from the datasheet, the diode switching energy for the employed SiC module is zero.

Finally, by applying the previously discussed loss calculation methods at various operating points in the SiC- and IGBT-based drive regions under different switching frequencies, the optimal switching frequency scheme can be visualized in the drive system's torque-speed map; see the following figures.

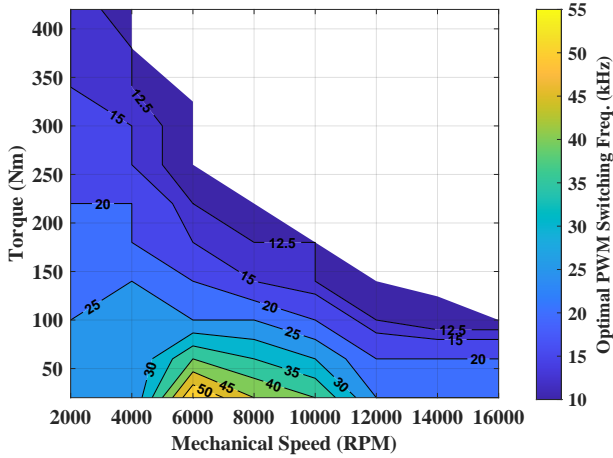
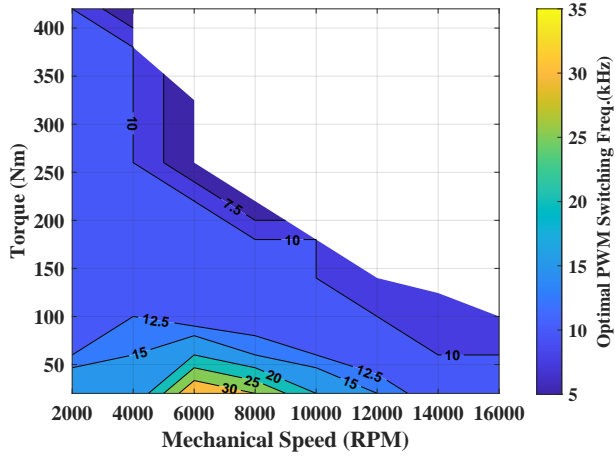


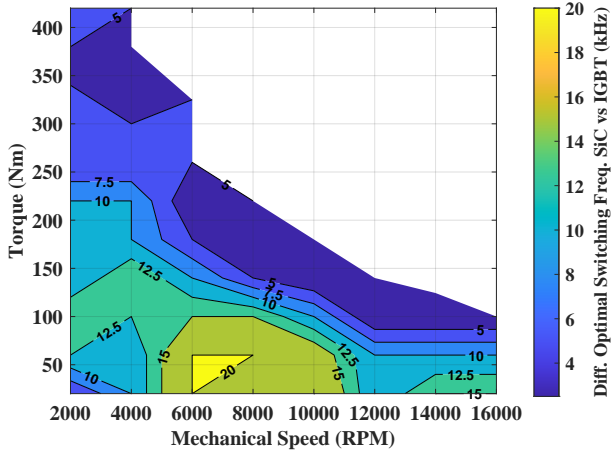
Figure 8.14: Optimal PWM switching frequency scheme of SiC-based motor drive system.

As can be observed from Figure 8.14, the optimal switching frequency is distributed in a pattern of concentric levels. As the value of the switching frequency decreases, it becomes associated with the outer layers of this pattern. In other words, higher frequencies are associated with the inner layers within the medium-speed range between 5000-10000 rpm with low torque, and lower frequencies are found in the outer layers for high torque regions. Additionally, in the high-speed region, the optimal switching frequency value gradually decreases as the speed increases.

Following, the approach used for the SiC-based drive system to determine the optimal switching frequency, the method was applied to identical operating points across the IGBT-based drive regions under different PWM switching frequencies. Figure 8.15 shows the distribution of the optimal switching frequency on the torque-speed map for the Si-IGBT-based drive system to achieve the minimum possible system losses, while Figure 8.15(b) illustrates the difference in optimal switching frequency between the two motor drive systems.



(a)



(b)

Figure 8.15: (a) Optimal PWM switching frequency scheme of IGBT-based motor drive system. (b) The difference in optimal switching frequency values between SiC-based and IGBT-based motor drives.

As shown, in the IGBT drive system, the typical PWM switching frequency range is limited to 5 to 30 kHz. In contrast, the SiC-based drive system

exhibits a broader PWM frequency distribution i.e., 10–50 kHz, due to its ability to operate at higher switching frequencies with lower switching losses compared to the Si-IGBT system. Additionally, as shown in Figure 8.15(b), the most significant difference—up to 20 kHz—occurs in the low- to medium-speed range with low torque, where EVs predominantly operate. Across other drive regions in the figure, the optimal frequency difference between the two motor drive systems is still substantial. These patterns illustrated above can indicate how the optimal switching frequency varies with different drive conditions or operational parameters, potentially guiding the selection of switching frequencies to minimize the losses and improve the motor drive performance.

Further evaluations were performed on the studied electric machine, integrated into the powertrain of a medium-sized battery electric vehicle (BEV). The vehicle was operated under the WLTC test-drive cycle to assess the predicted accumulated energy loss. The dynamic parameters of the vehicle were detailed in Chapter 3, Section 3.3. Three case studies are investigated. In Case A, the electric machine is sinusoidally fed in an FEM simulation with an inverter operating at a fixed switching frequency of 10 kHz. Case B examines a PWM-fed machine driven by an inverter with a fixed 10 kHz switching frequency in a coupled FEM simulation of the PMSM and inverter. Case C implements the proposed method in the current study, using a variable PWM-fed machine in the coupled FEM analysis. These studies were conducted for both a SiC-based inverter and an IGBT counterpart. Figure 8.16 shows the results of vehicle assessment in the WLTC drive cycle.

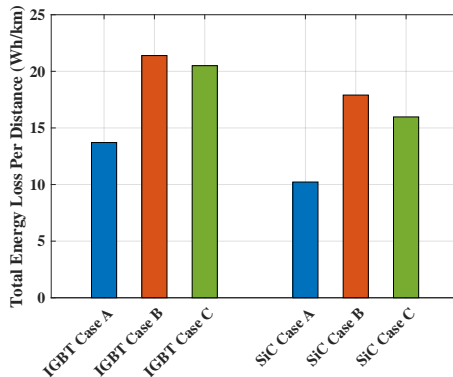


Figure 8.16: Total energy loss per distance in a selected EV over the WLTC.

As shown in Figure 8.16, in all three cases, the SiC-based drive consistently minimizes energy losses compared to the IGBT-based system. The sinusoidal current excitation of the machine (Case A) for both SiC and IGBT drives notably underestimates power and energy losses in the system. Looking at the bar charts for Cases B and C (IGBT & SiC), the proposed optimal PWM frequency profile (Case C) results in a 10.78 % reduction in accumulated energy loss for the SiC-based inverter and a 4.17 % reduction for the IGBT-based inverter compared to the fixed PWM frequency (Case B). Additionally, implementing the proposed method (Case C) leads to 22 % lower energy losses in the SiC-based drive compared to the IGBT counterpart, as the optimal PWM switching frequency pattern over the WLTC cycle is illustrated in Figure 8.17.

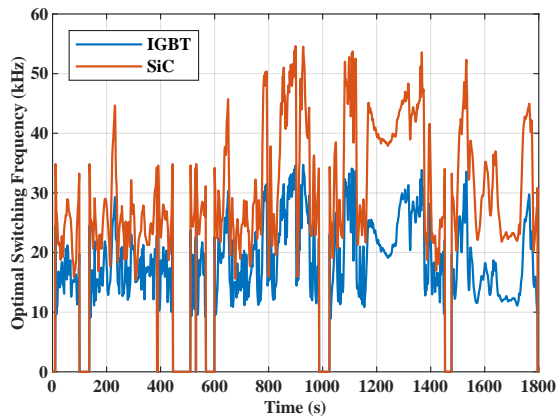


Figure 8.17: Optimal PWM switching frequency for IGBT and SiC switches under driving conditions of WLTC test-drive cycle.

It can be seen from the figure, the major difference, reaching up to 20 kHz, in the optimal frequency patterns occurs in the low- to medium-speed ranges over the WLTC, as also observed in the previous results.

Concluding Remarks and Future Work

9.1 Conclusions

This thesis began by numerically quantifying the impact of thermal feedback on power and energy losses in SiC versus IGBT devices—from the device level to the system level that was subsequently extended to real-world drive cycles (urban, highway, and mixed) as well as to mission-based lifetime predictions. It was shown that neglecting thermal feedback resulted in an underestimation of conduction losses by 11–15% in SiC inverters and by up to 18% in switching losses of IGBT inverters at a high-torque, low-speed operating point of the studied PMSM. Furthermore, energy losses in SiC inverters were found to be up to four times lower across the drive cycles, attributable in part to MOSFET reverse conduction, which makes them a superior solution at high switching frequencies even under worst-case conditions. Lifetime predictions further revealed that although the WLTC drive cycle induced considerably more accumulated damage than the ECE-City cycle—particularly affecting SiC devices—SiC modules were shown to achieve substantially longer lifetimes compared to IGBT systems.

Acknowledging heat as a key stress contributor, particularly in SiC MOS-

FETs, high thermal conductivity heat-spreading materials like graphene was proposed as an innovative solution for both SiC power module packaging and cooling devices/heatsinks. A detailed fluid dynamics model, utilizing a 3-D conjugate heat transfer (CHT) methodology, was employed to assess the thermal behavior of the emulated SiC power switches in contact with the coolant. The multidisciplinary analysis utilizing the graphene layer in the SiC module demonstrated a 10°C reduction per SiC chip in the junction temperature of the SiC MOSFET, based on an applied power loss per SiC chip in steady-state simulations. Additionally, a 15°C decrease was observed in transient computations over the WLTC per SiC chip. The integration of graphene in the heatsink design yielded significant improvements, including a 24.4% increase in the heat transfer coefficient (HTC) and a 19.6% reduction in thermal resistance (sink to fluid) at a 6 l/min fluid flow rate, compared to its aluminum counterpart. Consequently, the graphene-based heatsink resulted in an 11.5% lower temperature rise in the SiC chips compared to the aluminum version.

To address battery voltage fluctuations, adjusting the DC-link voltage across various driving conditions was proposed and investigated through a detailed loss analysis, incorporating FEM-based PMSM loss modeling and numerical power electronics loss calculations. The findings indicated that integrating a DC-DC converter into the powertrain and optimizing the DC-link voltage is particularly beneficial for low battery terminal voltages. Additionally, applying the proposed optimal DC-link profile in the WLTC drive pattern resulted in up to a 16% reduction in accumulated energy losses in the SiC driveline compared to its IGBT counterpart. Furthermore, the optimized DC-link profile reduced energy losses by 58% in the SiC-based system and 54% in the IGBT-based system, compared to operating at a fixed 300 V DC-bus voltage.

Furthermore, for improving the overall efficiency of the motor drive systems (SiC and Si), an optimal switching frequency across a wide range of operating conditions was determined. The analysis combined electromagnetic field simulations in Ansys Maxwell with a PWM-based drive system control algorithm in Ansys Twin Builder, ensuring an accurate representation of their interactions. By employing the real-time coupled simulations, the higher switching capabilities of SiC MOSFETs were effectively realized to optimize the PWM frequency over a broader range (10-50 kHz), particularly in the main drive region of electric vehicles, with differences of up to 20 kHz compared to IGBT systems. Furthermore, applying the proposed optimal PWM frequency profile

over the WLTC led to a reduction of up to 22% in accumulated energy losses in the SiC motor drive compared to its IGBT counterpart. In addition, the proposed optimal PWM frequency profile resulted in up to 11% reduction in accumulated energy loss for the SiC-based inverter and a 4.2% reduction for the IGBT-based inverter compared to using a fixed PWM frequency of 10 kHz.

9.2 Future work

As the efficiency analysis and improvements using SiC vs. Si were conducted for only a single propulsion inverter topology (2-level, 3-phase VSI) in the driveline configuration of this thesis, investigating other topologies, such as multi-level and neutral point clamped (NPC) inverters, would be highly valuable to highlight their potential benefits and drawbacks in EV applications.

In the context of lifetime studies, mission-profile-based SiC lifetime prediction models are still underdeveloped compared to IGBT models. Most studies focus on general reliability tests, not EV-specific lifetime evaluations under real-world mission profiles (i.e., real-world drive cycles). A standardized SiC lifetime model for automotive applications is still missing, making this an active area of research.

Incorporating graphene as a conductive heat spreader in power electronics would undoubtedly involve the construction of graphene-equipped cooling systems, requiring solutions for manufacturing challenges. This includes developing a method to experimentally integrate graphene layers in the power module packaging and/or graphene fins into a copper/aluminum cold plate within the heatsink. Although graphene functionalization on metal surfaces has been studied in the literature, further experimental validation is needed. Additionally, an environmental assessment is also crucial to ensure that energy savings justify the use of graphene in terms of overall sustainability. Equally important is further theoretical investigation to substantiate the benefits of graphene in heatsinks and power electronics packaging.

When it comes to the optimal adjustment of DC-link voltages and PWM switching frequency over the electric drive range, considering the impact of high switching speed (high slew rate dv/dt) in WBG-based motor drives on inverter losses is recommended. Providing a trade-off between the turn-off voltage overshoot caused by high dv/dt and the resulting switching losses,

along with assessing the effect of electromagnetic interference (EMI) in the system, is highly encouraged. Furthermore, a real-time optimization and control algorithm would be a valuable next step to select the voltage and the PWM frequency set-point over the driving region. To enhance the accuracy of core loss prediction in the electric machine, the impact of manufacturing processes on the electro-steel has also been recognized as an area for future work.

References

- [1] International Council on Clean Transportation, “Co₂ emissions (g/km) normalized to the nedc test cycle over time for the eu and selected global regions,” Accessed 2025-02-07. Available at <https://theicct.org/>.
- [2] European Commission, “Co₂ emission performance standards for cars and vans,” Accessed 2025-02-07. Available at https://climate.ec.europa.eu/eu-action/transport/road-transport-reducing-co2-emissions-vehicles/co2-emission-performance-standards-cars-and-vans_en.
- [3] J. Reimers, L. Dorn-Gomba, C. Mak, and A. Emadi, “Automotive traction inverters: Current status and future trends,” *IEEE Transactions on Vehicular Technology*, vol. 68, no. 4, pp. 3337–3350, 2019.
- [4] K. Kumar, M. Bertoluzzo, and G. Buja, “Impact of sic mosfet traction inverters on compact-class electric car range,” in *2014 IEEE International Conference on Power Electronics, Drives and Energy Systems (PEDES)*, 2014, pp. 1–6.
- [5] J. Biela, M. Schweizer, S. Waffler, and J. W. Kolar, “Sic versus si—evaluation of potentials for performance improvement of inverter and dc–dc converter systems by sic power semiconductors,” *IEEE Transactions on Industrial Electronics*, vol. 58, no. 7, pp. 2872–2882, 2011.
- [6] R. Menon, N. A. Azeez, A. H. Kadam, and S. S. Williamson, “Energy loss analysis of traction inverter drive for different pwm techniques and

- drive cycles,” in *2018 IEEE International Conference on Industrial Electronics for Sustainable Energy Systems (IESES)*, 2018, pp. 201–205.
- [7] X. Ding, M. Du, T. Zhou, H. Guo, C. Zhang, and F. Chen, “Comprehensive comparison between sic-mosfets and si-igbts based electric vehicle traction systems under low speed and light load,” *Energy Procedia*, vol. 88, pp. 991–997, 2016, CUE 2015 - Applied Energy Symposium and Summit 2015: Low carbon cities and urban energy systems, ISSN: 1876-6102.
- [8] J. Rąbkowski and T. Platek, “Comparison of the power losses in 1700v si igt and sic mosfet modules including reverse conduction,” in *2015 17th European Conference on Power Electronics and Applications (EPE'15 ECCE-Europe)*, 2015, pp. 1–10.
- [9] L. Ceccarelli, R. M. Kotecha, A. S. Bahman, F. Iannuzzo, and H. A. Mantooth, “Mission-profile-based lifetime prediction for a sic mosfet power module using a multi-step condition-mapping simulation strategy,” *IEEE Transactions on Power Electronics*, vol. 34, no. 10, pp. 9698–9708, 2019.
- [10] K. Ma, M. Liserre, and F. Blaabjerg, “Lifetime estimation for the power semiconductors considering mission profiles in wind power converter,” in *2013 IEEE Energy Conversion Congress and Exposition*, 2013, pp. 2962–2971.
- [11] P. D. Reigosa, H. Wang, Y. Yang, and F. Blaabjerg, “Prediction of bond wire fatigue of igbts in a pv inverter under a long-term operation,” *IEEE Transactions on Power Electronics*, vol. 31, no. 10, pp. 7171–7182, 2016.
- [12] A. Anurag, Y. Yang, and F. Blaabjerg, “Thermal performance and reliability analysis of single-phase pv inverters with reactive power injection outside feed-in operating hours,” *IEEE Journal of Emerging and Selected Topics in Power Electronics*, vol. 3, no. 4, pp. 870–880, 2015.
- [13] A. T. Bryant, P. A. Mawby, P. R. Palmer, E. Santi, and J. L. Hudgins, “Exploration of power device reliability using compact device models and fast electrothermal simulation,” *IEEE Transactions on Industry Applications*, vol. 44, no. 3, pp. 894–903, 2008.

-
- [14] D. Hirschmann, D. Tissen, S. Schroder, and R. W. De Doncker, "Reliability prediction for inverters in hybrid electrical vehicles," *IEEE Transactions on Power Electronics*, vol. 22, no. 6, pp. 2511–2517, 2007.
- [15] Z. Qiu, J. Zhang, P. Ning, and X. Wen, "Lifetime evaluation of inverter igbt modules for electric vehicles mission-profile," in *2016 19th International Conference on Electrical Machines and Systems (ICEMS)*, 2016, pp. 1–5.
- [16] S. Acharya, X. She, M. H. Todorovic, R. Datta, and G. Mandrusiak, "Thermal performance evaluation of a 1.7-kv, 450-a sic-mosfet based modular three-phase power block with wide fundamental frequency operations," *IEEE Transactions on Industry Applications*, vol. 55, no. 2, pp. 1795–1806, 2019.
- [17] C. Sintamarean, F. Blaabjerg, H. Wang, and Y. Yang, "Real field mission profile oriented design of a sic-based pv-inverter application," in *2013 IEEE Energy Conversion Congress and Exposition*, 2013, pp. 940–947.
- [18] M. F. Abdullah, S. A. Mohamad Badaruddin, M. R. Mat Hussin, and M. I. Syono, "Evaluation on the reduced graphene oxide thermal interface material and heat spreader for thermal management in high-temperature power device," *Jurnal Teknologi*, vol. 83, no. 3, pp. 53–59, Apr. 2021.
- [19] J. S. Lewis, "Reduction of device operating temperatures with graphene-filled thermal interface materials," *C*, vol. 7, no. 3, 2021, ISSN: 2311-5629.
- [20] S. Huang, Y. Zhang, S. Sun, *et al.*, "Graphene based heat spreader for high power chip cooling using flip-chip technology," in *IEEE 15th Electronics Packaging Technology Conference (EPTC 2013)*, pp. 347–352.
- [21] S. Huang, Y. Zhang, N. Wang, *et al.*, "Reliability of graphene-based films used for high power electronics packaging," in *16th International Conference on Electronic Packaging Technology (ICEPT 2015)*, pp. 852–855.

- [22] S. Huang, J. Bao, H. Ye, *et al.*, “The effects of graphene-based films as heat spreaders for thermal management in electronic packaging,” in *2016 17th International Conference on Electronic Packaging Technology (ICEPT)*, 2016, pp. 889–892.
- [23] P. Zhang, N. Wang, C. Zandén, L. Ye, Y. Fu, and J. Liu, “Thermal characterization of power devices using graphene-based film,” in *2014 IEEE 64th Electronic Components and Technology Conference (ECTC)*, IEEE, 2014, pp. 459–463.
- [24] M. R. Mat Hussin, M. Ramli, K. Wan Sabli, *et al.*, “Fabrication and characterization of graphene-on-silicon schottky diode for advanced power electronic design,” *Sains Malaysiana*, vol. 46, pp. 1147–1154, Jul. 2017.
- [25] Y. Liu and S. C. et al., “A lightweight and high thermal performance graphene heat pipe,” *Nano Select WILEY*, pp. 364–372, 2020.
- [26] Y. Liu, T. Thiringer, N. Wang, Y. Fu, H. Lu, and J. Liu, “Graphene based thermal management system for battery cooling in electric vehicles,” in *2020 IEEE 8th Electronics System-Integration Technology Conference (ESTC)*, 2020, pp. 1–4.
- [27] N. Wang, Y. Liu, L. Ye, and J. Li, “Highly thermal conductive and light-weight graphene-based heatsink,” in *2019 22nd European Microelectronics and Packaging Conference Exhibition (EMPC)*, 2019, pp. 1–4.
- [28] H. S. Seo and D. Shin, “Development of parallel and direct cooling system for ev/fcev inverter,” *SAE Technical Paper*, 2018.
- [29] G. Tang, T. c. Chai, and X. Zhang, “Thermal optimization and characterization of sic-based high power electronics packages with advanced thermal design,” *IEEE Transactions on Components, Packaging and Manufacturing Technology*, vol. 9, no. 5, pp. 854–863, 2019.
- [30] A. H. Mohamed, H. Vansompel, and P. Sergeant, “Electrothermal design of a discrete gan-based converter for integrated modular motor drives,” *IEEE Journal of Emerging and Selected Topics in Power Electronics*, vol. 9, no. 5, pp. 5390–5406, 2021.

-
- [31] J. H. Lee, J. H. Lee, J. H. Park, and C. Y. Won, "Field-weakening strategy in condition of dc-link voltage variation using on electric vehicle of ipmsm," in *2011 International Conference on Electrical Machines and Systems*, 2011, pp. 1–6.
- [32] N. Zhao, N. Schofield, and W. Niu, "Energy storage system for a port crane hybrid power-train," *IEEE Transactions on Transportation Electrification*, vol. 2, no. 4, pp. 480–492, 2016.
- [33] K. K. Prabhakar, M. Ramesh, A. Dalal, C. U. Reddy, A. K. Singh, and P. Kumar, "Efficiency investigation for electric vehicle powertrain with variable dc-link bus voltage," in *IECON 2016 - 42nd Annual Conference of the IEEE Industrial Electronics Society*, 2016, pp. 1796–1801.
- [34] A. Najmabadi, K. Humphries, and B. Boulet, "Implementation of a bidirectional dc-dc in electric powertrains for drive cycles used by medium duty delivery trucks," in *2015 IEEE Energy Conversion Congress and Exposition (ECCE)*, 2015, pp. 1338–1345.
- [35] J. O. Estima and A. J. Marques Cardoso, "Efficiency analysis of drive train topologies applied to electric/hybrid vehicles," *IEEE Transactions on Vehicular Technology*, vol. 61, no. 3, pp. 1021–1031, 2012.
- [36] K. Yamamoto, K. Shinohara, and T. Nagahama, "Characteristics of permanent-magnet synchronous motor driven by pwm inverter with voltage booster," *IEEE Transactions on Industry Applications*, vol. 40, no. 4, pp. 1145–1152, 2004.
- [37] T. Schoenen, M. S. Kunter, M. D. Hennen, and R. W. De Doncker, "Advantages of a variable dc-link voltage by using a dc-dc converter in hybrid-electric vehicles," in *2010 IEEE Vehicle Power and Propulsion Conference*, 2010, pp. 1–5.
- [38] C.-Y. Yu, J. Tamura, and R. D. Lorenz, "Optimum dc bus voltage analysis and calculation method for inverters/motors with variable dc bus voltage," *IEEE Transactions on Industry Applications*, vol. 49, no. 6, pp. 2619–2627, 2013.
- [39] J. Lemmens, J. Driesen, and P. Vanassche, "Dynamic dc-link voltage adaptation for thermal management of traction drives," in *2013 IEEE Energy Conversion Congress and Exposition*, 2013, pp. 180–187.

- [40] S. Sridharan and P. T. Krein, "Optimizing variable dc link voltage for an induction motor drive under dynamic conditions," in *2015 IEEE Transportation Electrification Conference and Expo (ITEC)*, 2015, pp. 1–6.
- [41] Y. Xu, A. Kersten, S. Klacar, and D. Sedarsky, "Maximizing efficiency in smart adjustable dc link powertrains with igbts and sic mosfets via optimized dc-link voltage control," *Batteries*, vol. 9, no. 6, 2023, ISSN: 2313-0105.
- [42] F. Yang, A. R. Taylor, H. Bai, B. Cheng, and A. A. Khan, "Using d–q transformation to vary the switching frequency for interior permanent magnet synchronous motor drive systems," *IEEE Transactions on Transportation Electrification*, vol. 1, no. 3, pp. 277–286, 2015.
- [43] Q. Li, D. Jiang, Y. Zhang, and Z. Liu, "The impact of vsfpwm on dq current control and a compensation method," *IEEE Transactions on Power Electronics*, vol. 36, no. 3, pp. 3563–3572, 2021.
- [44] O. Oñederra, I. Kortabarria, I. M. de Alegría, J. Andreu, and J. I. Gárate, "Three-phase vsi optimal switching loss reduction using variable switching frequency," *IEEE Transactions on Power Electronics*, vol. 32, no. 8, pp. 6570–6576, 2017.
- [45] S. Yunus, W. Ming, and C. E. Ugalde-Loo, "Adaptive variable switching frequency control for sic-based pmsm drive systems," in *IECON 2022 – 48th Annual Conference of the IEEE Industrial Electronics Society*, 2022, pp. 1–6.
- [46] L. Chang, M. Alvi, W. Lee, J. Kim, and T. M. Jahns, "Efficiency optimization of pwm-induced power losses in traction drive systems with ipm machines using wide bandgap-based inverters," *IEEE Transactions on Industry Applications*, vol. 58, no. 5, pp. 5635–5649, 2022.
- [47] L. Chang, W. Lee, T. M. Jahns, and K. Rahman, "Investigation and prediction of high-frequency iron loss in lamination steels driven by voltage-source inverters using wide-bandgap switches," *IEEE Transactions on Industry Applications*, vol. 57, no. 4, pp. 3607–3618, 2021.
- [48] S. Lovati, "Sic technology: Challenges and future perspectives," *Power Electronics News*, 2021.
- [49] ElectronicsWeekly.com, "The pros and cons of sic," 2018.

-
- [50] O. Josefsson, T. Thiringer, S. Lundmark, and H. Zelaya, "Evaluation and comparison of a two-level and a multilevel inverter for an ev using a modulized battery topology," in *IECON 2012 - 38th Annual Conference on IEEE Industrial Electronics Society*, 2012, pp. 2949–2956.
- [51] O. Josefsson, "Investigation of a multilevel inverter for electric vehicle applications.," in *PhD thesis, Technical university of Chalmers*, 2015.
- [52] S. Brueske, R. Kuehne, and F. W. Fuchs, "Comparison of topologies for the main inverter of an electric vehicle," in *PCIM Europe 2014; International Exhibition and Conference for Power Electronics, Intelligent Motion, Renewable Energy and Energy Management*, 2014, pp. 1–8.
- [53] N. Mohan, T. M. Undeland, and W. P. Robbins, *Power electronics: converters, applications, and design*. John wiley & sons, 2003.
- [54] S. Strobl, "Svpwm vs spwm modulation techniques," *imperix*, 2021 updated 2024.
- [55] J. Kolar, H. Ertl, and F. Zach, "Influence of the modulation method on the conduction and switching losses of a pwm converter system," in *Conference Record of the 1990 IEEE Industry Applications Society Annual Meeting*, 1990, 502–512 vol.1.
- [56] S. Amirpour, T. Thiringer, and D. Hagstedt, "Power loss analysis in a sic/igbt propulsion inverter including blanking time, mosfet's reverse conduction and the effect of thermal feedback using a pmsm model," in *IECON 2020 The 46th Annual Conference of the IEEE Industrial Electronics Society*, 2020, pp. 1424–1430.
- [57] A. Acquaviva and T. Thiringer, "Energy efficiency of a sic mosfet propulsion inverter accounting for the mosfet's reverse conduction and the blanking time," in *2017 19th European Conference on Power Electronics and Applications (EPE'17 ECCE Europe)*, 2017, P.1–P.9.
- [58] SEMIKRON, *Application Manual Power Semiconductors, ISLE Verlag 2015, Ilmenau, ISBN 978-3-938843-83-3*, pp. 274–279,
- [59] F. Casanellas, "Losses in pwm inverters using igbts," *IEE Proceedings - Electric Power Applications*, vol. 141, no. 5, pp. 235–239, 1994.
- [60] M. H. Rashid, "Power electronics handbook.," *Butterworth-heinemann*, 2017.

- [61] B. Hu, J. Ortiz Gonzalez, L. Ran, *et al.*, “Failure and reliability analysis of a sic power module based on stress comparison to a si device,” *IEEE Transactions on Device and Materials Reliability*, vol. 17, no. 4, pp. 727–737, 2017.
- [62] N. Sintamarean, F. Blaabjerg, H. Wang, F. Iannuzzo, and P. de Place Rimmen, “Reliability oriented design tool for the new generation of grid connected pv-inverters,” *IEEE Transactions on Power Electronics*, vol. 30, no. 5, pp. 2635–2644, 2015.
- [63] M. Handbook, “Reliability prediction of electronic equipment, standard mil-hdbk-217f.” 1991.
- [64] K. Ma, M. Liserre, F. Blaabjerg, and T. Kerekes, “Thermal loading and lifetime estimation for power device considering mission profiles in wind power converter,” *IEEE Transactions on Power Electronics*, vol. 30, no. 2, pp. 590–602, 2015.
- [65] S. B. e. a. O.E. Özçiflikçi M. Koç, “Overview of pmsm control strategies in electric vehicles: A review,” *International Journal of Dynamics and Control*, vol. 12, pp. 2093–2107, June 2024.
- [66] W. Purwanto, R. Risfendra, D. Fernandez, D. Sudarno Putra, and T. Sugiarto, “Design and comparison of five topologies rotor permanent magnet synchronous motor for high-speed spindle applications,” *International Journal of GEOMATE*, vol. 13, pp. 148–154, Dec. 2017.
- [67] L. Harnefors, “Control of variable-speed drives.,” in *Applied signal processing and control, Department of electronics, Malardalen University, Vasteras, Sweden*, 2002.
- [68] A. Kronberg, *Design and simulation of field oriented control and direct torque control for a permanent magnet synchronous motor with positive saliency*, 2012.
- [69] V. Virani, S. Arya, J. Baria, *et al.*, “Modelling and control of pmsm drive by field oriented control for hev,” *C, Modelling and Control of PMSM Drive by Field Oriented Control For HEV (February 12, 2019). Advances in Power Generation from Renewable Energy Sources (AP-GRES)*, 2019.

-
- [70] H. Celik and T. Yigit, "Field-oriented control of the pmsm with 2-dof pi controller tuned by using pso," in *2018 International Conference on Artificial Intelligence and Data Processing (IDAP)*, 2018, pp. 1–4.
- [71] M. Marufuzzaman, M. B. I. Reaz, L. F. Rahman, and T. G. Chang, "High-speed current dq pi controller for vector controlled pmsm drive," *The Scientific World Journal*, vol. 2014, 2014.
- [72] C. Cavallaro, A. Di Tommaso, R. Miceli, A. Raciti, G. Galluzzo, and M. Trapanese, "Efficiency enhancement of permanent-magnet synchronous motor drives by online loss minimization approaches," *IEEE Transactions on Industrial Electronics*, vol. 52, no. 4, pp. 1153–1160, 2005.
- [73] M. Meyer and J. Bocker, "Optimum control for interior permanent magnet synchronous motors (ipmsm) in constant torque and flux weakening range," in *2006 12th International Power Electronics and Motion Control Conference*, 2006, pp. 282–286.
- [74] A. Andersson, "Electric machine control for energy efficient electric drive systems," in *PhD Thesis, Chalmers University of Technology*, 2018.
- [75] T. Jokinen, V. Hrabovcova, and J. Pyrhonen, *Design of rotating electrical machines*. John Wiley & Sons, 2013.
- [76] G. Bertotti, "General properties of power losses in soft ferromagnetic materials," *IEEE Transactions on Magnetics*, vol. 24, no. 1, pp. 621–630, 1988.
- [77] M.-S. Lim, J.-H. Kim, and J. Hong, "Experimental characterization of the slinky-laminated core and iron loss analysis of electrical machine," *IEEE Transactions on Magnetics*, vol. 51, pp. 1–1, Jul. 2015.
- [78] A. Krings and J. Soulard, "Overview and comparison of iron loss models for electrical machines," *Journal of Electrical Engineering*, vol. 10, pp. 162–169, May 2010.
- [79] J. Pyrhönen, S. Ruoho, J. Nerg, *et al.*, "Hysteresis losses in sintered nd-feb permanent magnets in rotating electrical machines," *IEEE Transactions on Industrial Electronics*, vol. 62, no. 2, pp. 857–865, 2015.
- [80] H. Polinder and M. Hoeijmakers, "Eddy-current losses in the segmented surface-mounted magnets of a pm machine," vol. 146, pp. 261–266, 1999.

- [81] Y. Wang, J. Ma, C. Liu, G. Lei, Y. Guo, and J. Zhu, "Reduction of magnet eddy current loss in pmsm by using partial magnet segment method," *IEEE Transactions on Magnetics*, vol. 55, no. 7, pp. 1–5, 2019.
- [82] S.-H. Park, E.-C. Lee, J.-C. Park, S.-W. Hwang, and M.-S. Lim, "Prediction of mechanical loss for high-power-density pmsm considering eddy current loss of pms and conductors," *IEEE Transactions on Magnetics*, vol. 57, no. 2, pp. 1–5, 2021.
- [83] E. Grunditz, "Bev powertrain component sizing with respect to performance, energy consumption and driving patterns," Ph.D. dissertation, Jun. 2014.
- [84] S. Tenner, S. Gimther, and W. Hofmann, "Loss minimization of electric drive systems using a dc/dc converter and an optimized battery voltage in automotive applications," in *2011 IEEE Vehicle Power and Propulsion Conference*, 2011, pp. 1–7.
- [85] K. H. Billings and T. Morey, *Switchmode Power Supply Handbook*, 3rd. New York: McGraw-Hill, 2011, ISBN: 978-0071639719.
- [86] MAGNETICS, "2024 magnetics powder cores catalog," 2024.
- [87] S. Ehrlich, C. Joffe, H. Thielke, M. Leinfelder, and M. März, "Comprehensive spice model for power inductor losses," in *2019 IEEE Applied Power Electronics Conference and Exposition (APEC)*, 2019, pp. 1237–1244.
- [88] A. A. Balandin, S. Ghosh, W. Bao, *et al.*, "Superior thermal conductivity of single-layer graphene," *Nano Letters*, vol. 8, no. 3, pp. 902–907, 2008, PMID: 18284217.
- [89] Y. Fu and J. H. et al., "Graphene related materials for thermal management," *2D Materials*, vol. 7, no. 1, p. 012 001, Oct. 2019.
- [90] T. M. Tritt, "Thermal conductivity: Theory, properties, and applications.," *Springer Science and Business Media*, 2005.
- [91] N. Wang, M. K. Samani, H. Li, *et al.*, "Tailoring the thermal and mechanical properties of graphene film by structural engineering.," *Small*, e1801346, 2018.
- [92] L. Peng and Z. X. et al., "Ultrahigh thermal conductive yet superflexible graphene films.," *Adv.Mater.* 2017, 29, 1700589,

-
- [93] N.-J. Song, C.-M. Chen, C. Lu, Z. Liu, Q.-Q. Kong, and R. Cai, “Thermally reduced graphene oxide films as flexible lateral heat spreaders,” *J. Mater. Chem. A*, vol. 2, pp. 16 563–16 568, 39 2014.
- [94] Z. Liu, Z. Li, Z. Xu, *et al.*, “Wet-spun continuous graphene films,” *Chemistry of Materials*, vol. 26, no. 23, pp. 6786–6795, 2014.
- [95] T. Ma, Z. Liu, J. Wen, *et al.*, “Tailoring the thermal and electrical transport properties of graphene films by grain size engineering,” *Nature Communications*, vol. 8, p. 14 486, Feb. 2017.
- [96] H. Becerril, J. Mao, Z. Liu, R. Stoltenberg, Z. Bao, and Y. Chen, “Evaluation of solution-processed reduced graphene oxide films as transparent conductors,” *ACS Nano* 2, 463, 2008.
- [97] Z. Wei, Z. Ni, K. Bi, M. Chen, and Y. Chen, “In-plane lattice thermal conductivities of multilayer graphene films,” *Carbon*, vol. 49, no. 8, pp. 2653–2658, 2011, ISSN: 0008-6223.
- [98] H. Han, Y. Zhang, N. Wang, *et al.*, “Functionalization mediates heat transport in graphene nanoflakes,” *Nature Communications*, vol. 7, no. 1, 2016.
- [99] *Engys Ltd*, Accessed 2024-12-16. Available at <https://engys.com>.
- [100] Wolfspeed., *CAB450M12XM3*, Available at https://assets.wolfspeed.com/uploads/2024/01/Wolfspeed_CAB450M12XM3_data_sheet.pdf.
- [101] W. P. CAS300M12BM2,
- [102] Infineon., *FZ600R12KE3*, Available at Infineon Datasheet.
- [103] MAGNETICS., “Magnetics powder core catalog 2024,” *Model 0078163A7*, 2024, Available at <https://www.mag-inc.com/Company/News/January-2024/New-2024-Powder-Cores-Catalog>.
- [104] Wolfspeed., *CAS300M17BM2*, Available at <https://assets.wolfspeed.com/uploads/2024/01/Wolfspeed-CAS300M17BM2-data-sheet.pdf>.
- [105] Infineon., *FZ600R17KE3*, Available at Infineon Datasheet.
- [106] A. V. Girão, G. Caputo, and M. C. Ferro, “Chapter 6 - application of scanning electron microscopy–energy dispersive x-ray spectroscopy (sem-eds),” in *Characterization and Analysis of Microplastics*, ser. Comprehensive Analytical Chemistry, T. A. Rocha-Santos and A. C. Duarte, Eds., vol. 75, Elsevier, 2017, pp. 153–168.

- [107] T. Hitachi, H. Gohara, and F. Nagaune, "Direct liquid cooling igbt module for automotive applications," *Fuji Electric Review*, vol. 58, no. 2, pp. 55–59, 2012.
- [108] K. Olesen, R. Bredtmann, and R. Eisele, "'showerpower' new cooling concept for automotive applications," 2006.
- [109] E. EDGE, *Convective heat transfer coefficients table chart*, Accessed 2024-12-16. Available at https://www.engineersedge.com/heat_transfer/convective_heat_transfer_coefficients__13378.htm.
- [110] Y. Li, "Implementation of multiple time steps for the multi-physics solver based on chtmultiregionfoam.," in *Proceedings of CFD with Open-Source Software, 2016, Edited by Nilsson. H.*, 2016.
- [111] CFDDirect, "Energy equation in openfoam," Accessed 2024-12-17. Available at <https://cfd.direct/openfoam/energy-equation/>.
- [112] openfoamwiki, "Chtmultiregionfoam," Accessed 2024-12-17. Available at <https://openfoamwiki.net/index.php/ChtMultiRegionFoam>.
- [113] "OpenFOAM," Accessed 2024-12-17. Available at <https://openfoam.org/>.
- [114] G. Mademlis, N. Sharma, Y. Liu, and J. Tang, "Zero-sequence current reduction technique for electrical machine emulators with dc-coupling by regulating the svm zero states," *IEEE Transactions on Industrial Electronics*, pp. 1–1, 2021.
- [115] IEC60404-2, "Methods of measurement of the magnetic properties of electrical steel strip and sheet by means of an epstein frame," *Int. Electrotechnical Commission (IEC)*, 2008.
- [116] S. Amirpour, T. Thiringer, and D. Hagstedt, "Energy loss analysis in a sic/igbt propulsion inverter over drive cycles considering blanking time, mosfet's reverse conduction and the effect of thermal feedback," in *2020 IEEE Energy Conversion Congress and Exposition (ECCE)*, 2020, pp. 1505–1511.